Université de Lille

iemn
Institut d'Electronique, de Microélectronique et de Nanotechnologie
UMR CNRS 8520

Thèse

Pour obtenir le grade de

Docteur de l'Université de Lille

Spécialité Éléctronique, Microélectronique, Nanotechnologie et Microondes

presentée par

Baker SHALAK

Thèse dirigée par **Christophe DELERUE, DR CNRS, HDR, IEMN**

Préparée au sein de l'Institut d'Électronique, de Microélectronique, et de Nanoélectronique (IEMN)

Dans l'école doctorale ENGSYS

Modélisation de bit quantique en technologie de silicium

Modeling of Quantum Bit in Silicon Technology

Thèse soutenue le 10 Mai 2023 devant le jury composé de:

Madame Valérie VALLET

HDR, DR CNRS, PhLam, Présidente

Monsieur Marco PALA

HDR, DR CNRS, C2N, Rapporteur

Monsieur Nicolas CAVASSILAS

HDR, Professeur à Aix-Marseille Université, IM2NP, Rapporteur

Monsieur Romain MAURAND

HDR, LaTEQS, CEA Grenoble, Examinateur

Monsieur Yann-Michel NIQUET

HDR, IRIG, CEA Grenoble, Examinateur

This thesis is dedicated to *my beloved parents*

Acknowledgments

I would like to acknowledge and give my warmest thanks to my supervisor Christophe DELERUE who made this work possible by having an answer to all of my questions. His guidance and advice carried me through all stages of writing my project.
I would like also to acknowledge Yann-Michel NIQUET for all fruitful discussions.
I would like to acknowledge my beloved parents and siblings for the moral and financial supports in making this work. Not to forget all my friends. My endless thanks to God for giving me strength and blessings to make this work possible.

Contents

List of Figures

List of Figures

List of Tables

List of Abbreviations and Symbols

Abbreviations

MOS	Metal Oxide Semiconductor
CMOS	Complementary Metal Oxide Semiconductor
RF	Radio Frequency
SOI	Silicon On Insulator
Qubit	Quantum Bit
RLC	Resistor Inductor Capacitor
QCCD	Quantum Charge-coupled Device
EDSR	Electric Dipole Spin Resonance
RTN	Random Telegraph Noise
MOSFET	Metal-Oxide-Semiconductor Field Effect Transistor
BOX	Buried Oxide
2DEG	2D electron gas

Abtract

Noise sources are one of the critical factors that determine the performance of qubits in quantum computing applications. Noise sources refer to any external factors that can cause errors or decoherence in a qubit. In this thesis, we have simulated these effects in the case of a hole spin qubit in Silicon-On-Insulator (SOI) technology.

Charge fluctuators are one of the major sources of noise in hole spin qubits. The presence of moving charges can introduce fluctuations in the electric field around the hole. Charge fluctuators may arise from impurities or defects in the oxide layers in the vicinity of silicon regions. They can induce random changes in the energy levels, wavefunctions and g-factors of the hole spin, causing errors or decoherence in the qubit.

This makes it essential to study the impact of charge fluctuators on hole spin qubit. We simulate a quantum dot confining a single hole. The confinement is defined by electrostatic gates on a silicon nanowire channel. Our goal is to describe the qubit as realistically as possible compared to technologies which were recently developed and characterized. Our simulation takes into account the relaxation and the dephasing of the hole spin over time by combining Poisson and time-dependent Schrödinger equations to model a classical random telegraph signal. Our approach is able to describe the combined effects of fluctuating electric fields and spin-orbit coupling on the spin dynamics, without any free parameter.

We show that the well-known two-level model effectively describes the dephasing time T_2 over a broad range of frequencies ν of the telegraph signal. When ν is low, the decoherence is determined by the short time behavior of the spin precession

phase which is then characterized by a non-Gaussian distribution, the coherence of the phase is lost as soon as the fluctuator changes state. The Gaussian description is only accurate above a threshold frequency ω_{th}, when the two-level system responds to the statistical distribution of the fluctuator states. The dephasing time T_2 at this threshold frequency can be significantly increased by adjusting the magnetic field orientation and gate potentials along "sweet" lines. However, we show that T_2 cannot tend to infinity for reason which are discussed. The existence of "sweet" points is now an experimentally established fact. The simulations also show that the spin relaxation time T_1 cannot be accurately described by the two-level model as the coupling to higher-energy hole levels greatly impacts the spin dynamics.

We also study decoherence processes in the same hole spin qubit using the Bloch-Redfield theory. We show that this theory works well at high frequency ν, when the dynamics of the hole spin is slow compared to the fluctuations of its environment. Limits of the Bloch-Redfield theory at low frequency are identified.

Résumé

Les sources de bruit sont l'un des facteurs critiques qui déterminent les performances des qubits dans les applications de calcul quantique. Les sources de bruit font référence à tous les facteurs externes qui peuvent causer des erreurs ou de la décohérence dans un qubit. Dans cette thèse, nous avons simulé ces effets dans le cas d'un qubit de spin à trous en technologie Silicon-On-Insulator (SOI).

Les fluctuations de charges sont l'une des principales sources de bruit dans les qubits de spin à trous. La présence de charges mobiles peut introduire des fluctuations dans le champ électrique autour du trou. Les fluctuateurs de charge peuvent provenir d'impuretés ou de défauts dans les couches d'oxyde à proximité des régions de silicium. Ils peuvent induire des changements aléatoires dans les niveaux d'énergie, les fonctions d'onde et les facteurs g du spin du trou, provoquant des erreurs ou la décohérence du qubit.

Il est donc essentiel d'étudier l'impact des fluctuateurs de charge sur le qubit de spin de trou. Nous simulons un point quantique confinant un seul trou. Le confinement est défini par des grilles électrostatiques sur un nanofils de silicium. Notre objectif est de décrire le qubit de manière aussi réaliste que possible par rapport aux technologies qui ont été récemment développées et caractérisées. Notre simulation prend en compte la relaxation et le déphasage du spin du trou dans le temps en combinant les équations de Poisson et de Schrödinger dépendant du temps pour modéliser un signal télégraphique aléatoire classique. Notre approche est capable de décrire les effets combinés des champs électriques fluctuants et du couplage spin-orbite sur la dynamique du spin, sans aucun paramètre libre.

Nous montrons que le modèle à deux niveaux bien connu décrit efficacement

le temps de déphasage T_2 sur une large gamme de fréquences ν du signal télégraphique. Lorsque ν est faible, la décohérence est déterminée par le comportement à court terme de la phase de précession du spin qui est alors caractérisée par une distribution non gaussienne, la cohérence de la phase est perdue dès que le fluctuateur change d'état. La description gaussienne n'est précise qu'au-dessus d'une fréquence seuil ω_{th}, lorsque le système à deux niveaux répond à la distribution statistique des états du fluctuateur. Le temps de déphasage T_2 à cette fréquence seuil peut être augmenté de manière significative en ajustant l'orientation du champ magnétique et les potentiels de grille le long des lignes "douces". Cependant, nous montrons que T_2 ne peut pas tendre vers l'infini pour des raisons qui sont discutées. L'existence de points "doux" est maintenant un fait expérimentalement établi. Les simulations montrent également que le temps de relaxation du spin T_1 ne peut pas être décrit avec précision par le modèle à deux niveaux, car le couplage aux niveaux de trous de plus haute énergie a un impact important sur la dynamique du spin.

Nous étudions également les processus de décohérence dans le même qubit de spin à trous en utilisant la théorie de Bloch-Redfield. Nous montrons que cette théorie fonctionne bien à haute fréquence ν, lorsque la dynamique du spin du trou est lente par rapport aux fluctuations de son environnement. Les limites de la théorie de Bloch-Redfield à basse fréquence sont identifiées.

General Introduction

Four thousand years ago, the Chinese invented the abacus, which is considered as the first computer in history. It consisted of a wooden frame containing metal rods to which beads were attached. It is still used in some countries around the world. A few thousand years later, from the sixteenth century to the nineteenth century, mechanical calculators evolved over time, including Pascal' calculator, the Leibnitz wheel, the Difference Engine, the Analytical Engine and the Tabulating Machine. A breakthrough was achieved when an electronic computer was introduced in the United States in 1930 by Vannevar Bush, which relied on vacuum tubes to switch the electrical signal to perform calculations. Another turning point in the history of computing came in 1944, when the first Mark I programmable digital computer was built by a partnership between IBM and Harvard University. Over time, several generations of computers were developed.

Similarly, the development of the computer has been accompanied by the development of its processing and storage capabilities. The integration of semiconductors in the manufacture of electronic components, in particular the transistor, invented in 1947 by J. Bardeen, W.Schockley and W. H. Brattain researchers at Bell laboratories [21] and which is the basic building block of computers, has not prevented the power of computers from increasing since the 1970s. Moore's Law predicted that the number of transistors on a microprocessor chip would double every two years [22], and thus the computing power would also double.

In order to reduce rendering time and perform larger calculations in computing, parallelism is used since the 2000s. Roughly speaking, parallelism consists of processing data simultaneously. This is done by replacing the single processor by

multiprocessors with multicores.

The first person who introduced the concept of a quantum simulator was the physicist Richard Feynmann in the 1980s [23], the principle was to find a computer that would give an approximate simulation to the classical computer, but would give an exact simulation of nature, i.e. using quantum physics to simulate a quantum system. This hypothetical computer would be more efficient than a classical computer for some very specific tasks by taking advantage of the massive parallelization allowed by the superposition principle of quantum mechanics. In 1994, Peter Shor [24] developed an algorithm for prime factoring a given number in polynomial (not exponential) time. From this date on, everything accelerated, and significant progress was made by researchers. Then, in 1996, Lov Grover [25], from Bell Labs, published a quantum algorithm for searching for an element in a set of n objects, and the first quantum computer with 2 qubits was announced in 1998 [26], and now the new IBM Osprey quantum processor has reached 433 Qubits [27].

The ability of quantum technology to break the level of computing speed and processing is in principle very large compared to the existing technology. Therefore France is currently developing, among other possible technologies, its own quantum informatics platform based on silicon technology. Since many of the physical aspects of this technology are still not understood, this makes the interpretation of the experimental data difficult, not to mention the optimization of the devices. The PhD thesis that I am presenting is part of a larger project concerned with quantum bit modeling, with the aim of understanding the physics behind it. One of the main issues in this field is to understand the decoherence effects of quantum information in order to try to minimize them. The results of the research performed in this thesis will help to understand the impact of the noise sources on the information lifetime and assess their importance in comparison with other noise sources.

Chapter 1

Context of the thesis - Introduction to quantum computing

1.1 Quantum computing

Quantum computing is a combination of quantum physics, information theory and computer science. It is obvious that the discovery of quantum mechanics changed our understanding of the laws of nature, and since then, several technologies have been born thanks to quantum physics, for example the laser which is based on the electronic spectrum in gases, and on the electronic band structure in semiconductors, as well as nuclear energy which is based on the knowledge of the nuclear structure of atoms. An information can be expressed in several ways, like by different languages or by numbers. This last choice allows us to manipulate information in an automatic way with the help of machines, especially computers. Quantum mechanics and information science can be considered as a scientific revolution of the 20th century. The Figure 1.1 shows the relation between the two. This second quantum revolution has been distinguished by the award of the Nobel prize in physics 2022 to Alain Aspect, John Clauser and Anton Zeilinger.

The first link between quantum physics and information theory was seen in Bell's

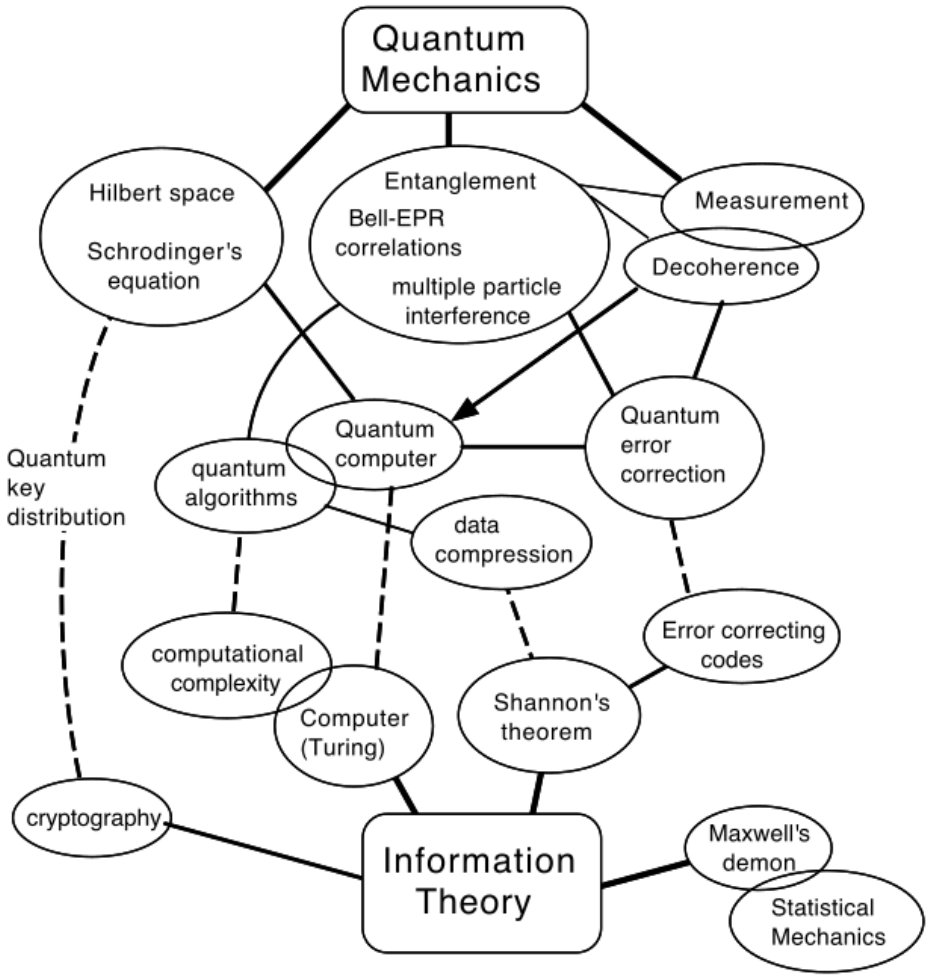

Figure 1.1: Relationship between information theory and quantum mechanics [1].

inequality which showed the importance of correlations between quantum systems that interacted with each other in the past. The second link was realized by the fact that the properties of quantum systems themselves can be used in quantum cryptography [28–31]. Another vision was brought by Feynman [23, 32] who foresaw the possibility of designing a simulator based on quantum physics to simulate other quantum systems. An important step was taken by Simon (1994) [33] who realized a quantum algorithm that solves a classically unsolvable problem, and in turn Simon inspired Shor to write a quantum algorithm that factors large integers.

With a simple two-state quantum system, one can in principle store a large amount of information, but how much information can one store in such a system? The answer is given by Jozsa and Schumacher (1994) [34] and Schumacher (1995) [35]:

it is equal to the number of states in this system which is so-called today a quantum bit or qubit.

1.2 Possible technologies

There are several technologies for realizing a quantum bit, such as superconducting qubits, trapped ion qubits, quantum dot qubits, defect-based qubits, topological qubits, photonic qubits and nuclear magnetic resonance.

1.2.1 Superconducting qubit

At very low temperatures, on the order of a few mK, a RLC (Resistor Inductor Capacitor) superconducting circuit has negligible resistance due to the superconductivity effect, so that the circuit functions as an LC resonator, which in spite of its macroscopic size at the micrometer scale [36–38] (Figure 1.2), has quantum characteristics [39–42] and is equivalent to a quantum harmonic oscillator. The harmonic oscillator is a quantum system with equidistant energy levels, which poses the problem of how to target sepcifically the two lowest levels of the system. The solution is to introduce a Josephson junction in the circuit, which introduces a nonlinearity effect in the system that removes the equidistance of the energy levels and facilitates the coding of information in a two-state system that constitutes the qubit [39, 40].

There are 3 forms of superconducting qubit. 1) The charge qubit [43–48] which is sometimes called an even Cooper box where the information is encoded by the even number of electrons in the superconductor. 2) The flux qubit [49–51] where the information is encoded by the direction of current in the circuit. 3) The phase qubit uses the difference in the phases of two superconducting wavefunctions of the Josephson junction [52]. The control of these qubits can be done by microwaves, magnetic fields or voltages. Moreover, the qubit lifetime is of the order of tens of microseconds [53], and the coupling between several superconducting qubits can be managed electronically [54, 55].

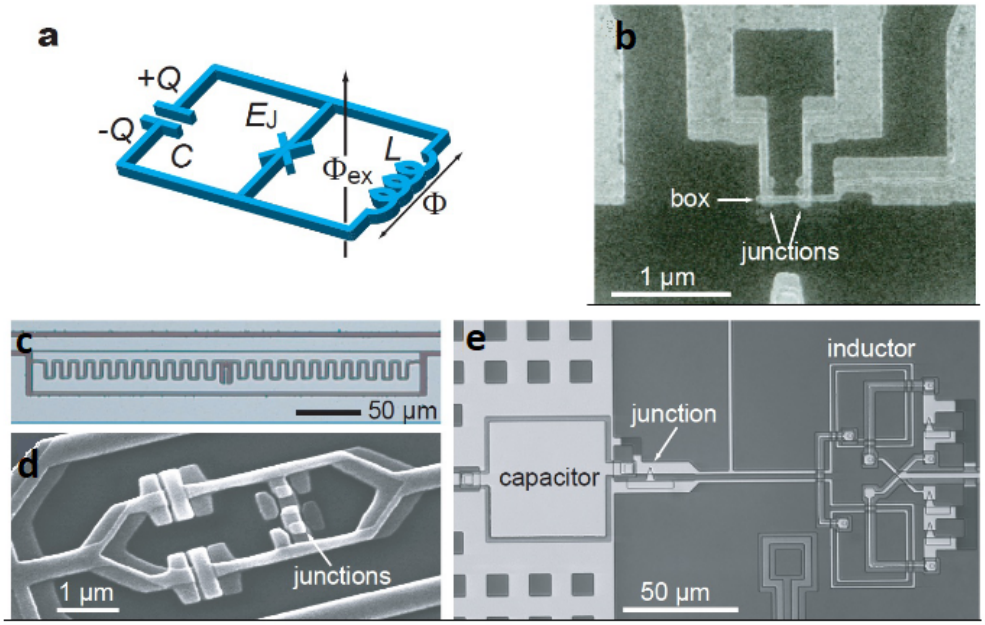

Figure 1.2: (a) Superconducting qubits model. X designs Josephson junction. The capacitance C includes a contribution from the junction itself. (b)-(e) Graphs of superconducting qubits with micro meter scale. The circuits are made of Al films. The Josephson junctions consist of Al_2O_3 tunnel barrier between two layers of Al. (b) Charge qubit, or a Cooper pair box. (c) Transmon, a derivative of charge qubit. The Josephson junction in the middle is not visible in this scale. (d) Flux qubit. (e) Phase qubit. From ref. [2]

1.2.2 Trapped ion qubits

Another existing qubit technology is the trapped ion qubit which is considered one of the most reliable among the existing technologies. One of the advantages offered by this qubit is the measurement efficiency provided by the state-dependent fluorescence detection technique [56, 57]. However, the challenge encountered is the entanglement of several qubits together.

The architecture of the quantum computer based on trapped atomic ions is interesting since the ions can be confined in space with nanometric precision, and the neighboring ions interact with each other under the effect of the coulombic force [58, 59], nearby electrodes provide electric fields that aim to create a confinement potential in the 3 dimensions of space as illustrated in Figure 1.3. A laser is used to cool the trapped ions in order to balance the system between the coulombic effect and the confinement effect. The result is a 1D linear atomic chain where its

motion is well described by quantized normal modes of harmonic oscillation.

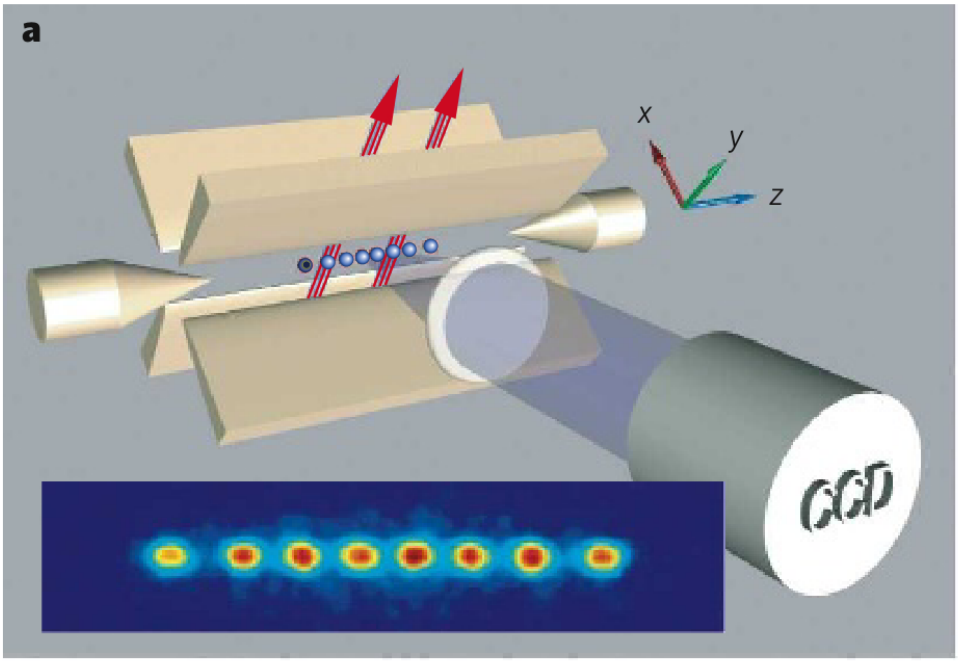

Figure 1.3: Schematic of ion trap qubit. Electric potentials are applied by electrodes to confine a 1-D crystal of individual atomic ions. Laser is used to entangle the internal levels of qubit. Resonant lasers can also cause spin-dependent fluorescence for the efficient detection of the trapped ion qubit states [2].

The entanglement of qubits is done via a laser that induces a coupling to the set of trapped spins, and then one can change the quantum state of the qubit by changing the motion of the set of trapped atoms, that occurs by modifying the modulation of the laser beam. This kind of qubit was proposed in 1995 [60] then demonstrated later in the same year [61]. The simple model proposed by Cirac-Zoller is a qubit with internal energy levels of the trapped ion and external energy levels corresponding to the harmonic motion of the whole set of ions. The entanglement of the quantum states is clearly seen after the application of two laser pulses. Consider a pair of electrons which are in the ground state $|\downarrow_1\rangle|\downarrow\rangle_2|0\rangle_m$ due to laser cooling where $|0\rangle_m$ is the ground state of the harmonic oscillator, a laser pulse is applied which changes the state of the first pair ion by exiting it at the higher harmonic level and the spin up state. Then a second laser pulse brings the system back to its fundamental harmonic state by changing the spin state of the

second ion as shown in equation (1.2.1). And so the ions forming the qubit are entangled without changing the initial harmonic state.

$$\begin{aligned} |\downarrow_1\rangle|\downarrow\rangle_2|0\rangle_m &\xrightarrow{\text{pulse 1}} |\downarrow\rangle_1|\downarrow\rangle_2|0\rangle_m + |\uparrow\rangle_1|\downarrow\rangle_2|1\rangle_m \\ &\xrightarrow{\text{pulse 2}} |\downarrow\rangle_1|\downarrow\rangle_2|0\rangle_m + |\uparrow\rangle_1|\uparrow\rangle_2|0\rangle_m \\ &= (|\downarrow\rangle_1|\downarrow\rangle_2 + |\uparrow\rangle_1|\uparrow\rangle_2)|0\rangle_m \end{aligned} \tag{1.2.1}$$

The realization of trapped ion qubit becomes more difficult when the number of trapped ions increases, the laser-induced cooling becomes less efficient, the decoherence of the harmonic mode [62] becomes more important due to the noise induced by the electical fields. One of several approaches proposed to circumvent these difficulties is the Quantum Charge-Coupled Device (QCCD) [63], it consists in transporting individual ions thanks to electric forces in different areas of the complex trap structure. The interest of this model is to process the trapped ions in small groups, between 5 and 10 atoms, where the noise infuence will be less important.

1.3 Spin qubit

By definition, quantum dots are semiconductor-based nano-structures where 3D quantum potential wells are formed. This produces discrete and quantized energy levels that look like atomic energy orbitals, which makes them similar to the qubits of trapped ions, which is why they are called artificial atoms. They are promising candidates for a qubit application similarly to trapped ions.

There are many different ways to make a quantum dot. The principle is always the same, the confinement of charge carriers (electron, hole) in small regions in the semiconductor. The first way is to develop the quantum dots in a chemical solution and then deposit them on the substrate. The other way is via MBE (molecular beam epitaxy) where the nanocrystals that form the quantum dots are developed layer by layer and are self-assembled, which gives exellent control over

the development process. Figure 1.4 presents two different types of quantum dots: Figure 1.4 (b) shows a self-assembled quantum dots where the growth process used results in small islands on a layer of semiconductor, these islands represent quantum dots.

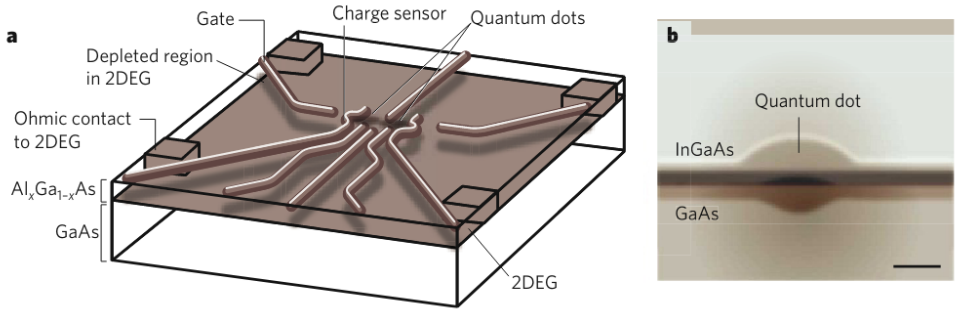

Figure 1.4: (a) Schematic of an electrostatically confined quantum dot. (b) A self-assembled quantum dot [2].

Figure 1.4 (a) shows an electrostatically defined quantum dot where the potential of metal gates creates the energy confinement. The electrostatically defined quantum dots are defined by small depletion zones in a 2D electron gas (2DEG). They work well at very low temperatures, lower than 1K, where the mean free path of electrons is spatially larger than the dimension of the quantum dot. These quantum dots are manipulated by the potential applied by the electrostatic gates. The self-assembled quantum dots have the ability to trap electrons that have an energy higher than the thermal energy, they can be manipulated by optical techniques.

Loss and DiVincenzo [64] were the first to propose the use of the spin of charge carriers in electrostatically defined quantum dots for quantum computation.

This is motivated by the advantages provided by this type of quantum dots, where, unlike self-assembled dots, can be geometrically placed on a chip in a well-designed manner in order to build quantum dot networks in which each dot represents a two-state quantum system providing the qubit. The information is carried by the degree of freedom of the intrinsic spin 1/2 of the electron (or hole).

The entanglement of two qubits can be managed by modifying the potential applied by the electrostatic gates that control the overlap of the spin wave functions,

the overlap creates orbitals that resemble a molecular orbital. The Loss and DiVincenzo model describes a quantum logic with which the measurement of spin state in the qubit is based on the coulomb blockade effect and the tunneling of electron is driven electricaly. This tunneling depends on the spin state due to the Pauli exclusion principle that prevents two electrons of the same spin from occurring the same energy level.

1.4 Silicon spin qubit

Coulomb blockade can be observed in very small devices (or quantum dots) in which the presence of electrons prevents other electrons to flow. The study of Coulomb blockade [65] in 90's was crucial to the advancement of Si-based qubit technology. There are several forms of qubit based on silicon technologies such as self-assembled nanocrystals, bottom-up grown nanowires, electrostatically gated Si/SiGe quantum dots, quantum dots in planar MOS structures, quantum dots in etched silicon nanowires, single donor impurities [66]. In this section, we will emphasize those based on MOS structures because the device studied in my thesis is based on this technology. Due to their relatively longer coherence time reaching the order of milliseconds [67] which has been demonstrated in research labs, spin qubits in silicon have attracted the attention of researchers around the world. This is due to the technological advancement in the purification of silicon as nuclear spins cause the fast decoherence of the qubit quantum state. Besides, the spin qubit is manufactured in two ways. The first one is the electrostatically defined spin qubit and the other one is the spin qubit of the impurity atoms implemented in silicon. Another advantage of the silicon technology is the ease of production due to the technological development already existing today coming from microelectronic industry, which comes from the good understanding of this material due to the years of research on it. The first silicon qubit was proposed by the University of New South Wales in Australia [68], then after a few years (in 2014), a group from the University of Delft has designed a spin qubit in Si/SiGe heterostructures, with the spin being electrically manipulated using a micro-magnet to generate an

electric field gradient. A little after, in 2016, the first CMOS (Complementary Metal Oxide Semiconductor) silicon spin qubit was made by CEA-Leti [69, 70]. Figure 1.5 shows a double quantum dot defined in a silicon nanowire. Each dot is electrostatically confined by the potential provided by a gate, in the corner of the silicon nanowire, in which a single electron or hole or a small number of electrons (holes) can be trapped. The qubit spin control is done via a technique called EDSR (Electric Dipole Spin Resonance) which consists of using a variable electric field and the spin-orbit coupling to control the qubit spin.

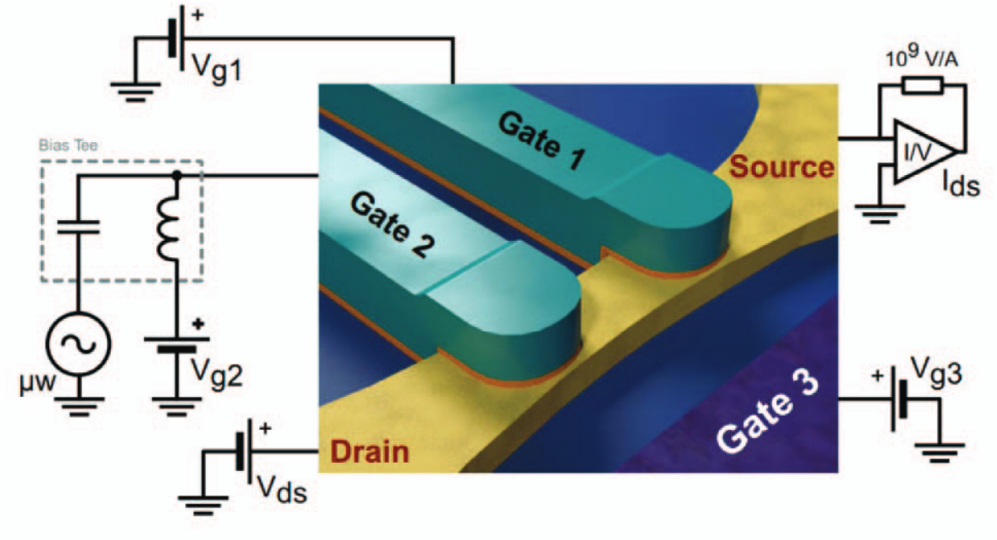

Figure 1.5: Schematic of a double quantum dot system, from ref.[3]. Each dot is defined in a Si nanowire under a gate. Other configurations of double quantum dots in a Si nanowire will be presented in chapters 3 and 4.

In this context, the Si or Ge hole qubit is of increasing interest, as the spin-orbit coupling is much more important for holes than for electrons in these materials [71]. So, as shown in the Figure 1.5, the qubit consists of two quantum dots, one contains the quantum information and the other is used to measure the first one, the qubit is formed by a source and a drain that represent two electodes, between them are the two quantum dots located in the channel and manipulated by the potential provided by other electrodes called the gates that ensure the coupling between the two dots as well as the transfer of the charge carriers between them. Their transport is done by tunneling effect from where the charge carriers are

transferred one by one between the dots. The effect of Coulomb/Pauli blockade can be used to measure the state of the spin according to the presence or absence of electronic transfer by the technique of RF (Radio Frequency) reflectometry.

1.5 Experimental progress

Table 1.1: Characteristics of different spin qubits based on semiconductor technology. f is the qubit frequency, T_2^* the coherence time, T_2 the dephasing time (spin echo) and $Q = T_2^*/T_\pi$ the quality factor. Reproduced from Ref [19].

Qubit	Material	f (MHz)	T_2^* (ns)	T_2 (ns)	$Q = T_2^*/T_\pi$	ref.
Single spin	Si/SiGe	~ 5	~ 9 x 10^2	3.7 x 10^4	~ 9	[72]
Single spin	^{28}Si	~ 0.3	≤ 1.2 x 10^5	1.2 x 10^6	≤ 80	[73]
Donor spin (e^-)	P in ^{nat}Si	~ 3	55	2 x 10^5	≤ 1	[68]
Donor spin (e^-)	P in ^{28}Si	~ 0.2	~ 3 x 10^5	1 x 10^6	~ 108	[74]
Singlet-Triplet	Si/SiGe	~ 351	~ 1 x 10^3	n.a.	n.a.	[75]
Hybrid	Si/SiGe	~ 1 x 10^4	~ 11	~ 40	~ 250	[76]

The experimental work on silicon spin qubit is evolving more and more using various approaches. In fact, CMOS technology is the preferred one because of its industrial developments and the role of silicon played in the development of information society. The earliest experimental works on CMOS-based qubit technology that is compatible with a standard manufacturing process is that reported by Leti (France) [69, 77], and the 300 mm process line for qubit manufacturing that is under development at INTEL [78].

In the table 1.1, there is a comparison of the characteristics of different silicon spin qubit technologies: qubit frequency, coherence time, T_2^* and T_2 dephasing time and quality factor. Figure 1.6 also shows some caracteristic spin lifetimes for different types of qubits. These very important quantities will be defined later in this document. More recent results will be discussed in Chapter 6.

Table 1.2 compares the physical qubit footprints produced by various technologies. The number of qubits per unit area, is provided for silicon qubits (single-spin and hybrid qubits), in comparison to the superconductive and trapped ions qubits used

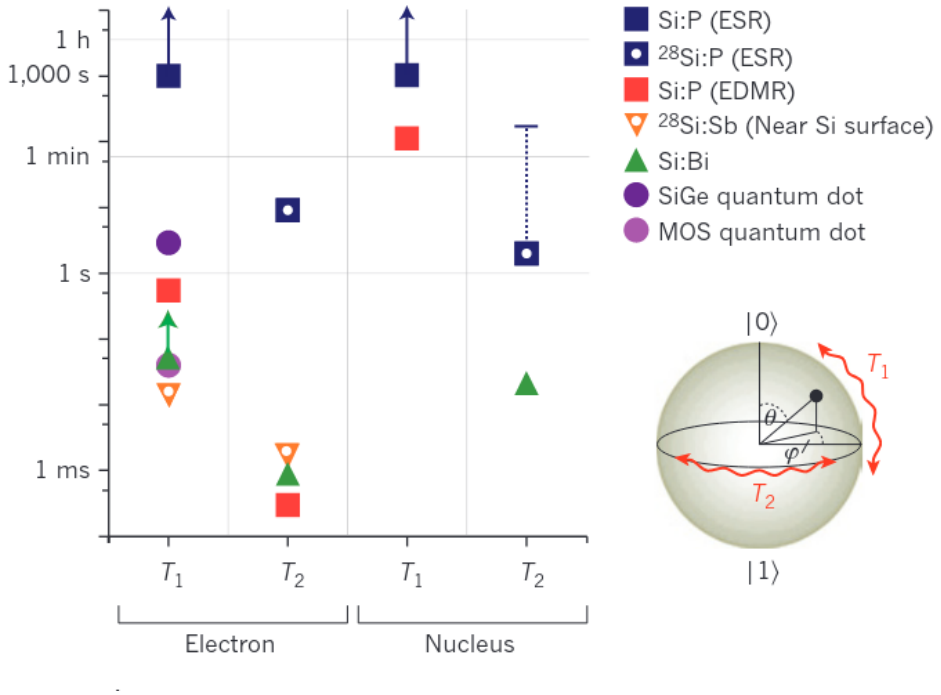

Figure 1.6: Spin lifetimes for different silicon spin qubit based on quantum dots or single donor impurities. T_1 is relaxation time and T_2 is dephasing time sketched on the sphere at the right. The arrows show how the characteristic times become larger at lower temperatures. Reproduced from Ref [4].

Table 1.2: Number of physical qubits per unit surface Mqb_{ph}/cm^2 and area $A_{chip}(mm^2)$ covered by 2 billions of physical qubits. The silicon hybrid qubit footprint refers to the 7 nm technology node. From Ref [19].

	Semiconductor Single-Spin qubit	Semiconductor Hybrid qubit (steane code)	Semiconductor Hybrid qubit (Surface code)	Superconductor Flux qubit (DWave like)	Superconductor Trasmon qubit (IBM like)	Traped ion qubit
Mqb_{ph}/cm^2	8000	830	100 x 10^2	8 x 10^{-4}	10^{-5}	2 x 10^{-5}
$A_{chip}(mm^2)$	25	240	20	25 x 10^7	2 x 10^{10}	10^{10}
Reference	[79]	[80]	[80]	[37]	[81, 82]	[83]

in current quantum computers. Silicon qubits have a far smaller footprint than superconductors and trapped ions qubits.

1.6 Objectives of the thesis

This thesis was part of the ANR project "MaqSi" dealing with the modeling and the assessment of silicon spin qubits. The objectives of the project were to understand the physics of the qubits, to sort out the existing options in order to make suggestion on the design of the qubits, and to find the strong and weak points of the SOI (Silicon On Insulator) technology for the application of quantum computing.

The project combined theory and experiments. This work was dedicated to study theoreticaly the decoherence and the variability of a qubit. The main objective of my thesis was to study the sensitivity of a hole spin qubit against the existing noise sources, especially the quasi-static charge noise found in the gate oxide layers. We focused on the study of the influence of single charge fluctuations on the lifetime of the quantum information in the qubit, this is called decoherence.

The thesis is divided in several chapters. Chapter 1 that you have read is an introduction of the general context of the thesis in which I have introduced the history of quantum computing with the presentation of the existing technologies in this field. Chapter 2 presents the different sources of noise existing in the qubit. I also discuss the telegraphic noise and decoherence phenomenon (defined by characteristic times T_1 and T_2) which represent the essence of the thesis. Chapter 3 is dedicated to describe the device geometry, and its characteristics. Chapter 4 presents the methodologies to calculate the electronic structure and the electrostatic potential in the devices. Chapter 5 describes the models developed to calculate the characteristic coherence times. In chapter 6, the results obtained will be discussed in order to make a general conclusion of the thesis. Chapter 7 provides additional results based on the Bloch-Redfield theory.

Chapter 2

Decoherence and dephasing

2.1 Introduction

A qubit is usually defined as a two-level system. The qubit is always coupled to its environment, this coupling induces a change in quantum coherence of the system called decoherence. The decoherence was always an important topic studied by physicists because of its impact on the qubit information lifetime. Different noise souces exist limiting the quantum coherence of the system, and they have been an obstacle to build a quantum computer. One of most important and not completly understood behaviour in nano devices is the 1/f noise. Random telegraph noise is a microscopic source of noise which is a possible origin of 1/f noise. In this chapter, we will discuss random telegraph noise and show the models of coherence lifetimes calculation.

2.2 Different noise sources

Silicon based qubits are always linked to undesirable interactions and disorders that limit the lifetime of the information and cause its loss. The Figure 2.1 presents a transistor with the different sources of existing noises (Courtesy : Y. M. Niquet). The gate noises (GN) are the noises produced by the metal gate of the transistor which are of magnetic and thermal fluctuation origin. The thermal noise also

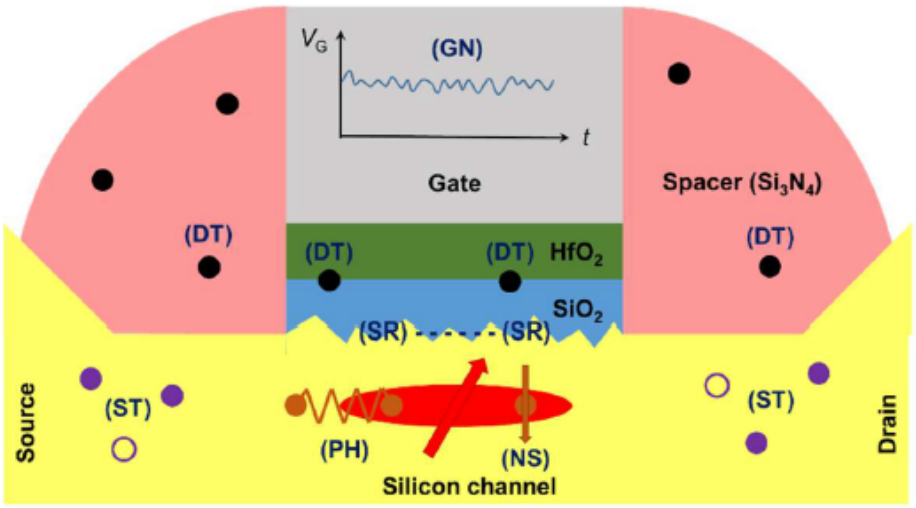

Figure 2.1: Noise sources. (SR): Surface roughness, (DT): quasi-static charge traps in the gate oxides and embedding materials, (ST): Shallow impurities near the source and drain possibly capturing/releasing charges during the operation of the qubit, (PH): Phonons, (NS): Nuclear spins, mostly in natural Si, (GN): Gate (and magnetic field) noise.

called Johnson-Nyquist noise is generated by the thermal agitation of electrons in an electrical resistance at equilibrium which will take place independently of any applied voltage. PH in Figure 2.1 stands for phonons, which are quasi-particles whose energies are quantized. They are associated with the elastic waves created by the vibrations of the crystal lattice. The phonons responsible of the relaxation of a qubit typically have an energy $\hbar\Omega$ where Ω is the Larmor angular frequency. This frequency in a hole spin qubit is generally smaller than 40 GHz. Thus, from the phonon band structure of silicon shown in Figure 2.2, it is clear that only the acoustic branches contain phonons in this energy range and then are responsible for decoherence.

One of the main sources of spin decoherence in a semiconductor-based qubit is the hyperfine coupling of the electrons with the nuclear spins (NS) of the host material, whose complex dynamics generate hyperfine field fluctuations that disturb the spin precession and cause coherence loss. The advantage of using silicon for qubit applications is manifested by the presence of a low concentration (4.7%) of the isotropic ^{29}Si isotrope in natural silicon, which reduces the effect of electron coupling to the nuclear spin compared to GaAs technologies [84]. It has been

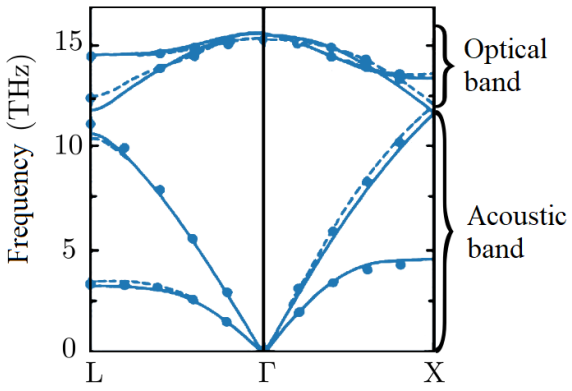

Figure 2.2: Band structure of silicon phonons along the L→ Γ → X path in the first Brillouin zone. Solid and dashed lines correspond to two computational methods. Circles represent experimental data. Adapted from reference [5].

demonstrated in 2005 that the purification of bulk crystals of silicon from their non-zero nuclear spin isotropes is possible [85]. In 2011, a high level of purification in the framework of the Avogadro project reaching a concentration of the isotrope ^{29}Si smaller than $5 * 10^{-5}$ for 1 Kg of silicon [86] was demonstrated.

Another source of decoherence is represented by the charge traps that exist in the oxide layers of components, especially the gate oxide, and are often described as quasi-static noise sources. We will not describe this aspect now because it will be discussed in detail, later in this chapter since it is the source of microscopic noise studied in this thesis.

2.3 1/f noise

Qubits are systems that exhibit high sensitivity to fluctuations, whether extrinsic, such as those due to the local electromagnetic environment, or intrinsic, such as noise from material defects. Fluctuations with 1/f (f:frequency) spectral density more generally $1/f^{\alpha}$ seem to be quite unavoidable in all nanodevices and it is therefore clear that 1/f noise plays a major role in quantum dynamics and is an important source of decoherence. The nanoscale size of nanodevices can be considered as a sensitive probe to this kind of noise and can therefore provide us with information about the microscopic origin of these noises. We could find in

the literature many systems for which there is evidence of fluctuation properties that have spectral densities that vary proportionally to 1/f over a wide frequency range. Despite, a complete physical mechanism for 1/f noise has not yet been discovered. There is no single way to explain the 1/f noise. The simplest model to reproduce the characteristics of 1/f noise is that of a set of fluctuators that represent a dynamic charge which fluctuates between two metastable states [87–89]. This produces what is known as random telegraph noise "RTN".

Due to recent developments in processing technology, it is now possible to fabricate devices with an active volume that is so small that it only holds a few charge carriers, for example silicon metal-oxide-semiconductor field-effect transistors (MOSFETs), where a random telegraph signal (RTS) can be seen in the drain current of a MOSFET as a function of time [17].

2.4 Spin decoherence

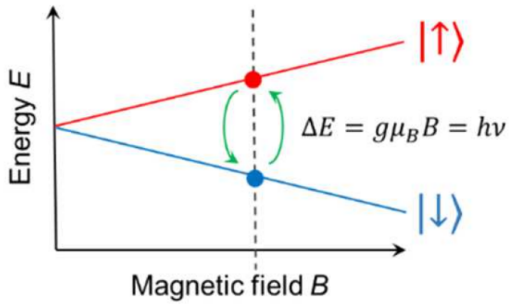

Figure 2.3: The degeneracy between the highest occupied levels of $|\uparrow\rangle$ and $|\downarrow\rangle$ spin states is lifted by a static magnetic field B.

A qubit is generally defined as a 2-level system where the degeneracy of the spin state of an electron or a hole is lifted due to an external magnetic field as seen in Figure 2.6. The electron or the hole spin undergoes a precession around the magnetic field axis taken as the z-axis. The wavefunction of the spin can be written as

$$|\psi(t)\rangle = \alpha(0)|\downarrow\rangle + \beta(0)e^{-i\Omega t}|\uparrow\rangle \tag{2.4.1}$$

where Ω is the frequency of precession, i.e. the Larmor frequency, and $|\downarrow\rangle, |\uparrow\rangle$ are the spin basis states of the electron or hole. Generally the decoherence of a qubit is defined by the loss of quantum information. It results from the change in the qubit dynamics due to various sources of noise and interactions. In this work, we study the decoherence due to single charge fluctuators [17]. The relaxation and the dephasing are two process defining the decoherence. The dissipative process where the electron spin state goes from up to down is ($|\uparrow\rangle \rightarrow |\downarrow\rangle$) is called relaxation, it is associated with the characteristic time T_1. On the Bloch sphere Figure 2.4, it corresponds to a path of the state along a z-axis, that means a change of θ. On the other side, the dephasing corresponds to the phase shift of spin compared to the perfect spin precession, i.e. a change in the phase φ on the Bloch sphere, it is associated with the characteristic time T_2.

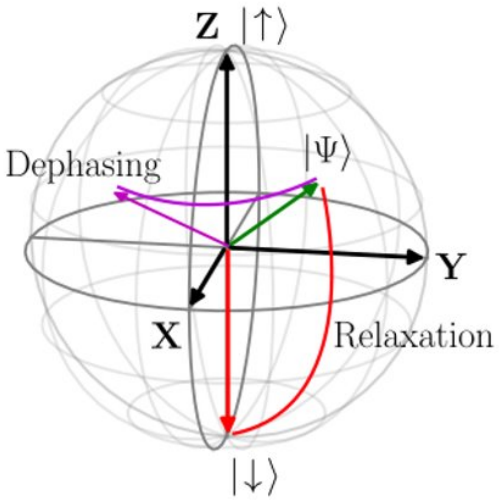

Figure 2.4: Bloch sphere.

2.5 Classical telegraph noise

In this section we show how to calculate the coherence lifetimes in the case of a classical telegraph noise. In the basis $\{|\uparrow\rangle, |\downarrow\rangle\}$, the Hamiltonian which describes a 2-level system coupled to a charge fluctuator following a random telegraphic signal reads:

$$H(t) = H_0 + \chi(t)U \tag{2.5.1}$$

with

$$H_0 = \frac{\hbar}{2}\begin{pmatrix} \Omega & 0 \\ 0 & -\Omega \end{pmatrix}; \qquad U = \begin{pmatrix} u^{\uparrow\uparrow} & u^{\uparrow\downarrow} \\ u^{\downarrow\uparrow} & u^{\downarrow\downarrow} \end{pmatrix} \tag{2.5.2}$$

where H_0 is the hamiltonian representing the spin system at the fundamental state without any perturbation or coupling to the bath, $\chi(t)$ is the telegraphic signal shown in Figure 2.5 and U is the coupling hamiltonian of the fluctuator to the qubit. For reasons that will be clarified later, we define $\omega_{th} = |u^{\uparrow\uparrow} - u^{\downarrow\downarrow}|$.

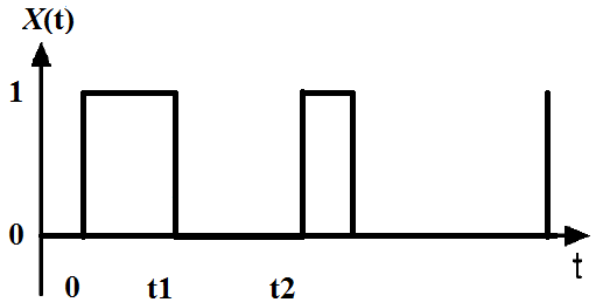

Figure 2.5: telegraphic signal.

2.5.1 Correlation function of telegraphic signal

The coherence time especially the relaxation time of a two-level system such as a qubit may depend on the noise spectral density. It is necessary to calculate the autocorrelation function of the telegraph noise signal. The autocorrelation function is a statistical tool used to analyze the degree of similarity between a time series and a shifted version of itself in order to compare the current value of a data set to its past value.

In this paragraph we show how calculate it in a general way where the telegraphic

signal is asymetric. Considering:

$$\chi(t) = \begin{cases} 1 & 0 \leq t < t1 \\ 0 & t1 \leq t < t2 \end{cases} \tag{2.5.3}$$

is a telegraphic signal which may switch between two discrete values 0 and 1, as seen in Figure (2.5). Let us define $q_1 = \langle \chi(t) \rangle$ as the average of $\chi(t)$ over time. Then consider the telegraphic signal of general form $B(t)$ with zero mean which could facilitate the calculation.

$$B(t) = \begin{cases} B_1 & = 1 - \langle \chi(t) \rangle = 1 - q_1 = q_0 \qquad 0 \leq t < t1 \\ B_0 & = 0 - \langle \chi(t) \rangle = -q_1 \qquad\qquad t1 \leq t < t2 \end{cases} \tag{2.5.4}$$

The autocorrelation function depends on the transition probability function from $B_i \to B_j$, we refer to Ref [90]. We define ν_0 and ν_1 as the probability per time unit of jump $B_1 \to B_0$ and $B_0 \to B_1$, respectively. With $\nu = \nu_0 + \nu_1$, $q_0 + q_1 = 1$ and $q_j = \frac{\nu_{1-j}}{\nu}$, we can define the transition probability function [90]

$$\begin{aligned} p_{ij}(\tau) &= Prob\left\{B(t) = B_j | B(0) = B_i\right\} \\ &= q_j + (\delta_{ij} - q_j) e^{-\nu t} \end{aligned} \tag{2.5.5}$$

Now we can write the autocorrelation function following Ref [90] as

$$\begin{aligned} C_{ij}(t) =& \langle B(t)B(0) \rangle = \sum_{ij} q_i p_{ij}(t) B_i B_j \\ =& q_0(q_0 + q_1 e^{-\nu\tau}) B_0^2 + 2q_0 q_1 (1 - e^{-\nu\tau}) B_0 B_1 + q_1(q_1 + q_0 e^{-\nu\tau}) B_1^2 \end{aligned} \tag{2.5.6}$$

Calculating the limit conditions at $t = 0$ and $t \to \infty$, we obtain

$$\begin{aligned} C_{ij}(0) =& q_0 B_0^2 + q_1 B_1^2 = q_0 q_1^2 + q_1 q_0^2 = q_0 q_1 \\ C_{ij}(\infty) =& (q_0 B_0 + q_1 B_1)^2 = 0 \end{aligned}$$

Then, the autocorrelation function reads

$$\begin{aligned} C_{ij}(t) = \langle B(t)B(0) \rangle &= C_{ij}(\infty) + [C_{ij}(0) - C_{ij}(\infty)] e^{-\nu|t|} \\ &= q_0 q_1 \; e^{-\nu|t|} \end{aligned} \tag{2.5.7}$$

Later we will use the autocorrelation function to calculate the noise spectrum of the telegraphic signal. In a symmetric case $q_0 = q_1 = 1/2$.

2.5.2 Hamiltonian in pure dephasing model

We first consider the system without spin relaxation, in a so-called pure dephasing model [91]. Non-diagonal terms of U are neglected and the Hamiltonian becomes according to reference [17]

$$H(t) = \frac{\hbar\Omega}{2}\hat{\sigma_z} + \frac{\hbar\omega_{th}}{2}\chi(t)\hat{\sigma_z} \tag{2.5.8}$$

where ω_{th} represents the change in Larmor angular frequency that fluctuates between Ω and $\Omega + \omega_{th}$ for $\chi(t) = 0$ and 1, respectively.

$\hbar\Omega$ is the Zeeman energy splitting between the energy levels of the qubit without any coupling and $\hat{\sigma_z}$ is the Pauli matrix which acts on the eigenstates $|\uparrow\rangle$, $|\downarrow\rangle$ of the qubit. $\frac{\omega_{th}}{2}\chi(t)\hat{\sigma_z}$ represents the hamiltonian describing the coupling of the qubit to a charge fluctuator.

The solution $\psi(t)$ of the time-dependent Hamiltonian equation (2.5.8) is [91]:

$$|\psi(t)\rangle = \frac{1}{\sqrt{2}}(e^{-i\Omega t/2}e^{i\varphi(t)/2}|\uparrow\rangle + e^{i\Omega t/2}e^{-i\varphi(t)/2}|\downarrow\rangle) \tag{2.5.9}$$

With

$$\varphi(t) = -\omega_{th}\int_0^t dt'\chi(t') \tag{2.5.10}$$

ψ is the superposition of $|\uparrow\rangle$ and $|\downarrow\rangle$ with a phase term $\exp(i\varphi(t)/2)$ that describes the fluctuations due to the coupling to the fluctuator and $\varphi(t)$ equation (2.5.10) represents the time evolution of the phase.

The equation (2.5.9) gives the temporal evolution of the wave function of a single realization. Experimentally, what interests us is to make an average on several measurements or realizations. Then, it is necessary to make the average of the measurements with respect to φ as shown in the equation (2.5.11)

$$\langle\hat{A}\rangle_\varphi = tr[d\varphi p(\varphi,t)\hat{\rho}(\varphi,t)\hat{A}] \tag{2.5.11}$$

where $\hat{A}$ is the observable, $\langle..\rangle_\varphi$ represents the quantum mechanical average and the average with respect to the random phase. $p(\varphi,t)$ is the probability distribution function of the φ phase and $\hat{\rho}$ represents the density matrix of the qubit.

The fact that $\hat{A}$ is independent of the phase fluctuation allows us to write:

$$\langle \hat{A} \rangle_{\varphi}(t) = tr[\hat{\rho}^{red}(t)\hat{A}] \tag{2.5.12}$$

where $\hat{\rho}^{red}$ is the reduced density matrix [91]:

$$\hat{\rho}^{red}(t) = \begin{pmatrix} \rho^{\uparrow\uparrow}(0) & \rho^{\uparrow\downarrow}(0)e^{-i\Omega t}D(t) \\ \rho^{\downarrow\uparrow}(0)e^{i\Omega t}D^{*}(t) & \rho^{\downarrow\downarrow}(0) \end{pmatrix} \tag{2.5.13}$$

which can be easily calculated from the wave function given by equation (2.5.9). We can clearly see that the diagonal elements ρ_{ii} remain constant as a function of time, i.e. the population of states does not change. This is due to the fact that we only study the qubit dephasing phenomenon and that it appears in the Hamiltonian as the diagonal term $\hbar\omega_{th}/2\hat{\sigma_z}$ (pure dephasing). The term $D(t)$ which appears in the non-diagonal elements of $\hat{\rho}^{red}(t)$ represents the evolution of the phase fluctuation due to the telegraphic signal.

$$D(t) = \langle e^{-i\omega_{th}\int_0^t dt' \chi(t')} \rangle_{\varphi} \tag{2.5.14}$$

$\langle ... \rangle \varphi$ represents the average of phase fluctuation φ on several realizations.

$$\langle ... \rangle_{\varphi} = \int d\varphi (...) p(\varphi, t) \tag{2.5.15}$$

$p(\varphi, t)$ is here the phase probability distribution for telegraphic noise and $D(t)$ is the term describing the coherence of the system.

2.5.3 Dephasing in the Gaussian approximation

It is known that the telegraphic signal is not a Gaussian noise, but it is insightful to study the coherence of the qubit by considering a Gaussian distribution probability for $q_1 = 1/2$. Experimentally, the measurements are done on several realizations. According to Ref [91], we consider that the fluctuations have a Gaussian distribution

$$p(\varphi, t) = \frac{1}{\sqrt{2\pi\langle \delta\varphi^2 \rangle}} e^{\frac{-\delta\varphi^2}{2\langle \delta\varphi^2 \rangle}} \tag{2.5.16}$$

leading to

$$D_{Gauss}(t) = \langle e^{i\varphi(t)} \rangle = e^{i\langle\varphi(t)\rangle - \frac{1}{2}\langle\delta\varphi^2\rangle}, \quad \delta\varphi(t) = \varphi(t) - \langle\varphi(t)\rangle \tag{2.5.17}$$

The mean $\langle\varphi(t)\rangle$ is equal to $-\omega_{th}t/2$ and the variance $\langle\delta\varphi^2(t)\rangle$ where $\delta\varphi(t) = \varphi(t) - \langle\varphi(t)\rangle$ is given by [91]:

$$\langle\delta\varphi^2(t)\rangle = \omega_{th}^2 \int_0^t dt' \int_0^t dt'' \langle\delta\chi(t')\delta\chi(t'')\rangle = \frac{\omega_{th}^2}{2\nu}[t - \frac{1}{\nu}(1 - e^{-\nu|t|})] \tag{2.5.18}$$

which leads to:

$$D_{Gauss}(t) = exp\{-\frac{i\omega_{th}t}{2} - \frac{\omega_{th}^2}{4\nu}[t - \frac{1}{\nu}(1 - e^{-\nu|t|})]\} \tag{2.5.19}$$

Following Ref [91], we can deduce the decoherence rate Γ_φ^{Gauss} from the visibility $|D_{Gauss}(t)|$ which at $t \to \infty$ is written as $e^{-\Gamma_\varphi^{Gauss}t}$

$$\Gamma_\varphi^{Gauss} = -\lim_{t\to\infty} \frac{1}{t} ln|D_{Gauss}(t)| = \frac{\omega_{th}^2}{4\nu} \tag{2.5.20}$$

This gives the inverse of the dephasing time T_2^* in the Gaussian approximation.

2.5.4 Exact result in pure dephasing model

In fact, the decoherence of the 2-level system due to a telegraphic noise cannot be described by the Gaussian approximation. The reason is that the probabilty function distribution of a telegraphic signal has not the shape of a Gaussian distribution. According to References [16, 17, 91] the phase distribution for a telegraphic signal switching between 0 and 1 as in equation (2.5.3) is given by the probability density:

$$p(\varphi, t) = \tag{2.5.21}$$
$$e^{-\nu t/2}[\frac{\delta(\varphi) + \delta(\varphi + \omega_{th}t)}{2} + \frac{\nu}{\omega_{th}} \frac{I_1(\nu t/2\sqrt{1 - (2/\omega_{th}t)^2(\varphi + \omega_{th}t)^2})}{\sqrt{1 - (2/\omega_{th}t)^2(\varphi + \omega_{th}t)^2}}](\theta(\varphi) + \theta(\varphi + \omega_{th}t))$$

where $\theta(\varphi)$ is the Heaviside function and I_1 is the modified Bessel function of the first kind. The probability distribution function $p(\varphi, t)$ versus the phase φ

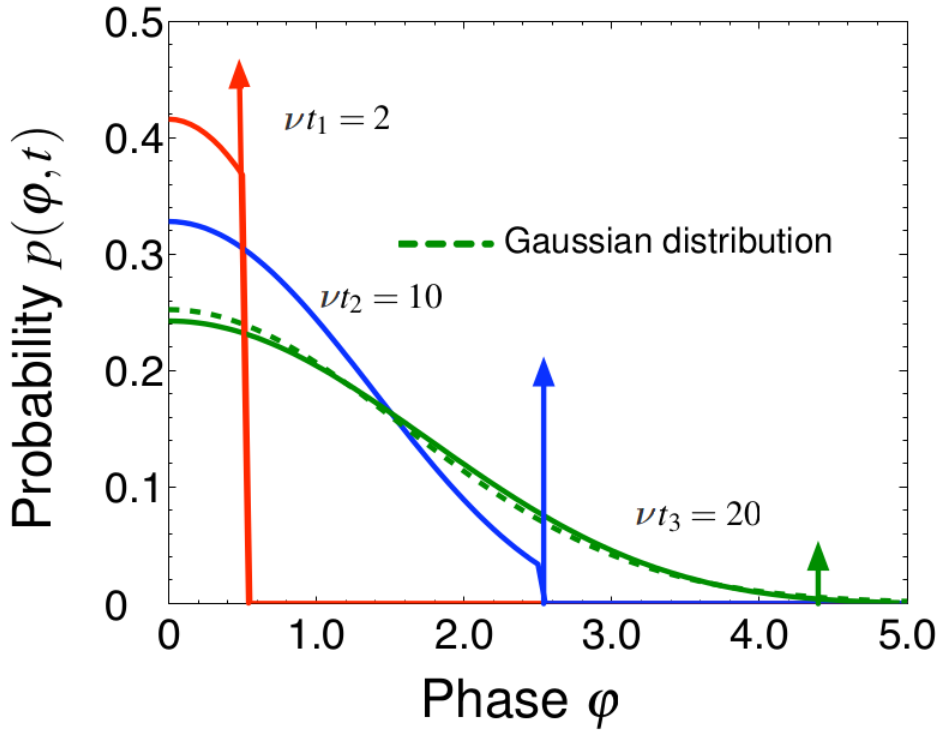

Figure 2.6: Plot showing the probability distribution function $p(\varphi, t)$ as a function of phase φ for weak coupling $\omega_{th}/\nu = 0.5$. The probability distribution is cut at $\varphi = \omega_{th}t/2$ by the δ function, which is indicated by the arrows, and the dashed line represents the asymptotic Gaussian distribution.

for different values of νt is shown in Figure 2.6. We see that for short νt, $p(\varphi, t)$ exhibits cuts due to δ-functions and for large νt, $p(\varphi, t)$ exhibits a Gaussian shape which will be discussed in chapter 6.

With a non-trivial calculation detailed in Refs [17, 91], we obtain the coherence $D(t)$ which obeys the non-Gaussian phase probability distribution 2.5.21,

$$D(t) = \frac{1}{2}e^{-i(\omega_{th}-i\nu)t/2}[(1+\frac{\nu}{2\delta})e^{\delta t} + (1-\frac{\nu}{2\delta})e^{-\delta t}] \tag{2.5.22}$$

with $\delta = \frac{1}{2}\sqrt{\nu^2 - \omega_{th}^2}$. The dephasing rate can be calculated from $D(t)$

$$\Gamma_\varphi = T_2^{*-1} = -\lim_{t\to\infty}\frac{1}{t}ln|D(t)| = \begin{cases} \frac{1}{2}(\nu - \sqrt{\nu^2 - \omega_{th}^2}) & \omega_{th} \leq \nu \\ \frac{\nu}{2} & \omega_{th} > \nu \end{cases} \tag{2.5.23}$$

This differs from $\Gamma_\varphi^{Gauss} = \omega_{th}^2/(4\nu)$ calculated with the Gaussian approximation seen above. However, the Gaussian approximation becomes exact in the limit $\nu >> \omega_{th}$.

2.5.5 Relaxation time T_1

The spin relaxation is induced by the presence of non-diagonal terms in the matrix U. An expression of T_1 was obtained by several approaches such as the Born-Markov master equation [92], the Bloch-Redfield theory [93, 94] (chapter 7), and the systematic weak-damping approximation in a path-integral approach [95]. T_1^{-1} is proportional to the noise spectrum $S(\Omega)$ at the frequency Ω [17].

As discussed previously, we can write the hamiltonian as followed

$$H(t) = H_0 + \langle\chi(t)\rangle U + (\chi(t) - \langle\chi(t)\rangle)U \tag{2.5.24}$$

that can be rewritten as

$$H(t) = H_m + V(t) \tag{2.5.25}$$

where H_m which is time independent and $V(t)$ depends on time

$$\begin{cases} H_m &= H_0 + \langle\chi(t)\rangle U \\ \\ V(t) &= B(t)U \end{cases} \tag{2.5.26}$$

where $B(t)$ was defined previously. The relaxation rate is determined by the noise spectrum at Larmor frequency Ω which is defined as (see Ref [17] and chapter 7)

$$\begin{aligned} S(\Omega) &= \frac{1}{2\pi\hbar^2}\int_{-\infty}^{\infty} d\tau e^{i\Omega t}\langle B(t)B(0)\rangle \\ &= \frac{q_0 q_1 \nu}{\pi\hbar^2(\nu^2+\Omega^2)} \end{aligned} \tag{2.5.27}$$

Then the relaxation time is written as

$$T_1^{-1} = 4\pi|u^{\uparrow\downarrow}|^2 S(\Omega) = \frac{4\Delta u^{\uparrow\downarrow}u^{\downarrow\uparrow}\nu}{\hbar^2(\nu^2+\Omega^2)} \tag{2.5.28}$$

with $\Delta = q_0 q_1$. Another proof of this result in the limit $\nu << \Omega$ is given in Appendix D.

2.5.6 Coherence time T_2 in the general case

T_2^* was derived in the pure dephasing model, i.e. in absence of non-diagonal terms in the matrix U. In the more general case where $u^{\uparrow\downarrow} \neq 0$, by referring to Bloch-

Redfield ([93, 94] and chapter 7) and Cohen-Tannoudji [92], the exprexxion of T_2 is

$$T_2^{-1} = T_2^{*-1} + (2T_1)^{-1} \tag{2.5.29}$$

2.6 Conclusion; outlook

In this chapter we discussed the different sources of decoherence, namely phonons, Nyquist noise, nuclear magnetic, and we focused on charge fluctuator noise. We have introduced an overview on 1/f noise and its link with the charge fluctuator. Then we described mathematically the Random Telegraph Noise in order to calculate the characteristic times of coherence in a two-level system.

Chapter 3

Silicon spin qubits

3.1 Introduction

In this chapter we will discuss the development of a spin qubit in silicon technology which was done at CEA. We will see the difference between a spin electron qubit and a spin hole qubit according to the different characteristics of the conduction and valence bands. Then we will discuss the different electrical characteristics and physical effects in the hole qubit, plus the effect of temperature. At the end we will briefly present different experimental measurements made to characterize a hole qubit.

3.2 Qubit geometry

INAC is a laboratory for condensed matter and low-temperature physics (now included in the institute IRIG), while LETI is a microelectronics laboratory. The CEA Grenoble (University Grenoble Alpes) comprises the two labs. With all of the relevant experience, developing a silicon qubit component was a natural way to address quantum computing technology.

Silicon nanowire technology has received a lot of interest in the race of Moore's law. The development of the so-called silicon-on-insulator (SOI) trigate transistor has made significant advances, particularly at CEA Leti. As sketched in Figure

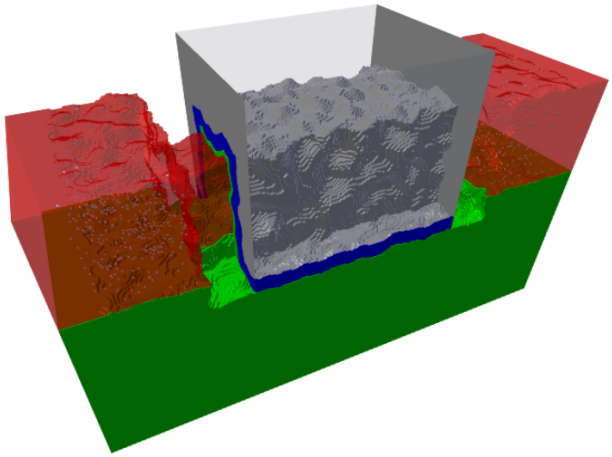

Figure 3.1: Trigate silicon MOSFET (Metal-Oxide-Semiconductor Field Effect Transistor) fabricated at Leti. SiO_2 in green, silicon is in red, the metallic gate is in gray and HfO_2 in blue.

3.1, it is typically formed by a nanowire of Si defined by lithography and chemical etching on a SOI substrate to reach lower dimensions of the order of 10 nm. The nanowire thus lies on a thick SiO_2 layer called the BOX (Buried Oxide), which seperates the backgate electrode from the nanowire. The source and drain are formed by highly doped extremities of the nanowire. Si_3N_4 spacers separate the source and drain contacts from the gate, which is placed on top of the nanowire in order to control the density of electrons or holes in the channel. Two oxide layers seperate the metallic gate from the Si channel, first a 1 nm thin SiO_2 layer and a second 2 nm HfO_2 layer, which has a higher dielectric constant and so enables a more efficient gate coupling. In other cases, the gate oxide is only formed of SiO_2 because HfO_2 is quite defective. The gate covers the sides with no contact with the BOX, providing great electrostatic control over the channel. The SiO_2 BOX minimizes leaking current, and the backgate adds an electrostatic handle to the system, allowing a control of the threshold voltage. Thanks to that, these devices are good candidates for low-power applications.

3.3 Description of the device

In order to make qubits more reproducible and efficient, the strategy was to configure these SOI devices with quantum simulations which are required to explain the physics due to the small dimensions of these devices. The geometry of device must first be changed because it is needed to make the device work in the single-electron or hole regime, and because there is a need of a mechanism to measure and change the spin state locally, as well as a reliable architecture that supports two-qubit operations. In the following, we go over each of these aspects to describe them.

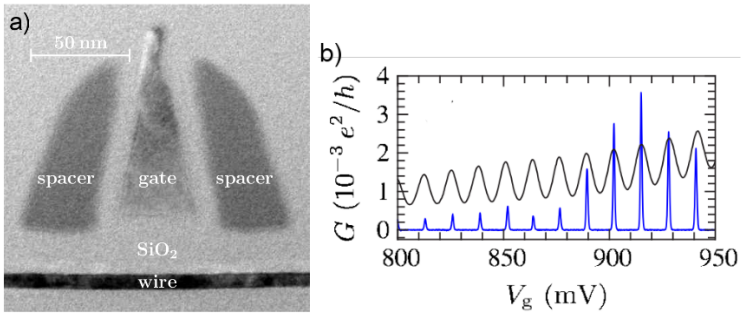

Figure 3.2: a) A MOSFET transistor with long spacers that capacitively couple to the source and drain contacts while isolating a quantum dot under the gate. b) Measured Coulomb oscillations at 4.2 K and 400 mK (black curve) (blue curve). From ref [6].

The design of the spacers (Figure 3.2 a) between the source-drain contacts and the gate is an important factor for single charge control [6]. The tunnel barriers which seperate the channel and the source/drain leads, are controlled by these spacers. They are the main reason of the creation of a quantum dot under the gate in the Coulomb blockade regime at low temperature if they are long enough. The number of electrons in the created quantum dot is controlled by varying the gate potential. The observed Coulomb oscillations are shown in Figure 3.2 b.

In order to make double quantum dots, it is necessary to add another gate to the system. In Figure 3.3, for example, two gates are connected in series to generate one quantum dot under each gate which is coupled to the neighbor dot by tunnel effect. Because of the Pauli spin blockade, which will be described later in this

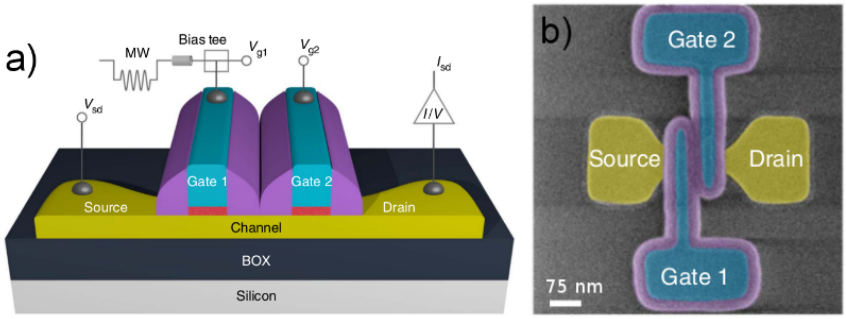

Figure 3.3: a) Double quantum dot (3D schematic). b) Top view of double quantum dot device. From ref [7].

chapter, the current can only flow if the spins in the two dots are not parallel, that makes the double qubit a perfect system to mesure qubit spin. As a result, measuring the current yields a measure of the spin, as established for electrons [96, 97] and holes [7, 98]. However, the method of detecting Pauli spin blockade is incompatible with quantum processing, which necessitates a single-shot readout. As a result, gate-reflectometry is a technique used for single-shot charge transfer detection [99–101].

3.4 Electron and hole qubits

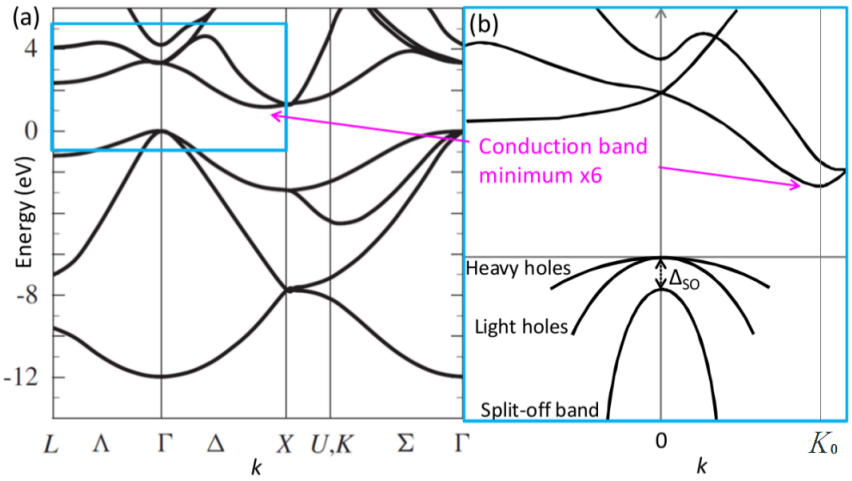

Figure 3.4: (a) Bulk silicon band structure. (b) Zoom on the valence band maximum and the conduction band minimum. From ref [8].

The main difference between a hole spin qubit and an electron spin qubit relates to the different physical characteristics of silicon valence band and conduction band. The top of the valence band for bulk silicon close to $k = 0$ is made up of two bands with distinct curvatures, the heavy (HH) and light holes (LH), which become degenerate at $k = 0$. The spin-orbit splitting energy separates the two bands from a third one known as the split-off with an energy Δ_{SO}=44 meV. The band structure of valence band will be detailed in chapter 4. The valence band is mostly composed of linear combinations of p atomic orbitals which have a orbital momentum $l = 1$, explaining the strong spin-orbit interaction near $k = 0$. The spin-orbit interaction is considerably stronger there than in the conduction band. The degree of symmetry is reduced in a nanostructure compared to the bulk. As a result, the degeneracy between HH and LH states at $k = 0$ is lifted. Then, depending on the type of confinement and strain, the resultant states are mixtures of heavy and light holes. The presence of spin-orbit coupling in the valence band of Si makes a hole qubit sensitive to electrical noise. On the other hand, it can be manipulated effectively by an electric field.

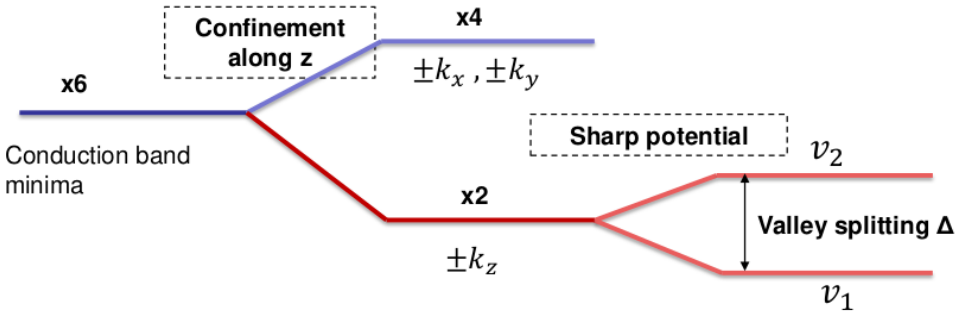

Figure 3.5: The impact of potential and confinement on the valley states in the case of an electron spin qubit [9].

On the other hand, the electron spin qubit depends on the characteristics found in the conduction band of silicon. The minimum of the conduction band is made of 6 times degenerate valleys: twice according to each direction of the reciprocal space $\pm K_{0x}$, $\pm K_{0y}$ and $\pm K_{0z}$ as seen Figure 3.5. This creates a problem for the encoding of quantum information since it requires two well-defined states. This problem can be reduced in nanostructures (e.g. quantum dots), where the confinement and

the interface of the structure destroy the symmetry and consequently produce a degeneracy lifting on the degenerate valleys. A confinement along z lifts the degeneracy between the four K_x, K_y and the two K_z. On the other hand, the lift of degeneracy between $+K_z$ and $-K_z$ is done by inter-valley scattering potentials induced by the sharp interface potential. Figure 3.5 presents a view on the impacts of confinement and sharp potentials. In a first approximation, the resultant states ν_1 and ν_2 are bonding and anti-bonding combinations of the $+K_z$ and $-K_z$ states. The energy known as the valley splitting Δ separates them.

Another remarkable feature of the silicon conduction band is that, in contrast to other III-V semiconductors, it exhibits relatively low degree of spin-orbit interaction. Due to its small atomic weight (Z = 14), which results in a lower electric field around the nucleus than for heavier atoms, silicon has a low spin-orbit effect in conduction band. In addition, the p orbitals are separated in energy and are unable to be linked effectively by the spin-orbit interaction because the conduction band minima are situated at different k values. Finally, due to the crystal centro-symmetry, Dresselhaus spin-orbit effects are negligible [102]. However, due to the relative low degree of symmetry in quantum dots compared the bulk, it has been demonstrated that, in some circumstances, this can result in a non-negligible spin-orbit interaction which can be used for spin manipulation [103, 104]. It appears that silicon could be a good choice for an electron spin qubit. The spin degree of freedom is an excellent quantum number as far as the valley splitting is high enough and the spin-orbit interaction is very low. Because of this, the spin qubit is essentially insensitive to electrical noise except at certain points of operation. Nuclear spins can be purified in silicon, therefore magnetic noises will not exist either. As a result, very coherent electron spin qubits are possible [105–107].

3.5 Main electrical characteristics

In this section we will present the main electrical characteristics of a hole qubit. The qubit is defined by a quantum dot in a silicon nanowire. A second quantum

dot is dedicated to measure the spin state of this qubit by acting as a spin filter by a spin-current conversion. For this purpose, we introduce the stability diagram and the current triangle with the two phenomena of Coulomb blockade and Pauli blockade in the double quantum dot device.

We take a system of two quantum dots linked in series, with two gates controlling the electro-chemical potentials via the voltages V_{G1} and V_{G2}. It is possible to apply a voltage V_d between the drain and the source. This mechanism is shown in Figure 3.6. Between the source, the drain, and the quantum dots, one or more holes can be transported.

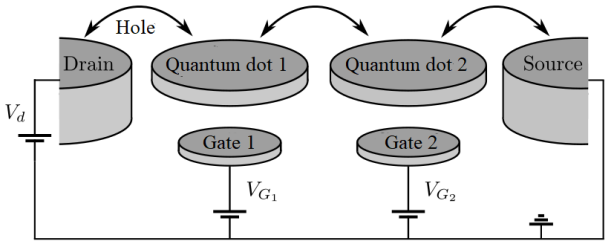

Figure 3.6: Diagram showing two quantum dots linked with a source and a drain. The source is grounded, while the voltage supplied to the drain is designated as V_d. The electro-chemical potentials of the quantum dots are controlled by the gate voltages V_{G1} and V_{G2}. The hole transport is shown by the black arrows. Inspired from refs [10, 11].

3.5.1 Coulomb blockade

The filling of these two quantum dots, which are set up in series, is based on the Coulomb blocking principle. For this, we first talk about filling a single quantum dot before moving to the case of the double quantum dot. Taking into account that to add a particle in a quantum dot of N particles, the required energy is given by

$$\mu(N+1) - \mu(N) = E_c + \Delta E \tag{3.5.1}$$

where $\mu(N)$ represents the electro-chemical potential of the dot with N carriers, Ec represents the Coulomb interaction energy and ΔE represents the energy difference

between the quantum states in the dot [11]. In the case of a spin degenerate state ($\Delta E = 0$), the injection of a second electron still requires an energy E_c, which is at the core of Coulomb blockade phenomenon. Coulomb blocking will occur when all the states of the quantum dot below the electro-chemical potential are completely filled. The quantum dot is linked to the source and drain in a one-electron transistor. This quantum dot can contain an extra particle when the gate-controlled electro-chemical potential $\mu(N+1)$ falls below the drain or source Fermi level at zero drain-source voltage. On the other hand, if the electro-chemical potential μ(N) exceeds the Fermi level, the dot loses a particle. The number of particles in the dot is constant as long as $\mu(N) < E_F < \mu(N+1)$ at $T = 0$.

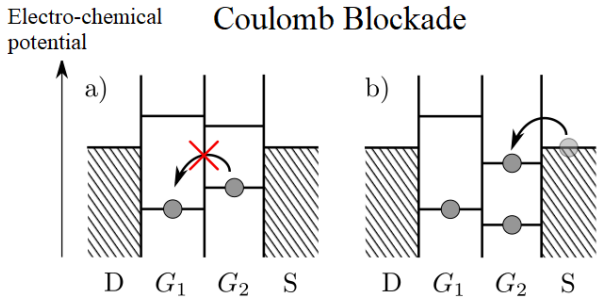

Figure 3.7: a) Diagram illustrating the Coulomb blockade. b) The filling of one of the two quantum dots, which are coupled to a source and a drain. In both scenarios, the drain/source voltage is 0.

The mechanism of filling two dots (Figure 3.6) is identical to the scenario previously discussed in the case of one quantum dot as shown in Figure 3.7. A configuration of a stable charge that corresponds to the Coulomb blockade in the case of the two quantum dots in series is shown in Figure 3.7 a. The electro-chemical potential of dot 1 after being charged in dot 2 is too high to allow a particle from dot 2 to be transported there. When the electro-chemical potential $\mu(N+1)$ for dot 2 falls below the Fermi level of the reservoirs, a particle is transferred from the source to quantum dot 2 in Figure 3.7 b.

3.5.2 Stability diagram

The voltages of the gates V_{G1} and V_{G2} of the quantum dots, in the case of two quantum dots connected in series, electrostatically control the electro-chemical

potentials of these quantum dots. The behaviour is described in Figure 3.8. As a result, the electro-chemical potentials change with varying gates voltages, allowing to load or empty the quantum dots by playing with Coulomb blocking effect. The stability diagram, which depicts the stable number of charge carriers present in these quantum dots vs the gate voltages V_{Gi} may then be created. Typical stability diagrams for the system are shown in Figure 3.8, where the pair (N_1, N_2) stands for the number of charges in each dot. The lines represent the limits of the regions with well defined number of charge carriers as function of the gate voltages. In an ideal situation, the voltage of gate i where $i \in \{1, 2\}$ controls the electro-chemical potential of quantum dot i only. Such a perfect stability diagram, as in Figure 3.8 a, would have vertical or horizontal lines dividing the various stability regions. Cross-effects, or the voltage of one grid influencing the

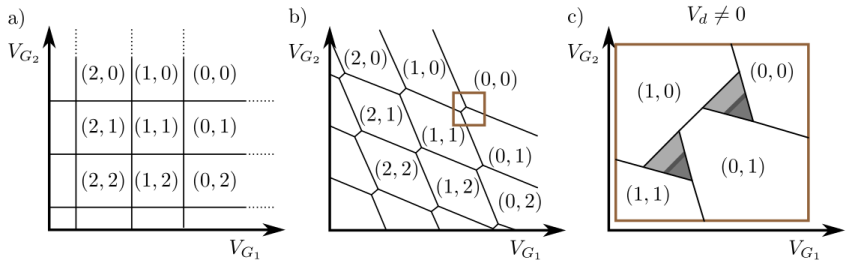

Figure 3.8: Diagram of stability according to the gate voltages V_{G1} andV_{G2}. A ideal case would have a gate controlling each of the quantum box chemical potentials. b) The quantum boxes are connected in this realistic case. Two triple points are framed by the brown square. c) Zoom of the square showing current triangles at the limit of different regions. Inspired from refs [10, 11].

electro-chemical potential of the other quantum dot, occurs in reality. The stability diagram then displays oblique lines instead of horizontal or vertical lines. Such a stability diagram is shown in Figure 3.8 b. This figure illustrates certain locations known as "triple points," where three charge configurations are degenerated. Thus, Coulomb interactions make it possible to control the filling of double quantum dots through gates acting on their electro-chemical potentials.

3.5.3 Pauli blockade

The Pauli blockade is based on the principle of Pauli exlusion which says: two holes or two electrons which have the same spin cannot be in the same state. Based on the double quantum dot device in series, we can imagine configurations exhibiting Pauli blockade. Figure 3.9 shows two cases that apply. First, we consider that

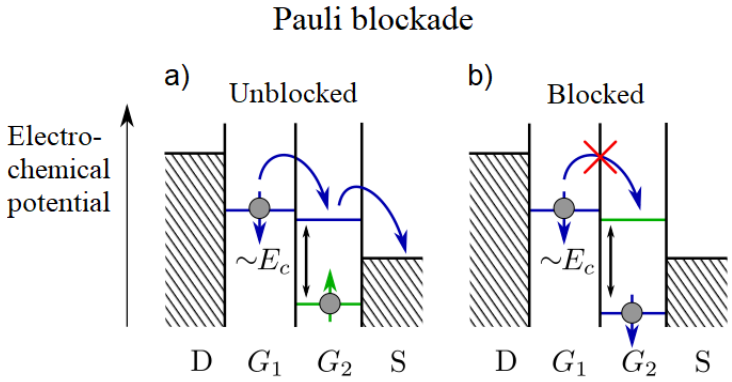

Figure 3.9: Chemical potentials for Pauli blocking are distributed. A spin $\Uparrow$ particle is depicted in green, whereas a spin $\Downarrow$ particle is depicted in blue. a) Charge can be transmitted to the source since the spin states are not blocked. b) The spin states are blocked, making it impossible for charges to go from the drain to the source.

each dot (named dot i) is filled with N_i holes where N_i is an odd number, we study the inter-dot transition $(N_1, N_2) \rightarrow (N_1 - 1, N_2 + 1)$. This is equivalent to the example: the transition $(1, 1) \rightarrow (0, 2)$. So the transition or blocking in this case depends on the hole spin of each dot. If the initial state $(1, 1)$ was $(\Uparrow, \Uparrow)$ or $(\Downarrow, \Downarrow)$, then the Pauli exclusion principle forbids the configurations $(0, 2)$ corresponding to $(0, \Uparrow\Uparrow)$ or $(0, \Downarrow\Downarrow)]$. Then, in this case, there is a current blocking. If the initial state $(1, 1)$ was $(\Uparrow, \Downarrow)$ or $(\Downarrow, \Uparrow)$, then the configurations of the form $(0, \Uparrow\Downarrow)$ or $(0, \Downarrow\Uparrow)$ are allowed. In this case, there is no current blocking: an electron can flow from the drain to the source through dots 1 and 2 (holes flow in the reverse direction).

3.5.4 Current triangle

Current triangles are regions of the stability diagram that exist around the triple point (Figure 3.8 c). This is due to the fact that the Fermi level of the source and drain align with the electro-chemical potential of the quantum dot states, in the presence of a small voltage V_d which allows current to flow through these regions. Several physical characteristics can be extracted from the current triangles [108]. The energy of the quantum dot states can be studied by analyzing the intensity and fluctuations of the observed current. Moreover, it is possible to measure the influence of the gates on the electro-chemical potential of the quantum dots thanks to the "size" of the triangles and the slope of their sides [108].

3.6 From room temperature to cryogenic situation

In this section, we will discuss the effect of temperature on the qubit formed in a transistor, based on SOI technology similar to the one described at the beginning of the chapter. A doped Si nanowire of length 200 nm, width 30 nm and height 17 nm is defined by electron beam lithography and wet etching. Silicon nitride spacers of 50 nm are present on the two sides of the gate (Figure 3.2).

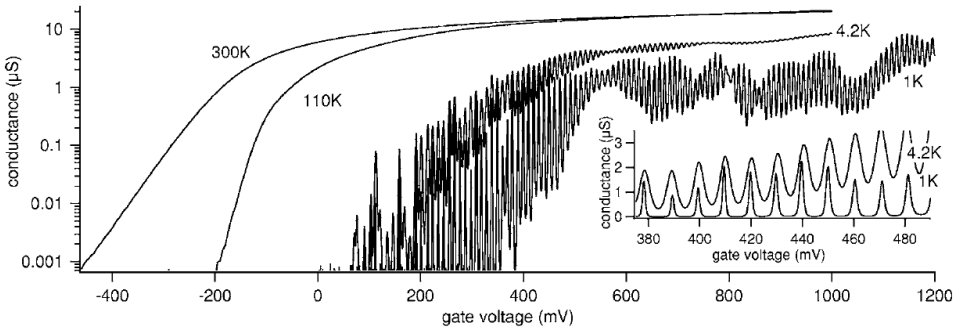

Figure 3.10: Linear drain-source conductance vs gate voltage for the device described in this section 3.6 at various temperatures. Inset: zoom on periodic Coulomb oscillations on a linear scale. From ref [12].

High doping of the exposed wire results in low resistance connections, and the gate

of the MOSFET transistor permits electron accumulation in the channel formed underneath. The low doped "access area", located between these sections under the spacers, serve as tunnel barriers on each side of the channel. Figure 3.10 depicts the I_d vs V_g characteristics at various temperatures. At lower temperatures, extremely periodic oscillations that are totally repeatable replace the monotonic curve obtained at 300 K, with the contrast increasing as the temperature drops.

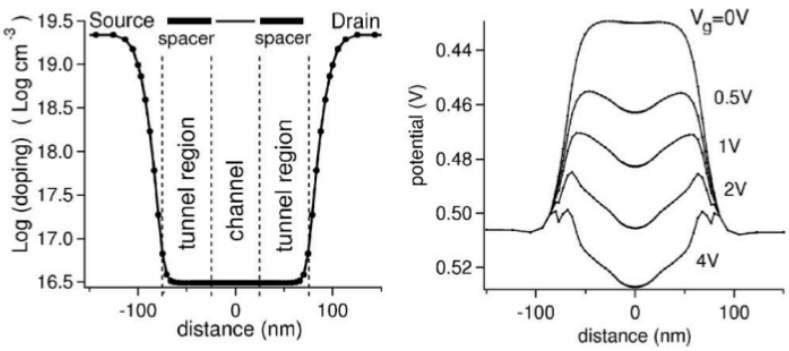

Figure 3.11: Numerical simulations of the doping (left) and potential (right) along the wire. Under the spacers and the gate, the undoped regions provide a flat potential at $V_g = 0V$, which is decreased in its center by the gate voltage, forming a well that is isolated by two barriers. From ref [12].

The potential and doping profiles along the wire are represented in Figure 3.11. A flat potential barrier is created at zero gate voltage when the doping decreases sharply under the spacers and gate. As this voltage increases, a well forms. At low temperatures, this potential well is the cause of single electron effects. Confinement does not occur if the resistance of this region falls below a threshold. For this reason, periodic Coulomb oscillations are not frequently observed in standard devices. Conversely, extremely low current is produced by extremely high access resistances. In this case, going from high to low temperature, the Coulomb oscillations appear which proves that the transistor becomes a one-electron transistor usable for quantum computing.

3.7 Experimental measurements on Si qubits

In this paragraph, we will discuss in a general way and briefly different experimental measurements performed on a hole qubit. The qubit is defined as a double quantum dot formed by a silicon nanowire of width 25 nm and height 8 nm etched on a silicon-on-insulator (SOI) substrate (Figure 3.12). Two metal gates are placed in series perpendicular to the nanowire and are separated by 30 nm. Each of them covers 35 nm of the nanowire. The 50 nm thick poly-Si and 5 nm thick TiN grids are separated from the nanowire by a few nanometers thick SiO_2 oxide layer. Silicon nitride spacers cover the gaps around the gates. The drain and source are heavily p-doped. The z=[001] axis is perpendicular to the substrate. Thanks to the voltage applied on the gates, one can control the number of charges in the quantum dots formed in the nanowire under each gate, to make the number of charges as small as possible.

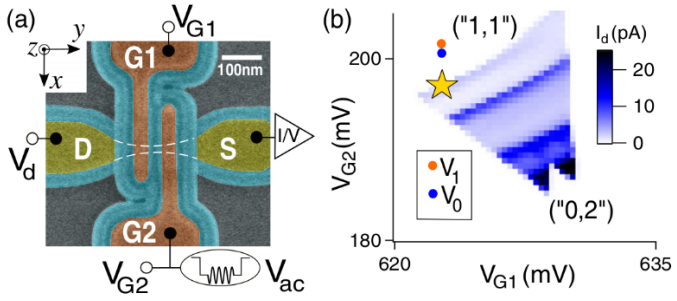

Figure 3.12: a) Image of the device obtained by scanning electron microscopy. b) Current triangles measured in the experimental device. The electrical polarizations V_0 and V_1 located out the triangle correspond to a Coulomb blocking configuration. The electrical polarization represented by a yellow star corresponds to a possible Pauli blocking configuration. Based on ref [13].

We first consider the measurement of the current triangle of Figure 3.12 which exhibits a rich physics allowing to extract the energies of the quantum dot states and to extract the values of the lever arms $\alpha_i = \frac{\partial \mu_i}{\partial V_{Gi}}$ which gives the influence of the gate j on the electro-chemical potential of the dot i and gives information about the position of the quantum dot created in the transistor channel with respect to the gate positions. And we remind that the source-drain voltage V_d is

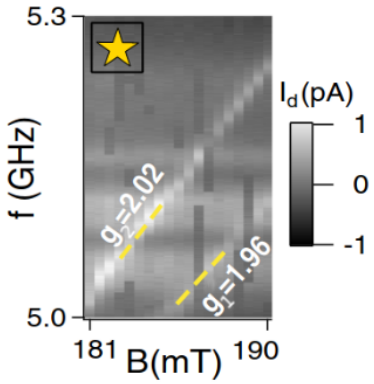

Figure 3.13: Source-drain current I_d is measured at the polarization point shown by a yellow star in the voltage-current diagram of Figure 3.12 b as a function of the frequency f_{ac} of the radio-frequency wave (V_{ac} of Figure 3.12 a) and the amplitude of the magnetic field B in Pauli blocking. From ref [13].

weak but not zero to insure the current flow.

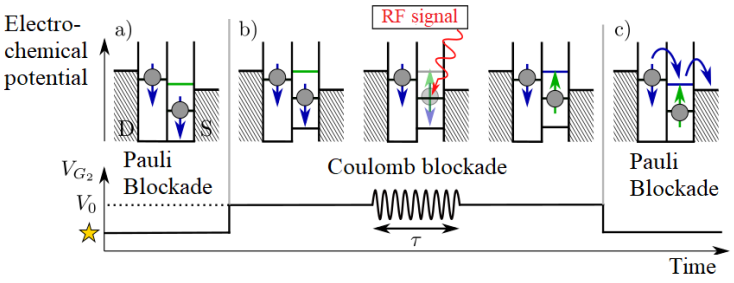

Figure 3.14: A full spin reversal is shown in the initiation, handling, and reading cycle (schematic). a) The initial state of Pauli blocking. b) Electrical control of the spin by temporary Coulomb blockade of dot 2 with a resonant radio frequency modulation on its gate. c) Pauli blockade reading.

By calculating the current I_d flowing in the nanowire as function of the frequency f_{ac} of the radio-frequency (RF) wave applied to G_2 and B (Figure 3.12 a), we can measure the gyromagnetic factor g of the qubit appearing in the equation $hf_{ac} = \mu_b g B$, μ_b is the Bohr magneton, B is the amplitude of the magnetic field. From the light lines of the Figure 3.13, we can deduce the factor g_1 and g_2 of the quantum dot 1 and 2, respectively.

Another measurement of I_d (average current) but this time as a function of the

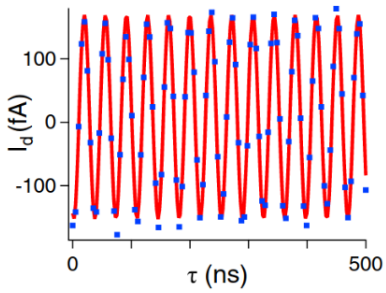

Figure 3.15: Average current I_d as a function of the time τ during which the RF signal applied (Figure 3.14). Drawn from ref [13].

time τ that a RF signal is aplied to quantum dot 2 allows to determine the spin state of the qubit. The principle is to measure the average current I_d over several cycles of initialization/manipulation/reading represented in Figure 3.14. Briefly, from the average current represented in Figure 3.15, we can conclude that I_d is maximum when the spin is unlocked, and, on the contrary, I_d is minimum when the spin is locked. Thus, by knowing the state of one dot, we can know the other and the reading is complete. Figure 3.16 shows the aggregation of the resonance frequency over 400 realizations and shows a Gaussian distribution from which one can estimate the resonance frequency. One can therefore calculate the factor g at a given potential according to the equation $g(V) = hf_L/\mu_B B$ for a given magnetic field orientation. By calculating $g(B, V)$, we can see the anisotropy of the g-factor, as shown in Figure 3.17. In fact there is a formalism called the g-tensor formalism that could make the calculation of g-factor as function of the orientation of magnetic field more easy and less costly numerically in which $(g)^2 = |\hat{g}b|^2 = {}^t b.\hat{G}.b.$ where $b = B/||B||$, and $\hat{G}$ is the tensor allowing the complete caracterisation of gyromagnetic factor g. In this case, it is not required to calculate point by point the entire map of g-factor as in Figure 3.17 a but calculating $\hat{G}$ which needs 6 different values of g to be constructed [109]. Then it could be used to calculate the g-factor for any arbitrary direction of B as seen in Figure 3.17 b.

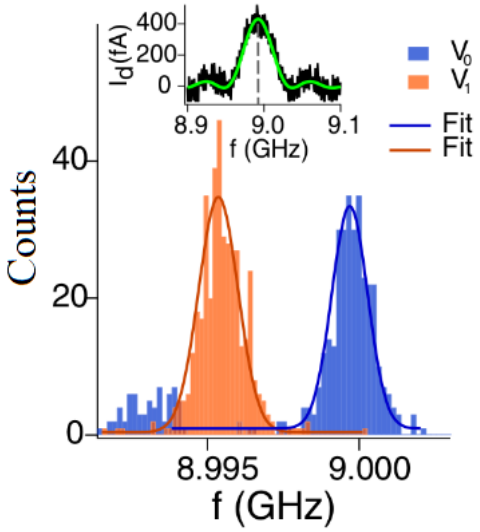

Figure 3.16: Larmor frequencies at the two electrical polarizations V_0 and V_1 are represented by a histogram (described in Figure 3.12 b). The peak of the current I_d (insert), which was measured as a function of the radio modulation frequency for a handling time of $\tau = 20$ ns in a magnetic field B = (0, 0.216, 0.216) T, served as the source of information for 400 measurements of the Larmor frequency that were used to create this histogram. Based on ref [13].

3.8 Conclusion; outlook

We have seen in this chapter that a qubit must be made of two quantum dots. The first represents the qubit itself and the other one is used to read the different characteristics of the qubit such as the Larmor frequency and the gyromagnetic factor. We have also seen that these measurements have been made thanks to the different physical effects that manage the hole or electron physics such as the Coulomb and Pauli blockades.

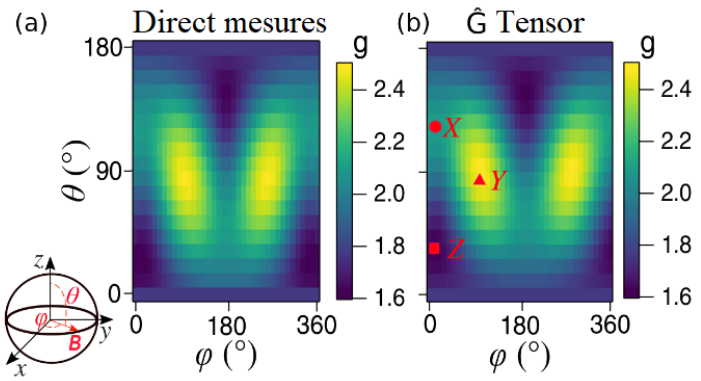

Figure 3.17: (a) Directly observed g-factor anisotropy as a function of the magnetic field orientation. (b) The g-factor computed from the reconstructed g-tensor (a). See ref [13].

Chapter 4

Methodology

4.1 Introduction

In this chapter, we discuss the methodology followed to numerically modeling the hole qubit. We first describe the structure and geometry of the qubit, then we introduce the **k.p** method to build the valence band structure around Γ (k=0, center of first Brillouin zone) by studying the influence of the different interactions on the bands. We discuss how to introduce the potential applied by the device gates described by the Poisson equation. Finally, we present the computational infrastructure that is used to bring together all the numerical methods in order to simulate the qubit

4.2 Device modeling

The three aligned Metal-Oxide-Semiconductor Field-Effect Transistors (MOSFET) shown in Figure 4.1 are formed in a Si nanowire along [110] referred to as the z axis. It has a rectangular section with width along y of 30 nm [$(1\bar{1}0)$ facets] and thickness of 10 nm along x [(001) facets]. The nanowire is laying on a 25-nm thick SiO_2 buried oxide that was formed on a doped Si substrate that may be utilized as a back gate. Three metallic gates with length and spacing along z of 30 nm are located on top of the channel and partially encircle it (over 20 nm). These

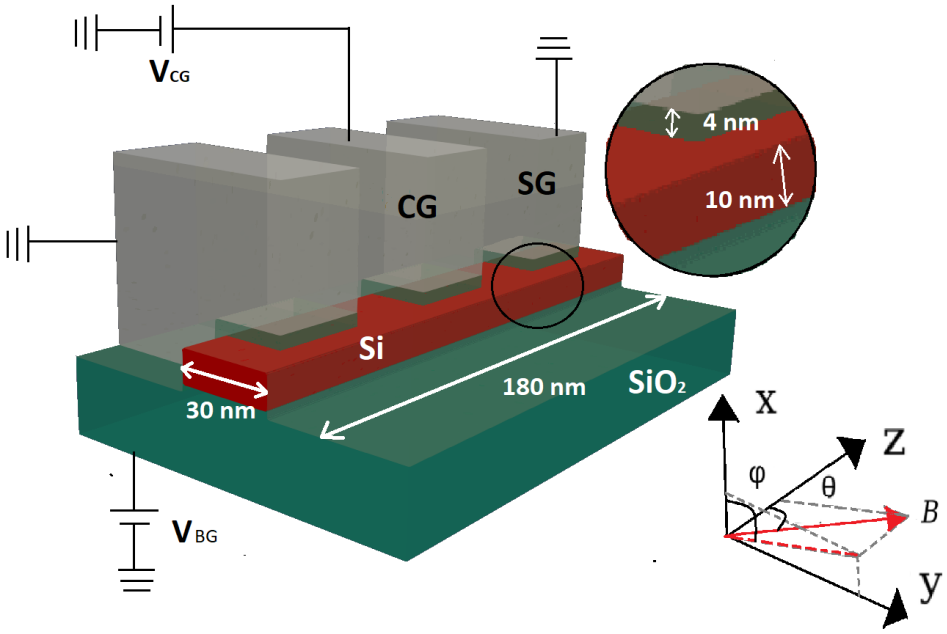

Figure 4.1: A 10 nm thick Si nanowire channel in red sitting on top of a buried oxide (green) is seen in the schematics for the hole qubit device. Top gates (gray) partially enclose the nanowire, over 20 nm of total width of 30 nm . SiO_2 is used in the gate stack (green). The hole quantum dot is represented by CG center gate. The secondary gate addressed in this paper is called SG. The polar angle θ and azimuthal angle φ shown on this diagram describe the orientation of magnetic field **B**.

metallic gates are separated from the nanowire by a 4-nm-thin SiO_2 layer. Si_3N_4 is used to cover the transistor. The voltage necessary to induce the development of a quantum dot in the nanowire corner is fixed using the central gate (CG) [110]. To the right and left of the central gate, there are two additional gates positioned along the z axis. To contain the hole in the central quantum dot, the other gates are grounded and the central gate is biased at $V_{CG} = -0.1$ V. A static magnetic field **B** is applied in the direction indicated by the azimuthal (φ) angles and polar (θ) angles as seen in Figure 4.1. This device configuration was chosen because it was already considered theoretically in Ref. [110] in which the electrical manipulation of the spin is described using a g-matrix formalism. Except otherwise stated, the Larmor frequency Ω was set to $2\pi \times 10$ rad/s.

4.3 Electronic structure: k.p

In this section, we introduce the **k**.**p** perturbation theory in solid-state physics which is a basically semi-empirical method for determining the band structure of crystalline solids centered on a certain wave vector. It allows to describe the band structure of a wide range of semiconductors. It is also used to calculate the electronic structure of objects like quantum dots in which there are discrete energy states like in a single atom due to confinement.

The principle of method is to expand the wave function at k (in fact periodic part) in the basis of the wave functions at k_0 supposed to be known. k_0 is chosen to correspond to an extremum of a band. When k is close to k_0, perturbation theory can be used leading to simplified equations. Here we discuss the method for $k_0 = 0$ which is appropriate for valence bands of zinc-blende semiconductors.

In view of the periodicity of atoms in crystals, $U(\mathbf{r})$, the potential created by the nuclei in the periodic crystal is such that:

$$U(\mathbf{r} + n_1\mathbf{a_1} + n_2\mathbf{a_2} + n_3\mathbf{a_3}) = U(\mathbf{r}) \tag{4.3.1}$$

where r is the position vector, n_i are integers and a_i are the lattice vectors. The Hamiltonian is written :

$$H = \frac{\mathbf{p}^2}{2m_0} + U(\mathbf{r}) \tag{4.3.2}$$

where m_0 is the mass of the free electron and $\mathbf{p} = -i\hbar\nabla$ represents the momentum operator. Following the Bloch theorem, the wave function is written as :

$$\Psi_{n\mathbf{k}}(r) = e^{i\mathbf{k}.\mathbf{r}} u_{n\mathbf{k}}(\mathbf{r}) \tag{4.3.3}$$

with $u_{n\mathbf{k}}$ is the periodic part

$$u_{n\mathbf{k}}(\mathbf{r} + \mathbf{a_i}) = u_{n\mathbf{k}}(\mathbf{r}), \quad \forall i \tag{4.3.4}$$

$\mathbf{k}$ represents the wave vector and n the band index. The Schrödinger equation

$$\left[\frac{\mathbf{p}^2}{2m_0} + U(\mathbf{r})\right] \Psi_{n\mathbf{k}}(\mathbf{r}) = E_{nk}\Psi_{n\mathbf{k}}(\mathbf{r}) \tag{4.3.5}$$

can be rewritten in the basis of u_{n0}:

$$u_{n\mathbf{k}}(\mathbf{r}) = \sum_{n'} c^n_{n'}(\mathbf{k}) u_{n'0}(\mathbf{r}) \tag{4.3.6}$$

as

$$\hat{H}(\mathbf{k}) c^n(\mathbf{k}) = E_{n\mathbf{k}} c^n(\mathbf{k}) \tag{4.3.7}$$

where $c^n(\mathbf{k})$ is the column matrix of the $c^n_{n'}(\mathbf{k})$ and $\hat{H}(\mathbf{k})$ is a square matrix of elements

$$[\hat{H}(\mathbf{k})]_{nn'} = \{E_{n0} + \frac{\hbar^2 \mathbf{k}^2}{2m_0}\}\delta_{nn'} + \frac{\hbar \mathbf{k}}{m_0} P_{nn'} \tag{4.3.8}$$

with $P_{nn'} = \langle u_{n0} | \mathbf{p} | u_{n'0} \rangle$

The method takes its name from the $k.p$ frame which appears in the Hamiltonian $\hat{H}(\mathbf{k})$. By diagonalizing the Hamiltonian $\hat{H}(\mathbf{k})$, we can then calculate the band structure of the material for all $\mathbf{k}$, by assuming that the eigenenergies of H_0 and the Bloch functions $\{u_{n0}\}$ are known. Details can be found in ref [111].

4.4 Hole qubit band structure

In this thesis, we study a hole qubit, for that in this part we are interested in describing the valence band structure in the neighborhood of the Γ point, center of first Brillouin zone. We start with the description of the top of the valence band structure of bulk Si at the Γ point. The approximation assumes that the valence bands can be described as linear combinations of p orbitals. It is important to know that the symmetry of the Bloch functions $u_{n\mathbf{k}}$ around $\mathbf{k} = 0$ is preserved, and then we can develop the band structure in the $\{u_x, u_y, u_z\}$ basis which corresponds to the p_x p_y p_z orbitals of the valence band and thus we can write

$$|u_{n\mathbf{k}}\rangle = \sum_{i}^{x,y,z} c^n_i(\mathbf{k}) u_{i0} \tag{4.4.1}$$

with c^n_i are coefficients. This is a 3-band model (spin degenerates), but the energy bands that are further away and do not appear in the Hamiltonian have a non-zero impact on the band structure. This is why Löwdin, in his perturbation theory [112], introduced the impact of these distant bands, which he considered as class

B bands, as a perturbation of the Hamiltonian developed on the basis of the so-called class A bands $\{u_x, u_y, u_z\}$. This leads to a renormalization of the terms of the Hamiltonian written in class A basis:

$$H_{3kp} = E_v I + \begin{pmatrix} Lk_x^2 + M(k_y^2 + k_z^2) & Nk_xk_y & Nk_xk_z \\ Nk_yk_x & Lk_y^2 + M(k_z^2 + k_x^2) & Nk_yk_z \\ Nk_zk_x & Nk_zk_y & Lk_z^2 + M(k_x^2 + k_y^2) \end{pmatrix} \tag{4.4.2}$$

where E_v is the valence band edge, I is the identity matrix. The terms L, M and N have been defined by Dresselhaus, Kip and Kittel [113]. In practice, data of cyclotron resonance may be used to experimentally calibrate all of these parameters. Figure 4.2 exhibits the silicon band structure along the line L→ Γ → X from a $k.p$ three-band description. The states are typically non-degenerate for a given non-zero k (spin degeneracy not included). However, the states can stay degenerate on pathways with high symmetry. For example, along the path L→ Γ →X, two of the three bands are degenerate.

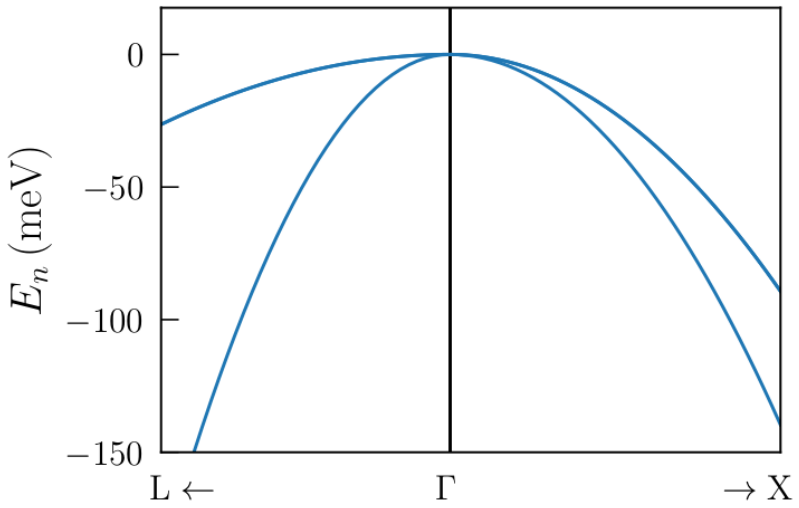

Figure 4.2: Without spin-orbit coupling, silicon band structure along the path L→ Γ →X around Γ, with $E_v = 0$, $L = -5.641$, $M = -3.607$, and $N = -8.676$ in units of $2/(2m_0)$ [14]. Along this path, the two highest energy bands are twice degenerate. The states are three times degenerate at Γ (six times with spin). →X means direction to point X (same with the point L). Figure from ref [15].

4.5 Spin-orbit coupling

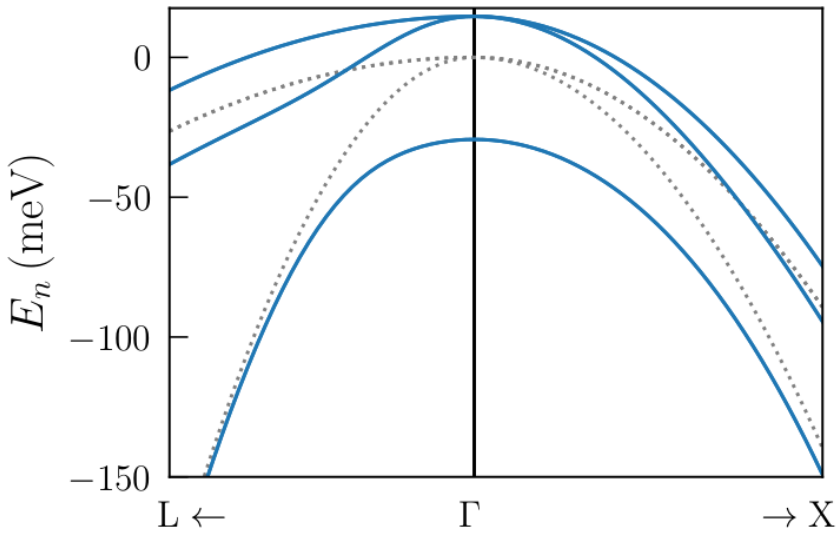

Figure 4.3: Band structure of silicon along the path L→ Γ →X with and without spin-orbit coupling (solid lines and dotted lines, respectively). With spin-orbit coupling, bands at Γ are fourfold and twofold degenerate. The first Brillouin zone is represented partially. From ref [15].

Relativistic effects cause an effective magnetic field that acts on an electron spin as it moves in a potential U. Spin-orbit coupling gets stronger when atoms get bigger. Incorporating the spin-orbit (SO) interaction into the Hamiltonian (4.3.2) leads to

$$H = \frac{\mathbf{p}^2}{2m_0} + U(\mathbf{r}) + \frac{\hbar}{4m_0^2c^2}(\sigma \times \nabla).\mathbf{p} \tag{4.5.1}$$

where σ represents the vector of Pauli matrices. With this new interaction, the basis must be expanded to take spin into account, and the extended basis reads as $\{u_{x\uparrow}, u_{y\uparrow}, u_{z\uparrow}, u_{x\downarrow}, u_{y\downarrow}, u_{z\downarrow}\}$. In this basis the SO Hamitonian reads as [114]:

$$H_{so} = \frac{\Delta_{so}}{3}\begin{pmatrix} 0 & -i & 0 & 0 & 0 & 1 \\ i & 0 & 0 & 0 & 0 & -i \\ 0 & 0 & 0 & -1 & i & 0 \\ 0 & 0 & -1 & 0 & i & 0 \\ 0 & 0 & -i & -i & 0 & 0 \\ 1 & i & 0 & 0 & 0 & 0 \end{pmatrix} \tag{4.5.2}$$

where Δ_{so} is the SO splitting at $k = 0$.

Figure 4.3 shows the valence band formed by the heavy hole (HH), the light hole (LH) and the split-off band. The matrix of H_{so} in equation (4.5.2) is formally the same as the matrix of SO coupling in the basis of p orbitals of an atom ($L = 1, s = 1/2$). This allows to write the eigenstates of H_{so} as $|J, M\rangle$ with $J = 3/2$ or $1/2$:

$$|\frac{3}{2}, \frac{+3}{2}\rangle = \frac{1}{\sqrt{2}}|(u_{x\uparrow} + iu_{y\uparrow})\rangle \tag{4.5.3}$$

$$|\frac{3}{2}, \frac{+1}{2}\rangle = \frac{1}{\sqrt{6}}[|(u_{x\downarrow} + iu_{y\downarrow})\rangle - 2|u_{z\uparrow}\rangle] \tag{4.5.4}$$

$$|\frac{3}{2}, \frac{-1}{2}\rangle = -\frac{1}{\sqrt{6}}[|(u_{x\uparrow} - iu_{y\uparrow})\rangle + 2|u_{z\downarrow}\rangle] \tag{4.5.5}$$

$$|\frac{3}{2}, \frac{-3}{2}\rangle = -\frac{1}{\sqrt{2}}|(u_{x\downarrow} - iu_{y\downarrow})\rangle \tag{4.5.6}$$

$$|\frac{1}{2}, \frac{+1}{2}\rangle = \frac{1}{\sqrt{3}}[|(u_{x\downarrow} + iu_{y\downarrow})\rangle + |u_{z\uparrow}\rangle] \tag{4.5.7}$$

$$|\frac{1}{2}, \frac{-1}{2}\rangle = \frac{1}{\sqrt{3}}[|(u_{x\uparrow} - iu_{y\uparrow})\rangle - |u_{z\downarrow}\rangle] \tag{4.5.8}$$

of energies $E_{3/2} = \frac{\Delta_{so}}{3}$ and $E_{1/2} = -\frac{2\Delta_{so}}{3}$.

These are also eigenstates of $\hat{H}(\mathbf{k})$ for $k = 0$. The states which correspond to $J = 1/2$ form the split-off band.

In the basis set $\{|\frac{3}{2}, +\frac{3}{2}\rangle, |\frac{3}{2}, +\frac{1}{2}\rangle, |\frac{3}{2}, -\frac{1}{2}\rangle, |\frac{3}{2}, -\frac{3}{2}\rangle, |\frac{1}{2}, +\frac{1}{2}\rangle, |\frac{1}{2}, -\frac{1}{2}\rangle\}$, the six-band k.p hamiltonian is given by [113, 115].

$$H_{6k.p}(\mathbf{k}) = -\begin{pmatrix} P+Q & -S & R & 0 & \frac{1}{\sqrt{2}}S & -\sqrt{2}R \\ -S^* & P-Q & 0 & R & \sqrt{2}Q & -\sqrt{\frac{3}{2}}S \\ R^* & 0 & P-Q & S & -\sqrt{\frac{3}{2}}S^* & -\sqrt{2}Q \\ 0 & R^* & S^* & P+Q & \sqrt{2}R^* & \frac{1}{\sqrt{2}}S^* \\ \frac{1}{\sqrt{2}}S^* & \sqrt{2}Q & -\sqrt{\frac{3}{2}}S & \sqrt{2}R & P+\Delta_{so} & 0 \\ -\sqrt{2}R^* & -\sqrt{\frac{3}{2}}S^* & -\sqrt{2}Q & \frac{1}{\sqrt{2}}S & 0 & P+\Delta_{so} \end{pmatrix} \tag{4.5.9}$$

with P, Q, R, S being functions of dimensionless Luttinger parameters which can be expressed as functions of L, M and N.

Table 4.1: Spin-orbit energy Δ_{so} in the valence band, Luttinger parameters and parameter κ [20] for different semiconductors.

	Si	Ge	InP	GaAs	InAs	InSb
Δ_{so} (eV)	0.044	0.29	0.11	0.34	0.41	0.80
γ_1	4.285	13.38	4.95	6.85	20.40	37.10
γ_2	0.339	4.24	1.65	2.10	8.30	16.50
γ_3	1.446	5.69	2.35	2.90	9.10	17.70
κ	-0.42	3.41	0.97	1.20	7.60	15.60

$$
\begin{aligned}
P =& E_\nu + \gamma_1 \frac{\hbar^2}{2m_0}(k_x^2 + k_y^2 + k_z^2) \\
Q =& \gamma_2 \frac{\hbar^2}{2m_0}(k_x^2 + k_y^2 - 2k_z^2) \\
R =& \sqrt{3}\frac{\hbar^2}{2m_0}(\gamma_3(k_x^2 - k_y^2) - 2i\gamma_2 k_x k_y) \\
S =& 2\sqrt{3}\gamma_3 \frac{\hbar^2}{2m_0} k_z(k_x - ik_y)
\end{aligned}
\tag{4.5.10}
$$

The Luttinger parameters $\gamma_1, \gamma_2, \gamma_3$ which describe the valence band are given by following equations

$$\frac{\hbar^2}{2m_0}\gamma_1 = -\frac{1}{3}(L + 2M) \tag{4.5.11}$$

$$\frac{\hbar^2}{2m_0}\gamma_2 = -\frac{1}{6}(L - M) \tag{4.5.12}$$

$$\frac{\hbar^2}{2m_0}\gamma_3 = -\frac{1}{6}(N) \tag{4.5.13}$$

can be adjusted for each semiconductor and are given in the table (4.1) for Si and different types of semiconductors, for more details see ref [115]. Figure 4.3 shows the band structure in the presence of the SO coupling compared to the one without SO coupling, and shows a lift of degeneracy between HH, LH and split-off bands unless at Γ where HH and LH bands are degenerate (blue line).

4.6 Description of the magnetic field

This part is concerned with the description of the effect of the magnetic field on the Hamiltonian.

The influence of the magnetic field is characterized by two effects. The first one come from the vector potential $\mathbf{A}$ (where the magnetic field $\mathbf{B} = \nabla \times \mathbf{A}$) which is introduced by replacing the wave vector $\mathbf{k}$ by $i\nabla + \frac{e}{\hbar}\mathbf{A}$. The term of the Hamiltonian due to the vector potential effect is written

$$H_A = -(3\kappa + 1)\mu_B \mathbf{B}.\mathbf{L} \tag{4.6.1}$$

where μ_B is the Bohr magneton, κ can be expressed in terms of Luttinger parameters [eq (4.5.10)] and $\mathbf{L}$ is the matrix representation of the orbital momentum of the Bloch function for $l = 1$.

The second effect is the Zeeman effect which is the action of the magnetic field on the spin. The Hamitonian is written

$$H_z = \frac{1}{2} g_0 \mu_B \sigma \mathbf{B} \tag{4.6.2}$$

where σ are the vectors of the Pauli matrix in the physical spin basis. The total effect of the magnetic field is the sum of the two effects

$$H_B = \mu_B \mathbf{B} K = \mu_B \mathbf{B}[-(3\kappa + 1)\mathbf{L} + g_0 \mathbf{S}] \tag{4.6.3}$$

where $\mathbf{K} = -(3\kappa + 1)\mathbf{L} + g_0\mathbf{S}$ and K_x, K_y and K_z in $\{j, m_j\}$ basis are given in appendix(A) and $\mathbf{S}$ is the spin of the hole.

4.7 Enveloppe function

In nanostructures, we decompose the whole wave function when the system is subjected to a slowly fluctuating external potential $U(r)$ at the atomic level [116] as a sum of envelope functions F_n multiplied by Bloch functions u_{n0}:

$$\psi(\mathbf{r}) = \sum_n F_n(\mathbf{r}) u_{n0}(\mathbf{r}) \tag{4.7.1}$$

Because of the slow variation of $U(r)$, we can decouple the action of $U(r)$ on F_n and u_{n0}. The wavefunction in 6-band k.p can be written as:

$$\psi(\mathbf{r}) = \sum_{jm_j} F_{jm_j}(\mathbf{r}) \otimes |j, m_j\rangle \tag{4.7.2}$$

Therefore the Schrödinger equation reads as:

$$[H_{6k.p}(-i\nabla) + U(\mathbf{r}).I_6]\tilde{F} = E\tilde{F} \tag{4.7.3}$$

where $H_{6k.p}$ is the Hamiltonian (4.5.9), I_6 is the identity matrix of dimension 6, k was replaced by the impulsion operator $-i\nabla$, and $\tilde{F}$ is enveloppe function vector for HH, LH and split-off bands.

4.8 Potential: Poisson

Thanks to the Poisson equation, it is possible to calculate the potential $V(\mathbf{r})$ applied by the gates of the transistor in which there is, in each different part in the device, a charge density $\rho(\mathbf{r})$ and a material of dielectric constant $\epsilon(\mathbf{r})$:

$$\nabla[\epsilon(\mathbf{r})\nabla V(\mathbf{r})] = -4\pi\rho(\mathbf{r}) \tag{4.8.1}$$

The equation is solved by the finite difference method where the relative dielectric permittivities of the different materials are: $\epsilon_{Si} = 11,7$, $\epsilon_{SiO_2} = 3,9$, $\epsilon_{Si_3N_4} = 7,5$.

The boundary conditions are :

- Periodicity of the device along the axis of the nanowire
- The potential applied to the grids.

The method consists in discretizing the volume into small volumes of the sample in the form of parallelepipeds defined by the nodes of the grid as seen in figure 4.4, each node is associated with its own potential V_i which corresponds to its charge Q_i and ϵ_i. We can obtain a system of linear equations (4.8.2) to calculate the potential by writing Gauss' theorem on each facet of the small parallelepiped of the grid:

$$AV = 4\pi(Q + Q_b) \tag{4.8.2}$$

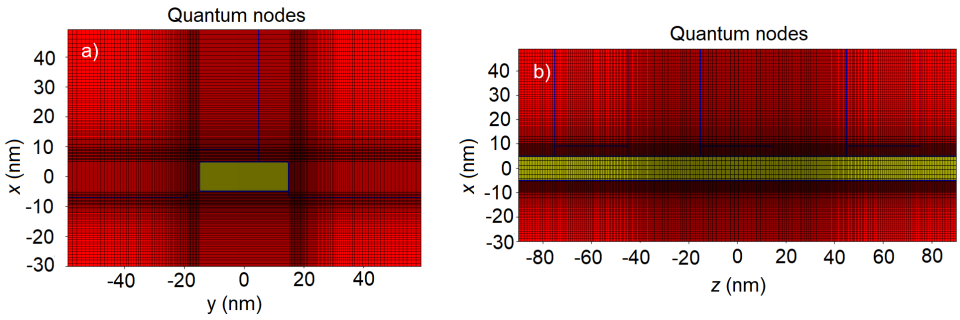

Figure 4.4: a) Transverse section (x,y) plane at z= 0 of a device. b) Longitudinal section (xz plane) at y=0 of a device. Both figures show a non-uniform mesh which is denser in the more active region.

where Q_b and Q are the vectors describing the boundary conditions, V is the potential vector to be calculated and A is a symmetric matrix. The equation is solved by the conjugate gradient method [117].

4.9 `TB_Sim` and device modeling

The simulations are performed with the `TB_Sim` code. The code has been developed for 15 years at CEA/INAC with contribution from other groups such as IEMN. `TB_Sim` is a multi-scale and multi-physics platform for the modeling of the structural, electronic, optical and transport properties of semiconductor nanostructures. It includes various modules for the calculation and diagonalization of arbitrary TB and k.p Hamiltonians, for the calculation of phonons and electron-phonons interactions, for the solution of Poissons equation, etc ... In this section, we will explain the operations of `TB_Sim` codes, which is illustrated in Figure 4.5. We need to calculate the energy states of the qubit, the wave functions, the Larmor frequency, and the potential response of the qubit. The geometry of the device in Figure 4.1 was described in section 4.2 of this chapter. In a first step of calculation, we mesh the device in a parallelpiped fashion. The mesh density differs between the different parts of the device. The active parts of the device, such as the silicon nanowire and the thin SiO_2 oxide layers, have the densest meshes. The less active parts of the device have a less dense mesh, such as the BOX, and always in a way to ensure the convergence of the numerical calculations. Periodic conditions along

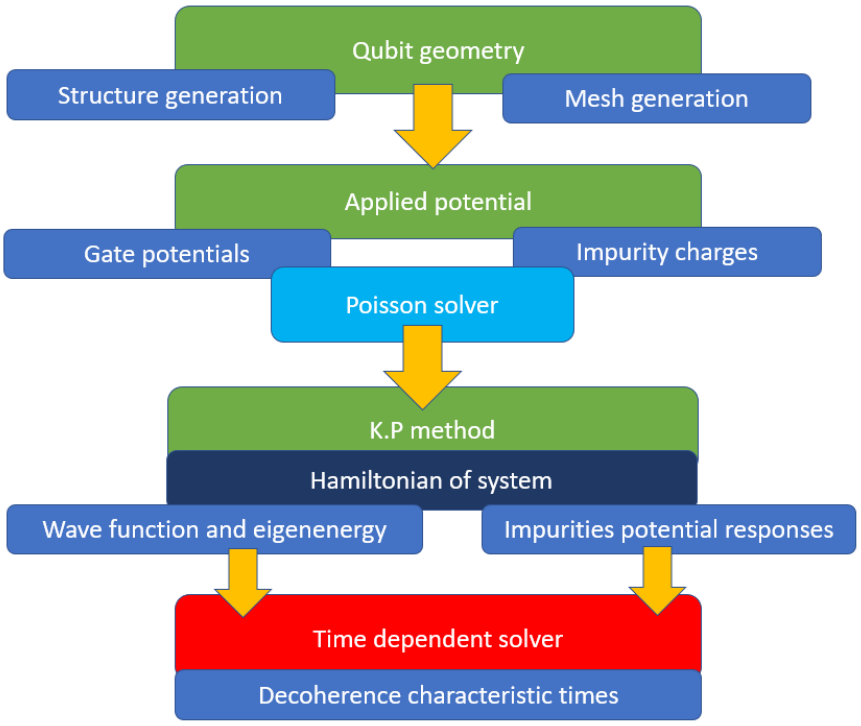

Figure 4.5: Computational infrastructure.

the axis of the nanowire (the z-axis in our case) are applied.

The second step is the application of the potential energy U on the grids using the electric potential obtained by solving the Poisson equation by the finite difference method.

In the third step, we solve the Schrödinger equation in order to obtain the energy levels and the associated wave functions. In the fourth step, we use these results to establish the potential response due to the presence of a charge impurity in the gate oxide. The calculation of the matrix elements of U is simply obtained by summing its components over all elements (boxes) of the 3D grid taking into account that the envelope functions and the electrostatic potential are slowly variable and the Bloch functions u_{n0} form an orthogonal basis. The fifth step aims at using the previous results to develop a model to calculate the qubit decoherence time due to a charge fluctuation in the oxide. This will be described in chapter 5.

4.10 Conclusion; outlook

In this chapter, we introduced the qubit geometry and the 6-band k.p. method for bulk semiconductor around Γ taking into account the spin-orbit coupling effect and the external magnetic field effect on the valence band structure of silicon. We described the methodology used to calculate the hole states of the qubit device. We have also briefly seen how to introduce numerically the Poisson equation which is solved by the finite difference method. Finally, we discussed the `TB_Sim` software infrastructure that was used to simulate the qubit in order to obtain results that will be interpreted and used for time-dependent simulations.

Chapter 5

Modelling

5.1 Introduction

In this chapter, we will model a charge fluctuator which responsible for a random telegraphic signal which is coupled to a hole qubit. The model aims to measure the qubit decoherence characterized by two processes: the relaxation and the dephasing designed by characteristic times T_1 and T_2, respectively. Two models have been developed, the first one is the two-level model which aims to get numerical results based on the solution of the time-dependent Schrödinger equation in order to compare them with the analytical result found in the litterature (chapter 2). The second model is the multi-level model in which we study the effect of the coupling of the two-level system (standard qubit) to other high energy states and investigate its influence on the qubit decoherence.

5.2 Description of the trap: potential of a point charge

There are several models that describe a charge fluctuator. The model adopted in this thesis consists of an impurity or a point defect in the gate oxide layer, assuming that it is located at 0.6 nm from the gate of the transistor. This defect

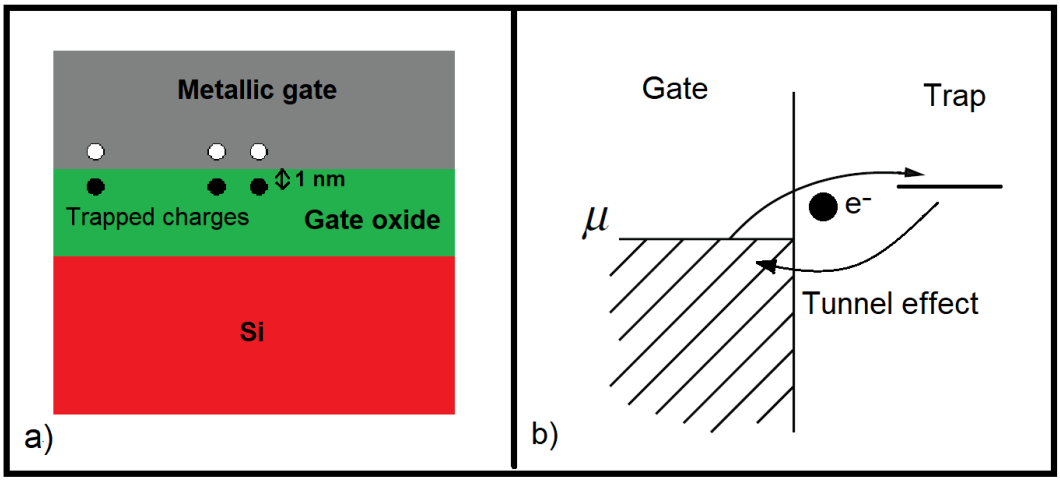

Figure 5.1: a) A diagram exhibiting localized charges traps close to a gate electrode. Local dipoles produced by induced image charges interact with the qubit. b) A hypothetical scenario in which electrons jump between a localized state and a typical metal. Inspired from ref [16].

induces a change in the band structure of the oxide so as to create a deep potential well capable of trapping an electron. Due to its proximity to the gate and the fact that its energy level is close to the Fermi level of the gate metal as shown in Figure 5.1, the transfer of an electron from the gate to the trap (potential well) and vice versa is done by tunneling effect, resulting in a charge fluctuator. The presence of an electron in the trap creates an additional potential in the qubit environment. This potential would not have much influence on the qubit coherence if the electron was permanently confined in the trap, but the fact that it is moving between the trap and the gate makes it quasi-static due to its limited and stochastic motion between two nearby positions in the device. Another effect that appears due to the proximity of the trap charge to the gate is the image charge effect where an opposite charge is created in the gate as shown in Figure 5.1 a. The electrons in the metal react to the presence of the trapped charge. In the case of a planar interface between two semi-infinite medium (metal plus oxide), this response can be described by an opposite charge located in the metal [118]. We end up with the potential of two opposite charges close to each other, thus a dipole.

The trapped charge plus its image behaves as an electrostatic dipole. Numerically, the electrostatic potential V is calculated by solving the Poisson equation

in the system when a charge is added to the oxide under the gate. This potential thus includes the direct potential of the charge plus the potential induced by the dielectric response of the system including metal gate.

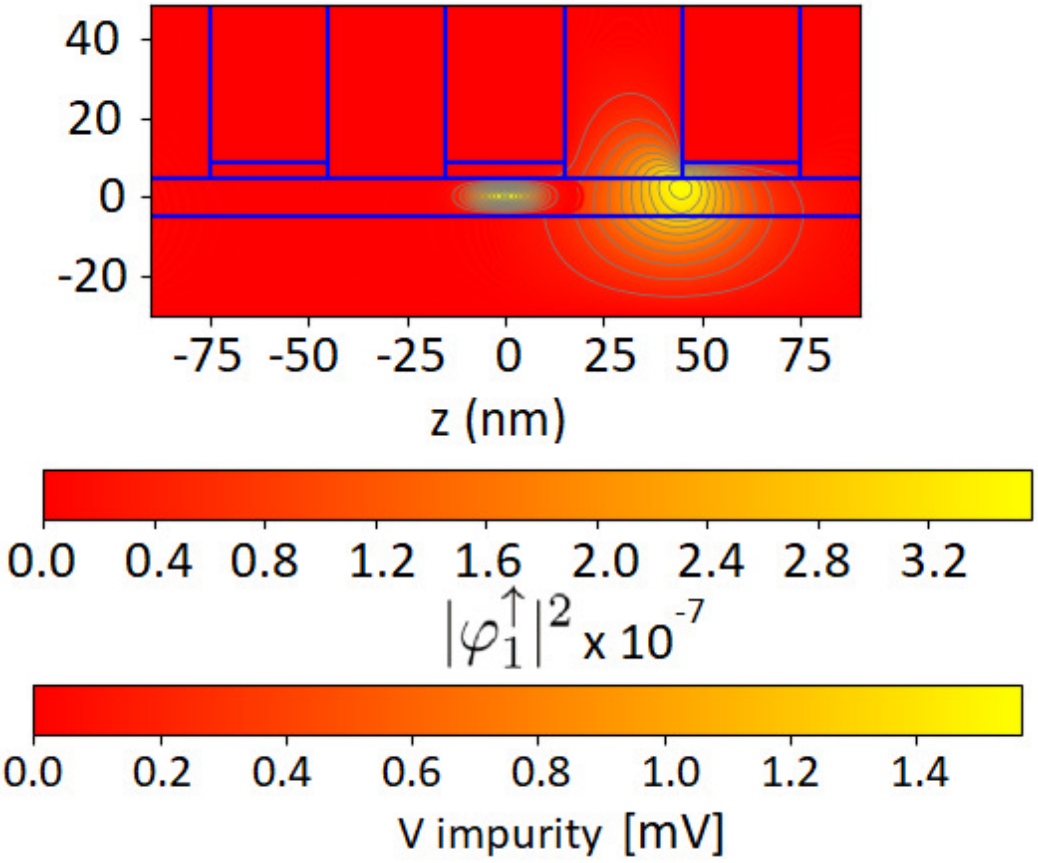

Figure 5.2: Probability density for the hole wavefunction $[|\varphi_1^{\uparrow}|^2]$ located under the central gate shown in a longitudinal section of the device [xz plane, $y = 0$]. The electrostatic potential induced by a single charge placed under the second gate is also shown.

5.3 Time-dependent Hamiltonian

We consider a charge fluctuator coupled to the hole qubit (Figure 5.1 a). The time-dependent Hamiltonian of the system reads as

$$H(t) = H_0 + \chi(t)U \tag{5.3.1}$$

H_0 represents the hamiltonian of the qubit system under a static magnetic field **B** with no electrical perturbation. The charge fluctuator mathematically expressed by perturbation U and a random telegraphic signal $\chi(t)$ which describe the filling of a localized charge trap in the oxide layer at a distance of 0.6 nm from a metallic gate. When a charge is on the trap, the perturbation is defined by U. For exemple Figure 5.2 is a longitudinal section of studied device (Figure 4.1) which shows the probability density of the hole wavefunction $[|\varphi_1^{\uparrow}|^2]$ and the electrostatic potential produced by a confined charge $-e$ underneath the secondary gate. The charge fluctuator is defined as a quasi-static noise [17], where $\chi(t)$ at instant t can take one of two values, 0 or 1 (equation (2.5.3)), with corresponding probabilities p_0 and p_1. If $\chi(t) = 0$, that means the trap is empty else if $\chi(t) = 1$, that means an electron of charge $-e$ has tunneled from the gate to the trap and fills it. The tunneling transition rate for the process $0 \to 1$ is $\nu_{0\to1} = \nu[1 - f_{FD}(\varepsilon_0)]$ where the tunneling rate is ν, f_{FD} is the Fermi-Dirac distribution function, and the location of the trap level in comparison to the Fermi level in the reservoir (gate) is ε_0. In order to simplify the problem, we suppose that $\varepsilon_0 = 0$, $\nu_{0\to1} = \nu/2$, $\nu_{1\to0} = \nu - \nu_{0\to1} = \nu/2$, $p_0 = p_1 = 1/2$ [91]. The numerical treatment of the case of asymmetric tunneling ($\nu_{0\to1} \neq \nu_{1\to0}$) would be straighforward but does not lead to situations with very different physics since, in particular, we will consider a tunneling rate in a wide frequency range.

5.4 Time dependent simulations

In order to study the influence of a simple charge fluctuator on the qubit leading to decohence, it is necessary to calculate the characteristic times T_1 (designing the relaxation process), T_1'(defined later), and T_2 (dephasing process) which will be discussed in the next sections. Then we need to calculate the time evolution of the wavefunction $|\psi(t)\rangle = e^{\frac{-i}{\hbar}\int_0^t H(t')dt'}|\psi(0)\rangle$ which represents the solution of the time dependent Schrödinger equation:

$$i\hbar\frac{d|\psi(t)\rangle}{dt} = H(t)|\psi(t)\rangle \tag{5.4.1}$$

$|\psi(t)\rangle$ is written as a linear combination of the hole states $|\varphi_i^{\uparrow}\rangle$ and $|\varphi_i^{\downarrow}\rangle$:

$$|\psi(t)\rangle = c_1^{\uparrow}(t)|\varphi_1^{\uparrow}\rangle + c_1^{\downarrow}(t)|\varphi_1^{\downarrow}\rangle + c_2^{\uparrow}(t)|\varphi_2^{\uparrow}\rangle + c_2^{\downarrow}(t)|\varphi_2^{\downarrow}\rangle + ... \tag{5.4.2}$$

Here we assumed that the states are ordered, $|\varphi_1^{\uparrow}\rangle$ and $|\varphi_1^{\downarrow}\rangle$ being the ground states, i.e. on an electronic energy diagram, the highest states of the valence band. Numerically, we used a Chebychev polynomial expansion for the resolution of the time propagation of the wave function equation with great precision and fidelity [119].

Chebychev polynomial expansion

The Chebychev method is a polynomial method where the propagator $e^{-iHt/\hbar}\psi$ can be expressed as a polynomial expansion as

$$e^{-iHt/\hbar}\psi = \sum_n a_n P_n(H)\psi \tag{5.4.3}$$

where $P_n(H)$ is a polynomial whose action on ψ can be evaluated by iteration of H on ψ, and a_n are coefficients. $P_n(H)\psi$ can be calculated for any polynomial of H of bounded spectrum $[E_{min}, E_{max}]$. The method consists to expand the propagator in terms of Chebyshev polynomials. For the exponential function, the expansion has the form

$$e^{-i\alpha x}\psi = \sum_n a_n(\alpha)\Phi_n(-ix) \tag{5.4.4}$$

where

$$a_n(\alpha) = \int_{-i}^{i} \frac{e^{-i\alpha x}\Phi_n(x)}{\sqrt{1-x^2}}dx = 2j_n(\alpha) \tag{5.4.5}$$

and

$$a_0(\alpha) = j_0(\alpha) \tag{5.4.6}$$

where $j_n(\alpha)$ are Bessel functions. The Chebyshev recurrence relation is

$$\Phi_{n+1}(x) = 2x\Phi_n(x) + \Phi_{n-1}(x) \tag{5.4.7}$$

the expanded wavefunction becomes

$$\psi(t) = e^{-i(E_{min}t/\hbar+\alpha)} \sum_n a_n(\alpha)\Phi_n(-iH_{norm})\psi(0) \tag{5.4.8}$$

where H_{norm} is the renormalized Hamiltonian of bounded spectrum $[-1, 1]$

$$H_{norm} = 2\frac{H - I[(E_{max} - E_{min})/2 + E_{min}]}{E_{max} - E_{min}} \tag{5.4.9}$$

I is the identity matrix and $\alpha = \frac{(E_{max}-E_{min})t}{2\hbar}$.

The polynomials is generated by the recurrence relation

$$\phi_{n+1} = -2iH_{norm}\phi_n + \phi_{n-1} \tag{5.4.10}$$

with

$$\phi_n = \Phi_n(-iH_{norm})\phi(0) \quad \phi(0) = \psi(0) \quad \phi_1 = -iH_{norm}\psi(0) \tag{5.4.11}$$

The iteratively time-ordering Chebychev propagator is efficient and accurate. The error is distributed over the whole range of eigenvalues. For more details see ref [120].

5.4.1 Two-level model

Relaxation process: T_1

The two-level model holds when $|\psi(t)\rangle$ remains within the doublet $|\varphi_1^{\uparrow}\rangle$ $|\varphi_1^{\downarrow}\rangle$ during its evolution with time. The energy difference between the two states is the Zeeman splitting $g\mu_B B = \hbar\Omega$ in absence of perturbation. The matrices (chapter 2)

$$H_0 = \frac{\hbar}{2}\begin{pmatrix} \Omega & 0 \\ 0 & -\Omega \end{pmatrix} \quad U = \begin{pmatrix} u_{\uparrow\uparrow} & u_{\uparrow\downarrow} \\ u^*_{\uparrow\downarrow} & u_{\downarrow\downarrow} \end{pmatrix} \tag{5.4.12}$$

are calculated numerically as described in the previous chapter. The coupling terms (the non-diagonal elements of the matrix U) and the difference $u_{\uparrow\uparrow} - u_{\downarrow\downarrow}$ result from the spin-orbit coupling and the time reversal symmetry breaking under the action of the magnetic field B which is detailed in the appendix B.

We define the Pauli matrices $\sigma_1 = \begin{pmatrix} 0 & 1 \\ 1 & 0 \end{pmatrix}$, $\sigma_2 = \begin{pmatrix} 0 & -i \\ i & 0 \end{pmatrix}$, $\sigma_3 = \begin{pmatrix} 1 & 0 \\ 0 & -1 \end{pmatrix}$ in the basis $\{|\varphi_1^{\uparrow}\rangle, |\varphi_1^{\downarrow}\rangle\}$ which cannot be confused with σ_x, σ_y, σ_z in which x, y, z refer to the axes of the system.

Defining $\boldsymbol{\sigma}$ as the vector of Pauli operators, we calculate the observable (see also equation (2.5.12))

$$\langle\langle \boldsymbol{\sigma}(t) \rangle\rangle = \langle \psi(t) | \boldsymbol{\sigma} | \psi(t) \rangle_{\{E\}} \tag{5.4.13}$$

where $\psi(t)$ is the wave function solution of the time dependent Schrödinger equation. The index $\{E\}$ represents the average over a large number of realizations of the telegraphic signal in order to obtain converged results. So to measure the relaxation, it is enough to calculate $\sigma_{\parallel}(t) = \langle\langle \sigma_3(t) \rangle\rangle$ which represents the projection of the effective spin on the magnetic field axis $e_{\parallel}$.

We consider the initial condition $|\psi(0)\rangle = |\varphi_1^{\uparrow}\rangle$. It should be noted that, since we study the system in a semi-classical way, the system reaches a situation of an equal statistical superposition of the two states $|\varphi_1^{\uparrow}\rangle$ and $|\varphi_1^{\downarrow}\rangle$, $\sigma_{\parallel}(\infty) = 0$ (see Appendix D).

The results of the calculations will be presented an discussed in chapter 6. $\sigma_{\parallel}(t)$ shows an exponential decay from which we deduce T_1.

Dephasing process: T_2

The dephasing is the process coming from the change of the spin precession phase with time designed by $\delta\Phi(t)$ due to the perturbation induced to the initial Hamiltonian of the qubit H_0 by $\chi(t)U$. In this case, the Larmor frequency Ω turns into Ω' where $\hbar\Omega'$ represents the new Zeeman splitting energy calculated by diagonalization of $H_0 + U$ and which is discussed in chapter 6. The best method to measure the dephasing is to calculate the quantity

$$m(t) = |\langle\langle \sigma_1(t) \rangle\rangle + i \langle\langle \sigma_2(t) \rangle\rangle| \tag{5.4.14}$$

which is the modulus of the mean of the spin projection in the plane perpendicular to $\mathbf{B}$ and gives the evolution of the phase of the spin precession. An important point in the calculation of T_2 is to take as initial condition $|\psi(0)\rangle = \frac{1}{\sqrt{2}}(|\varphi_1^{\uparrow}\rangle + |\varphi_1^{\downarrow}\rangle)$ corresponding to the spin in the plane. The results fitted with a negative exponential give the decay constant T_2 in this case.

5.4.2 Multi-level model

A quantum dot like the one that forms our qubit is not limited to only two states. There are many states that are more distant in energy than the doublet studied in the case of the two-level model. They are usually neglected considering that the coupling with these states is negligible and the qubit in its turn is considered as a two-state system. In this section, we take into account the coupling with these distant states in order to see their influence on the characteristic decoherence times T_1 and T_2. We then consider that the qubit contains $2N$ states and we represent H_0 and U in the basis $\{\varphi_1^{\uparrow}, \varphi_1^{\downarrow}, \varphi_2^{\uparrow}, \varphi_2^{\downarrow}, ..., \varphi_N^{\uparrow}, \varphi_N^{\downarrow}\}$. T_1 and T_2 are calculated in the same way as in the two-level model but assuming non-zero terms of matrices of σ_1, σ_2, σ_3 only in the subspace $|\varphi_1^{\uparrow}\rangle, |\varphi_1^{\downarrow}\rangle$.

The initial conditions are unchanged. The norm of the wave function in the two-state model $\left|\langle\varphi_1^{\uparrow}|\psi(t)\rangle\right|^2 + \left|\langle\varphi_1^{\downarrow}|\psi(t)\rangle\right|^2$ remains equal to 1, whatever t. This is non longer the case in the multi-level model. This is due to the fact that all states are coupled together by the non-diagonal elements of the U-matrix and that for $t \to \infty$ the weight of the wave function is distributed over all states, which will be discussed in chapter 6. For this purpose, we introduce a new quantity called $p_1(t) = \left|\langle\varphi_1^{\uparrow}|\psi(t)\rangle\right|^2 + \left|\langle\varphi_1^{\downarrow}|\psi(t)\rangle\right|^2$ which represents the sum of the wave function weights on the doublet states. It is clear that $p_1(t)$ will constrain T_1 and T_2 since they are calculated as a function of $|\varphi_1^{\uparrow}\rangle$ and $|\varphi_1^{\downarrow}\rangle$. We then associate with $p_1(t)$ the characteristic time T_1' and which is calculated by fitting $\langle p_1(t)\rangle_{\{E\}}$ with a negative exponential as in the case of T_1 and T_2.

5.5 Conclusion; outlook

In this chapter, we modeled a charge fluctuator coupled to a hole qubit. We used the solution of the time-dependent Schrödinger equation to compute the eigenvector $\psi(t)$ using the Chebyshev polynomial expansion. Two models have been developed: the first one at two levels aims at verifying the analytical results of chapter 2 and the second one at several levels is used to study the influence of

several states (> 2) on the decoherence. The next chapter will be devoted to the discussion of the results obtained from the simulations of the developed models and to the conclusion.

Chapter 6

Results of time-dependent simulations

6.1 Introduction

In this chapter, we will discuss the results obtained from the models developed in chapter 5. For this purpose, we will introduce different configurations of the charges trapped in the device and the potential applied on the gates. In addition, we will introduce the wave functions of the holes created in the device. We will discuss the time-dependent simulations and the calculation of characteristic times corresponding to each entity. We will discuss the results obtained by the time-dependent simulations comparing them with the analytical model found in the literature and then we will discuss the calculations made to optimize the effects of the charge fluctuators on the qubit coherence time.

6.2 Description of the studied situations: position of the traps (Trap 1, 2 and 3)

In this section, we show the different trap positions that lead to the creation of a charge fluctuator. We assume three different electronic trap positions in the qubit

Table 6.1: Studied charge traps. Position: The coordinates x, y and z are defined with respect to the axes specified in figure 4.1. Characteristics deduced from the perturbation matrix U : angular frequency $\omega_{th} \approx |u_{\uparrow\uparrow} - u_{\downarrow\downarrow}|/\hbar$ and $|u_{\uparrow\downarrow}|$ is the modulus of the non-diagonal matrix element. With Larmor frequency $\Omega = 2\pi \times 10^{10}\ rad/s$.

Trap	x	y	z	Gate	ω_{th}	$\lvert u_{\uparrow\downarrow}\rvert$
	(nm)				(s^{-1})	(μeV)
Trap 1	8.4	0.0	0.0	Central	1.063×10^9	1.4594
Trap 2	8.4	4.0	14.0	Central	5.469×10^8	0.4381
Trap 3	8.4	0.0	46.0	Secondary	3.039×10^7	0.0248

device studied in this thesis. One of them is described in Figure 6.1. Table 6.1 shows the x, y and z coordinates of each trap in the device. We consider traps located in the oxide, sufficiently close to a metallic gate to allow charge tunneling between the trap and the metal. Trap 1 and Trap 2 are located in the oxide under the central gate and Trap 3 is located under the secondary gate of the device. Each of these traps is separated from the gate by a distance of 0.6 nm.

Figure 6.1 represents a cross section (xy plane) at $z = 0$ of the device in which an electron in Trap 1 is sketched. It appears as a small blue point in the oxide layer between the nanowire and the gate. Trap 1 induces the highest perturbation potential, as shown by ω_{th} and $u_{\uparrow\downarrow}$ in table 6.1, due to its proximity to the center of the device where the hole qubit is located. As the distance between the trap and the hole qubit increases, perturbation potentials become lower as shown in Table 6.1 for Traps 2 and 3. The components of U approximately behave as d/r^2 where d is the length of the dipole and r is the distance from the dipole to the hole.

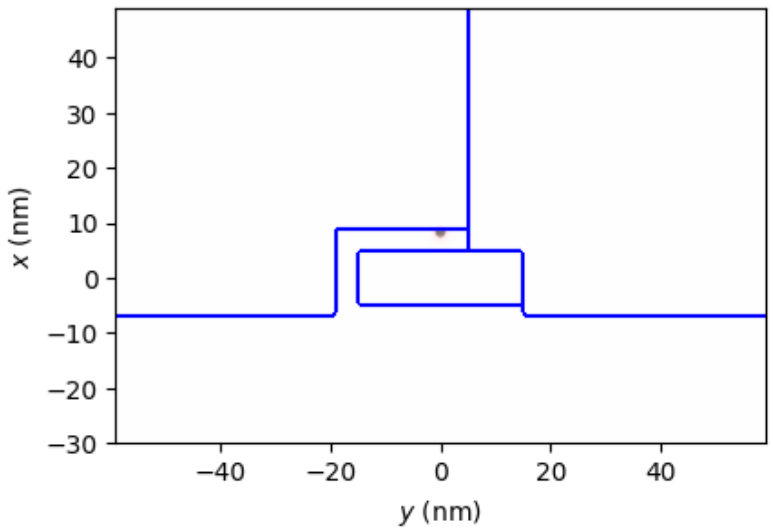

Figure 6.1: Transverse [xy plane at $z = 0$] cross section of the device. A single charge on Trap 1 at position $x = 8.4$ nm, $y = 0$ and $z = 0.0$ nm is represented by a blue point.

6.3 Potential

Except otherwise stated, we apply on the central gate a bias of -0.1 V, the secondary gates and the back gate are grounded. Figures 6.2 represent the potential in the transversal section (xoy plane) at $z = 0$ and the longitudinal section (xoz plane) at $y = 0$. The potential has a critical role to assure the confinement required along z to create the qubit in the nanowire under the central gate.

6.4 Electronic structure, wavefunctions

Figure 6.3 represents the 3D device in which the red part represents the ground state wave function calculated by the 6-band KP model discussed in Chapter 4. It shows that the wave function is compressed on the side of the silicon nanowire under the central gate along y and well centered in the middle of the nanowire along z. By varying the potential applied to the different gates, we can control the position of the wave function inside the nanowire, which will modify the effect of the fluctuator on the coherence time of the qubit. This will be discussed in

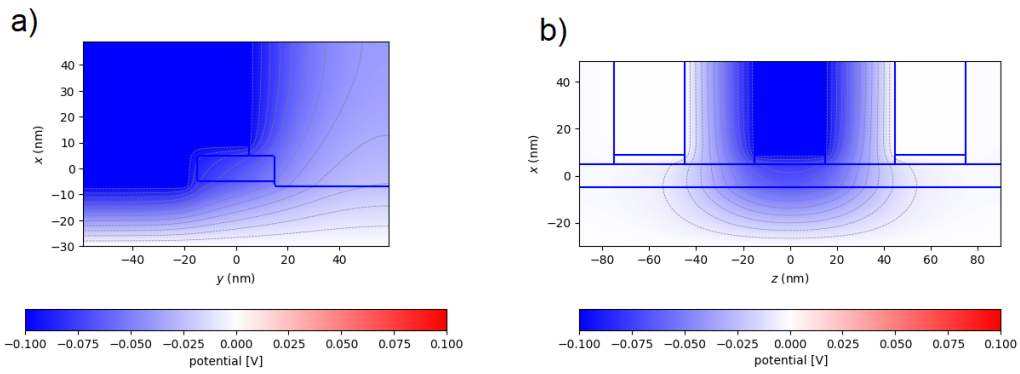

Figure 6.2: Potential for a bias applied on the central gate $V_{CG} = -0.1V$.

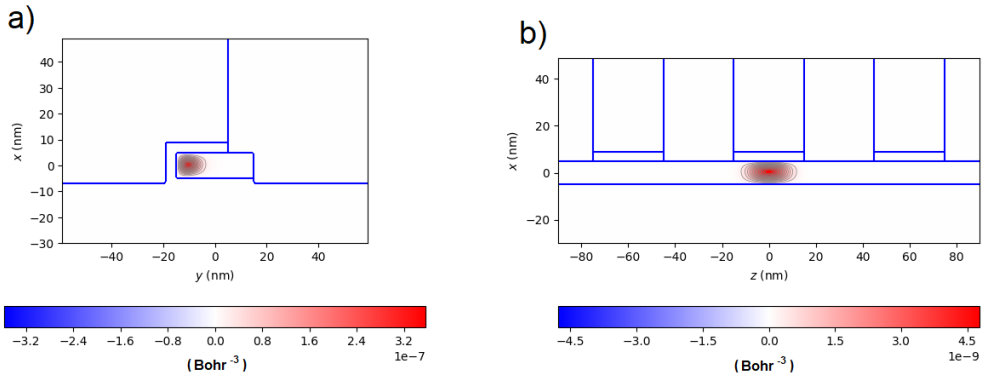

Figure 6.3: Iso-density surface of the ground-state qubit hole wave function seen according to (a) transverse [xy plane at $z = 0$] and (b) longitudinal [xz plane, $y = -10$ nm corresponding to the center of the hole wave function] sections.

section 6.10.

6.5 Time-dependent simulations: traces of σ_i

In this section, we will discuss the results obtained from time-dependent simulations for $\sigma_{\parallel}(t)$, $p_1(t)$ and $m(t)$ in order to derive the characteristic coherence times T_1, T_1' and T_2.

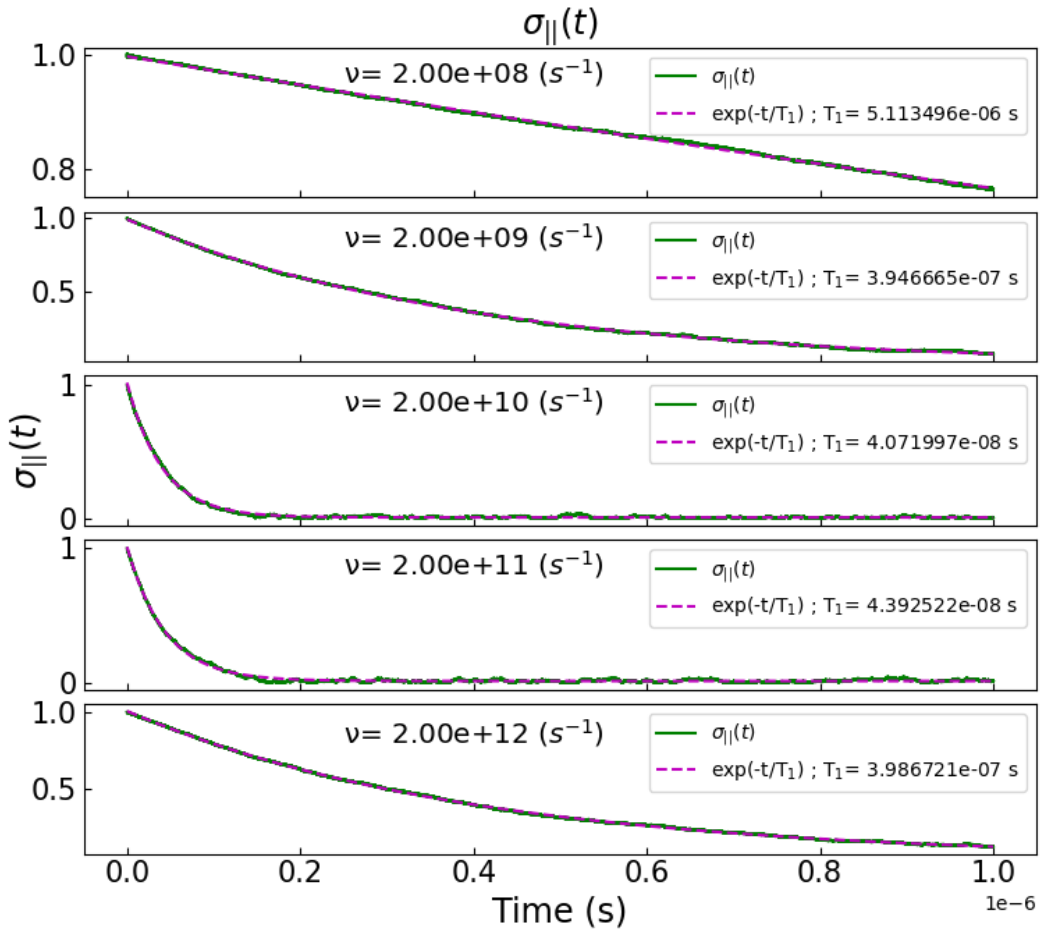

Figure 6.4: Evolution of $\sigma_{||}(t)$ for different fluctuator frequencies ν in the case of Trap 1, in the 2-level model. T_1 is given by the exponential decay fitting

6.5.1 2-level system

For the 2-level model, Figure 6.4 shows $\sigma_{||}(t)$ for different frequencies ν of the fluctuator. $\sigma_{||}(t)$ undergoes an exponential decay. The behaviour is different for $m(t)$ (figure 6.5). There are coherent oscillations which have been predicted by the analytical calculations when $\delta = \frac{1}{2}\sqrt{\nu^2 - \omega_{th}^2}$ in eq (2.5.22) becomes imaginary. They come from remanent coherent oscillations between the different realizations of the oscillators. For $\nu < \omega_{th}$, $m(t)$ undergoes oscillations with an envelope that decays exponentially. For $\nu = \omega_{th}$ there is only one oscillation so the decay is better described by a Gaussian function. For $\nu > \omega_{th}$, $m(t)$ undergoes an exponential decay, without oscillation. This type of behavior is described by the equation (2.5.22) of Chapter 2 which measures the visibility which represents $m(t)$ in the

case of pure dephasing.

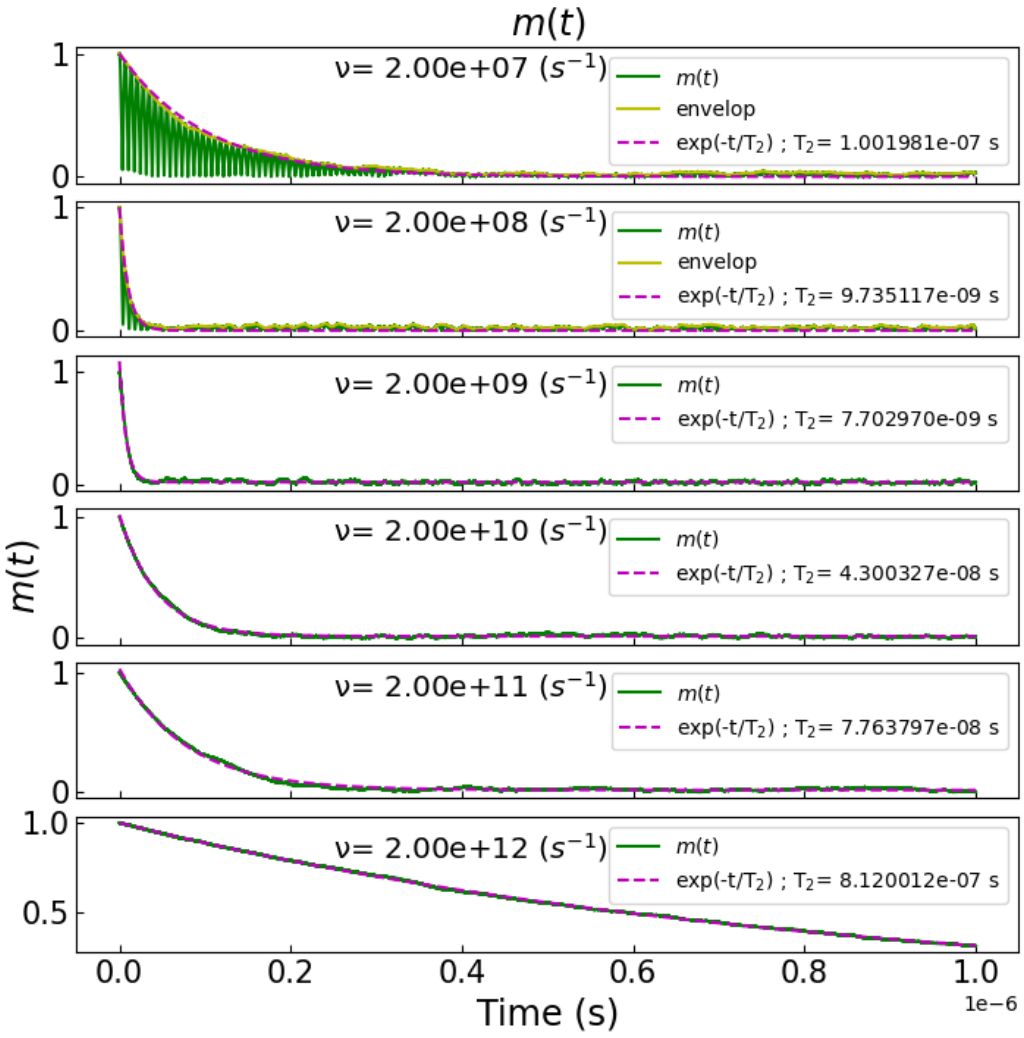

Figure 6.5: Evolution of $m(t)$ for different fluctuator frequencies ν of the case of Trap 1, in the 2-level model. For $\nu < \omega_{th} = 1.963 \times 10^9$ s^{-1}, $m(t)$ presents oscillations [17]. In this case, T_2 is given by the exponential decay of the envelope.

6.5.2 Multi-level system

The time-dependent simulations for Trap 1 are shown in Figures 6.6 and 6.7 where $\sigma_{\parallel}(t)$ and $m((t)$ are calculated with the method discussed in Chapter 5 for the multi-level model.

Figure 6.8 shows calculations of $p_1(t)$ introduced in chapter 5. $p_1(t)$ represents the weight of the wavefunction on the first two states $\varphi_1^{\uparrow}$ and $\varphi_1^{\downarrow}$. The 2-level model is

valid when $p_1(t) \approx 1$. The results show that $p_1(t)$ undergoes an exponential decay but does not tend to zero contrary to $\sigma_{\parallel}(t)$ and $m(t)$. $p_1(t)$ tends to $2/2N$ where $2N$ is the number of levels which is equal to 20 in this case.

In a 2-level quantum system, the relaxation should normally be the transition $|\uparrow\rangle \rightarrow |\downarrow\rangle$, i.e. on the Bloch sphere, it is the transition along the Z axis, $+1 \rightarrow -1$. But as we see, $\sigma_{\parallel}(t)$ tends to 0, i.e. the final state is an equal superposition of two states. In other words, over time, if we start from $\psi(t=0) = |\varphi_1^{\uparrow}\rangle$, the final state can be written as $|\psi(t=\infty)\rangle = \alpha|\varphi_1^{\uparrow}\rangle + \beta|\varphi_1^{\downarrow}\rangle$ where $|\alpha|^2 = |\beta|^2 = 1/2$. Then, in this case, the weight of the final wavefunction is equi-distributed on all the states of the basis taken into account and this comes from the fact that the system is studied in a semi-classical way where the spontaneous emission and dissipation are not taken into account. This explains the fact that, in the multi-level model, the weight on the first two states expressed in $p_1(t)$ tends to $2/2N$, as the final state is equi-distributed on all states of the basis, and then $\sigma_{\parallel}(t)$ tends to 0. The mathematical demonstration of this reasoning is given in appendix (D).

6.5.3 Fit and determination of characteristic times

In order to extract the characteristic times corresponding to $\sigma_{\parallel}(t)$, $m(t)$, $p_1(t)$, the curves are fitted with a function $f(x) = e^{(-t/\tau)} + b$, where τ is the characteristic time which represents either T_1, T_2, T_1', and b is a constant equal to 0 in the case $\sigma_{\parallel}(t)$ and $m(t)$, different from 0 for $p_1(t)$.

6.6 Numerical limitations

We consider a magnetic field of 0.2712 T oriented along the direction characterized by $\theta = 90°$ and $\varphi = 45°$ (figure 4.1) which leads to a Larmor frequency $\Omega/(2\pi)$ of 10 GHz. This forces us to use a time step of 10^{-12} s for the numerical solution of the time-dependent Schrödinger equation for $\nu \leq 2 \times 10^{11}$ s^{-1}, 10^{-13} s for $\nu = 2 \times 10^{12}$ s^{-1}, 10^{-14} s for $\nu = 2 \times 10^{13}$ s^{-1} and 10^{-15} s for $\nu = 2 \times 10^{14}$ s^{-1}. The maximum simulation time has been limited to 10^{-4} s. We thus considered

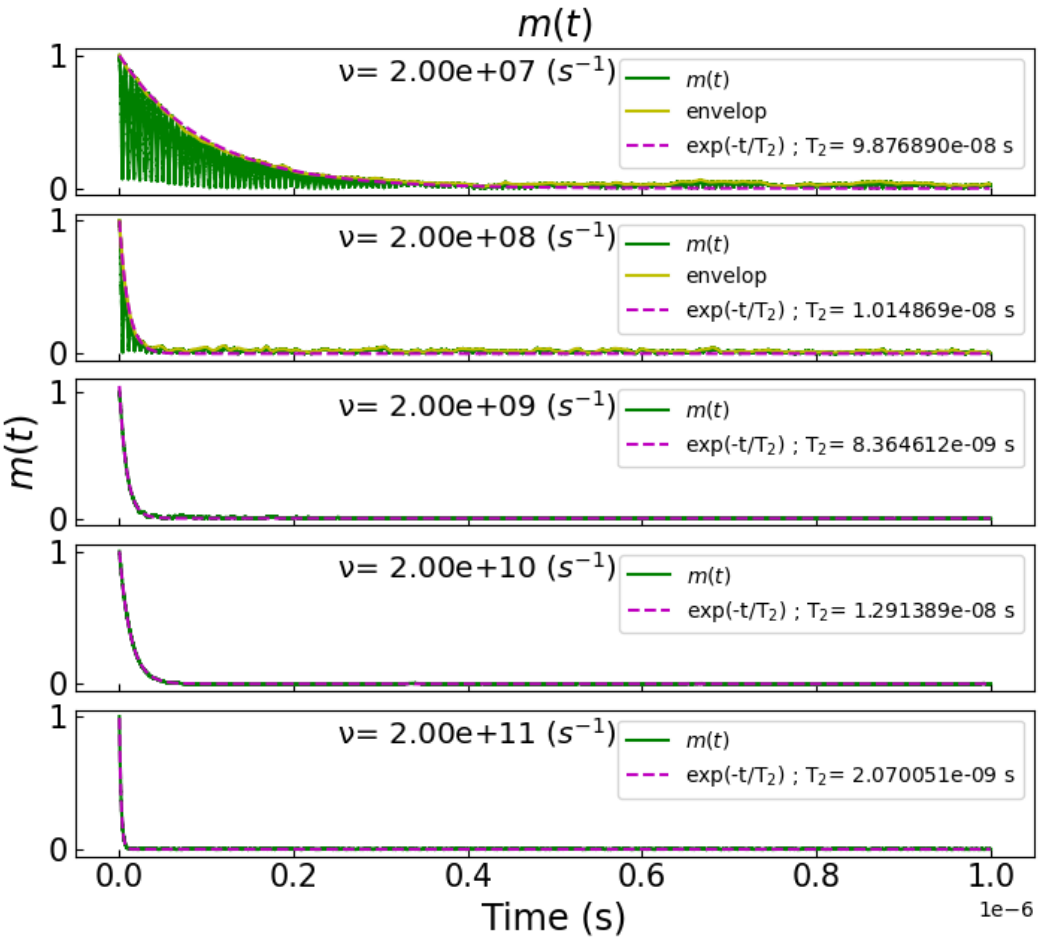

Figure 6.6: Evolution of $m(t)$ for different fluctuator frequencies ν in the case of Trap 1, in the multi-level model. $m(t)$ presents oscillations for $\nu < \omega_{th}$ as in figure 6.5. In this case, T_2 is given by the exponential decay of the envelope.

ν between 2×10^6 s^{-1} and 2×10^{14} s^{-1}. However, the laws of variation of the characteristic times as a function of ν will allow us to extrapolate them to smaller tunneling rates ν which often characterize telegraphic noises at low temperatures [17].

6.7 Coherence times in 2-level model

In this section, we interpret the characteristic times in the 2-level model by comparing the numerical results obtained by time-dependent calculations with analytical ones already developed in chapter 2. The 2-level model is a special case of the

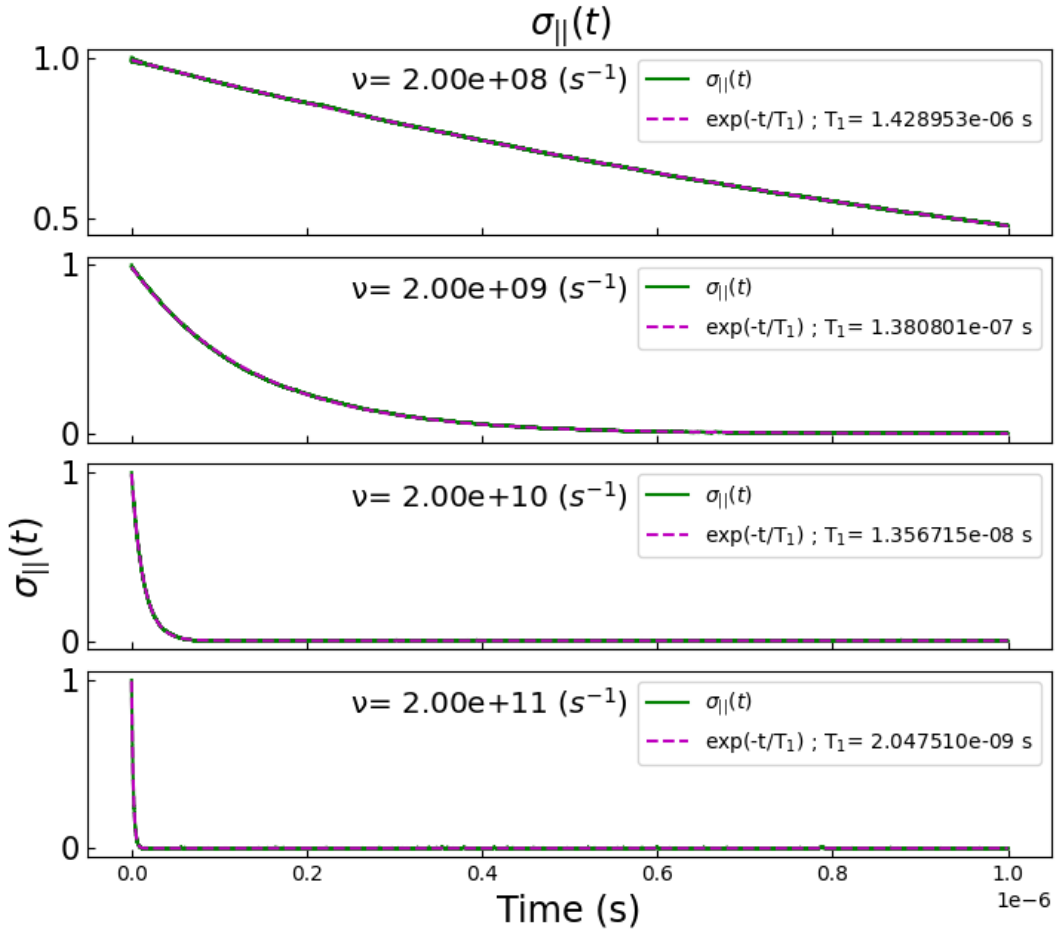

Figure 6.7: Evolution of $\sigma_{\parallel}(t)$ for different fluctuator frequencies ν in the case of Trap 1, in the multi-level model. T_1 is given by the exponential decay fitting.

multi-level model where $N = 1$. The results of this model will help us to better understand the results of the multi-level model.

Equation (2.5.29) shows that T_2 depends on the relaxation time T_1 and the dephasing time T_2^* of the pure dephasing model. From a mathematical point of view, T_2^* depends on the diagonal element of the perturbation matrix U (equation 5.4.12). The dephasing arises from the phase shift $\delta\varphi$ which represents the change in spin precession due to the random variation of the time-dependent Hamiltonian described by $\chi(t)U$. This results in the change of the Larmor frequency from $\Omega \to \Omega'$ over time where $\hbar\Omega'$ is the splitting energy obtained by the diagonalization of $H_0 + U$. In the section (6.10.1), we show how to calculate the angular frequency ω_{th} in a general way and which gives the pure dephasing case $\omega_{th} = |u_{\uparrow\uparrow} - u_{\downarrow\downarrow}|/\hbar$.

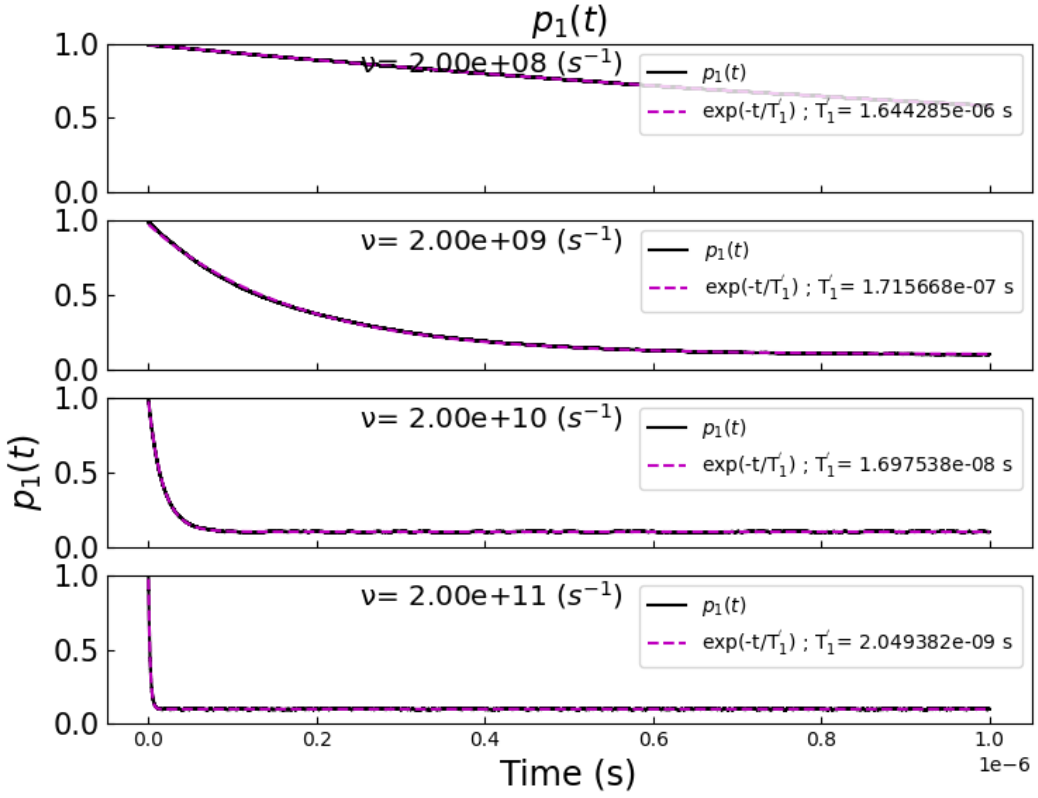

Figure 6.8: Evolution of $p_1(t)$ for different fluctuator frequencies ν in the case of Trap 1, in the multi-level model. $T_1^{'}$ is given by the exponential decay fitting.

$|u_{\uparrow\uparrow} - u_{\downarrow\downarrow}|$, written as $|u_1^{\uparrow\uparrow} - u_1^{\downarrow\downarrow}|$ in the multi-level model, presented in Figure 6.10 c, represents the change of the energy splitting in the case of pure dephasing.

Figure 6.9 shows that the results of numerical simulations are in correspondence with the analytical results. The curve of T_2 is formed by two different parts. For frequencies $\nu >> \omega_{th}$, the number of qubit spin phase variations is large in time $\approx \pi/\omega_{th}$. These phase variations can be described by a Gaussian distribution in this frequency range. So, in this Gaussian regime, the pure dephasing process is characterized by $T_2^* = 4\nu/\omega_{th}^2$ [16, 17]. T_2^* has a linear dependence on ν [16, 17] because the 2-level system becomes more insensitive to the random disturbance once the frequency of this disturbance increases. In the low frequency range $\nu << \omega_{th}$, the Gaussian approximation is no longer valid. The phase variation time $2\pi/\omega_{th}$ is much smaller than the switch time $1/\nu$ and then there are not enough switches in a time equal to $2\pi/\omega_{th}$ to describe a Gaussian distribution of events.

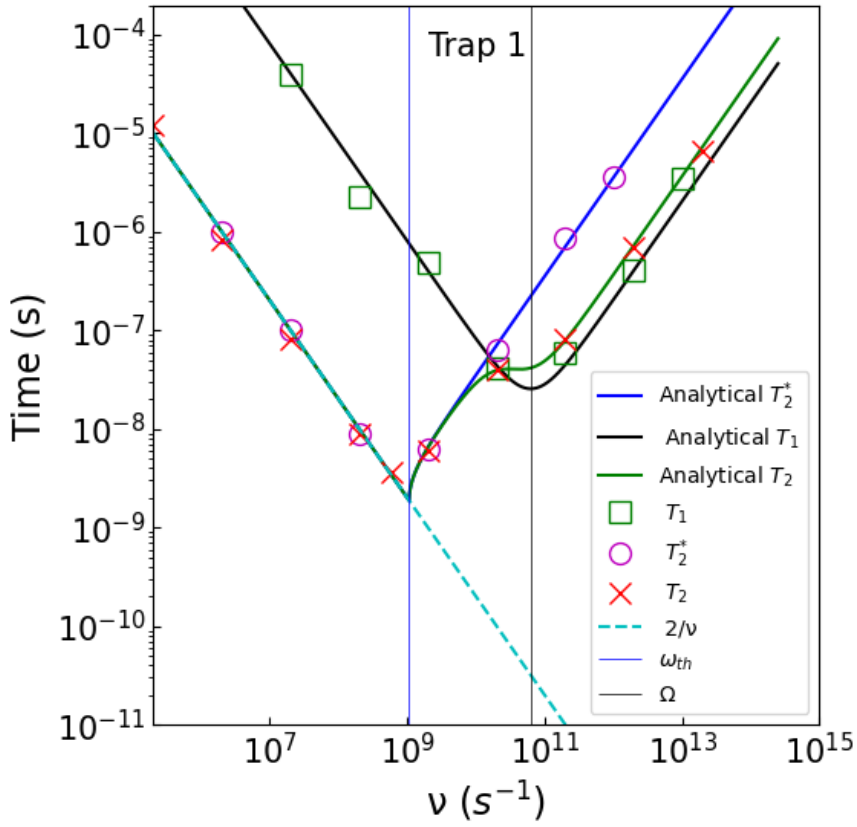

Figure 6.9: Characteristic times T_1 (green squares) and T_2 (red crosses) versus tunneling frequency ν calculated numerically in the 2-level model for Trap 1. Lines represent the analytical expressions for T_1 (black) given by equation (2.5.28) and T_2^* (light blue) given by equation (2.5.23), T_2 (green) given by equation (2.5.29), with ω_{th} and $|u_{\uparrow\downarrow}|$ of Table 6.1. The straight dashed turquoise line shows a time varying as $2/\nu$. At $\nu \gg \Omega$, $T_2 \approx 2T_1$.

It will be clear (in the low frequency range) that the dephasing depends only on the fluctuator frequency, which is shown in Figure 6.9 where $T_2 = T_2^* = 2/\nu$. The $2/\nu$ line means that the qubit loses its coherence when the fluctuator undergoes its first switch.

T_2^* for any frequency in the pure dephasing model is given by equation (2.5.23) where $\omega_{th} = |\Omega - \Omega'|$ represents the angular frequency that separates the Gaussian and non-Gaussian regime. Figure 6.9 also shows that the dephasing time T_2 is determined by T_1 and T_2^*, as shown in equation (2.5.29), with T_1 being the characteristic time of the relaxation process.

The results of the numerical calculation of T_1 correspond well with the analytical equation (2.5.28). Figure 6.9 shows that the qubit + fluctuator system enters in

resonance for $\nu = \Omega$, when the fluctuator frequency and the qubit spin precession frequency (Larmor frequency) are equal.

The dephasing time T_2 calculated by the numerical simulation corresponds well with the analytical equation. The reason is that the change in the Larmor frequency $\Omega \rightarrow \Omega'$ is mainly determined by the diagonal term of U. In the frequency range $\nu < \omega_{th}$, $T_2 \approx T_2^*$. On the other hand, in the frequency range $\nu > \omega_{th}$, $T_2^* > T_1$. And therefore, from equation(2.5.29), we can deduce that $T_2 \approx 2T_1$. The dependence of T_2 on T_1 and T_2^* represents a coupling between the two phenomenon, the relaxation and the dephasing, which can be explained by the fact that $u_{ij} \neq 0$ for all elements of the matrix U.

T_1 also varies as $1/\nu$ for low tunneling rates ($\nu << \omega_{th}$), like T_2, but with a prefactor $\frac{\hbar^2\Omega^2}{|u_{\uparrow\downarrow}|^2}$ instead of 2. Table (6.1) indicates that $|u_{\uparrow\downarrow}| << \hbar\Omega$ for the traps studied here, consequently $T_1 > T_2^*$ and $T_2 = T_2^*$ from equation (2.5.29).

6.8 Coherence times in the multi-level model

Figure 6.10 a shows the 10 highest energy levels of the hole qubit. Each line in the figure is formed in reality by two lines which represent two energy levels forming a Kramers doublet split due to the presence of the external static magnetic field **B**. In the 2-level model, the first two $E_1^{\uparrow}$ and $E_1^{\downarrow}$ levels define the qubit as a 2-level system. In the multi-level model, we consider 20 states, which corresponds to $N = 10$, in all our time-dependent simulations.

6.8.1 The case of Trap 1

Figure 6.11 shows the numerical results for T_2, T_1, and $T_1^{'}$ in the Trap 1 configuration. We can see that T_1 follows $T_1^{'}$ which means that T_1 is influenced by the coupling with the other states. For the same reason, T_1 and $T_1^{'}$ are smaller than T_1 obtained in the 2-level model, especially for $\nu > \Omega$ where $T_1^{'}$ continues to decrease until a frequency $\Omega_{12} = (E_1^{\uparrow} - E_2^{\uparrow})/\hbar$. Indeed, the coupling strength between these

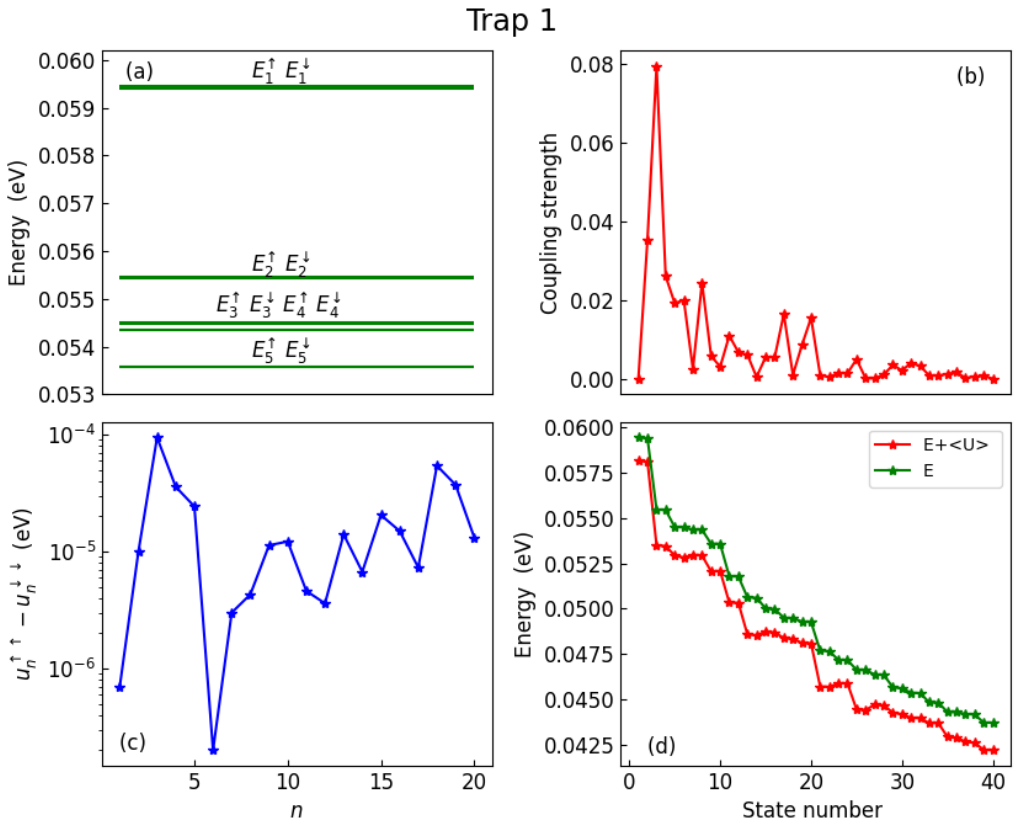

Figure 6.10: (a) The 10 highest electronic energy levels of the hole qubit. (b) Coupling strength defined as the ratio $\left|\langle\varphi_1^{\uparrow}|U|\varphi_n^{\uparrow\downarrow}\rangle\right| / |E_1^{\uparrow} - E_n^{\uparrow\downarrow}|$. (c) $\delta_n = \langle\varphi_n^{\uparrow}|U|\varphi_n^{\uparrow}\rangle - \langle\varphi_n^{\downarrow}|U|\varphi_n^{\downarrow}\rangle = u_n^{\uparrow\uparrow} - u_n^{\downarrow\downarrow}$ versus n. (d) Unperturbed level energies $E_n^{\uparrow\downarrow}$ (green) and perturbed level energies $E_n^{\uparrow\downarrow} + \langle\varphi_n^{\uparrow\downarrow}|U|\varphi_n^{\uparrow\downarrow}\rangle$ (red) presented according to the state number defined as $2n-1$ for $|\varphi_n^{\uparrow}\rangle$ states and $2n$ for $|\varphi_n^{\downarrow}\rangle$ states. (b-d) All results are for Trap 1. (b) and (d) share the same horizontal axis.

two states 1 and 2 is the greatest as shown in figure 6.10 b.

For $\nu << \Omega_{12}$, $T_1^{'}$ varies as $1/\nu$, as in equation (2.5.28), but with a smaller factor compared to that of T_1 of the 2-level model.

The comparison of T_1 or $T_1^{'}$ of the multi-level model with T_1 of the 2-level model shows that the 2-level model is no longer valid to explain the qubit relaxation process.

We can conclude that the relaxation is influenced by the couplings to the higher energy levels which are stronger than the coupling between the two levels, which is clearly seen in figure 6.10 b. The relaxation of the system is globally governed by this effect.

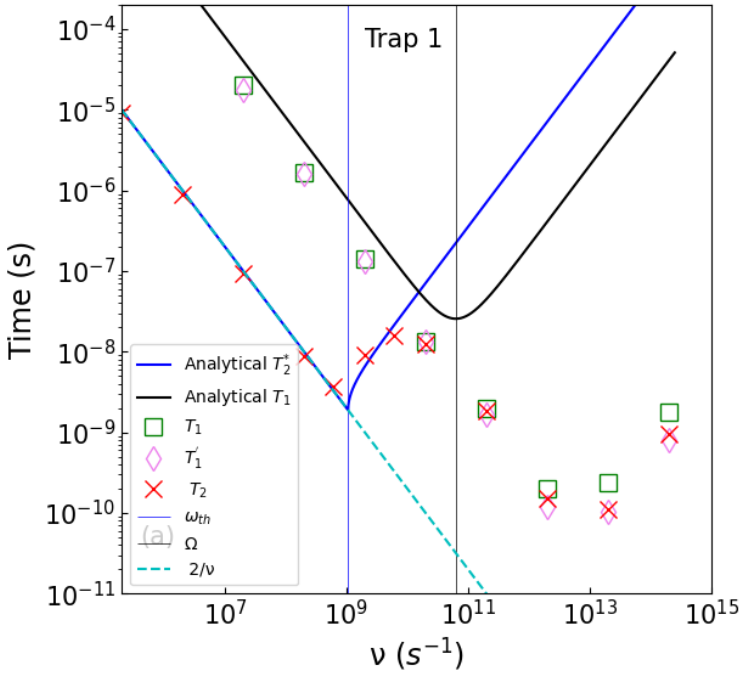

Figure 6.11: Characteristic times T_1 (green square), T_1' (magenta lozanges) and T_2 (red crosses) versus tunneling frequency ν calculated in the multi-level model ($N = 10$) for Trap 1. Solid lines represent the analytical expressions for T_1 (black) and T_2^* (light blue) of the 2-level model, using ω_{th} and $|u_{\uparrow\downarrow}|$ of Table 6.1. The straight dashed turquoise line shows a time varying as $2/\nu$.

T_2 in the multi-level model in the frequency range $\nu < \omega_{th}$ coincides with T_2 of the 2-level model. For $\nu > \omega_{th}$, T_2 approximately follows T_1'. This behavior can be explained by the fact that, in the low frequency range, the dephasing is affected by the fluctuator frequency more than the coupling strength. In the high frequency range, the dephasing will be dominated by T_1, which is already seen in the 2-level model and remains true in the multi-level model.

6.8.2 Results for Trap 2 and 3

Traps 2 and 3 are configurations where the fluctuator is located at a larger distance from the qubit wavefunction than Trap 1. It is clear from Table (6.1) that ω_{th} and $u_{\uparrow\downarrow}$, and the coupling strength [figure (6.14)] decrease as a function of the distance to the qubit wavefunction. This can be seen on T_1 and T_1' of Trap 2 and 3 by the upward shift of the curve relatively to Trap 1, both for the 2-level and multi-level

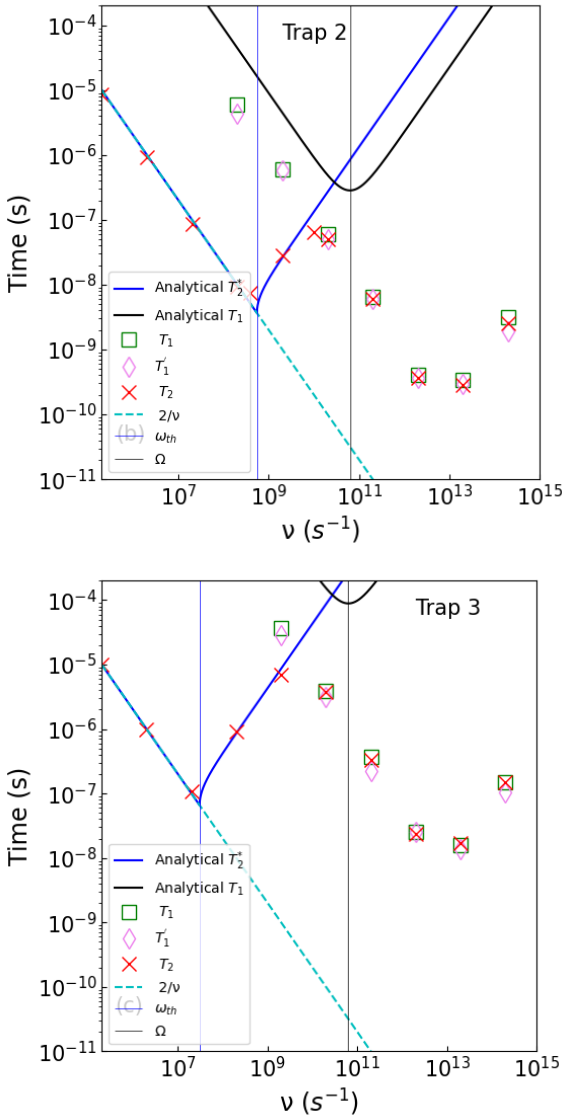

Figure 6.12: Same as figure 6.11 for Trap 2 and Trap 3.

models. By increasing the distance (wavefunction-Trap), the coupling terms all decrease, but those with the higher energy states decrease less rapidly than those within the doublet of states then the shift between the two models increase. Thus the two-level model for T_1 becomes even less valid.

Comparing the T_2 curves of different traps, we notice the shift of ω_{th} to lower frequency. We notice that T_2 for $\nu < \omega_{th}$ always follows the straight line $2/\nu$, no matter the position of the trap. This regime is already seen in the 2-level model discussed in the previous section and in ref [17]. This leads us to the conclusion

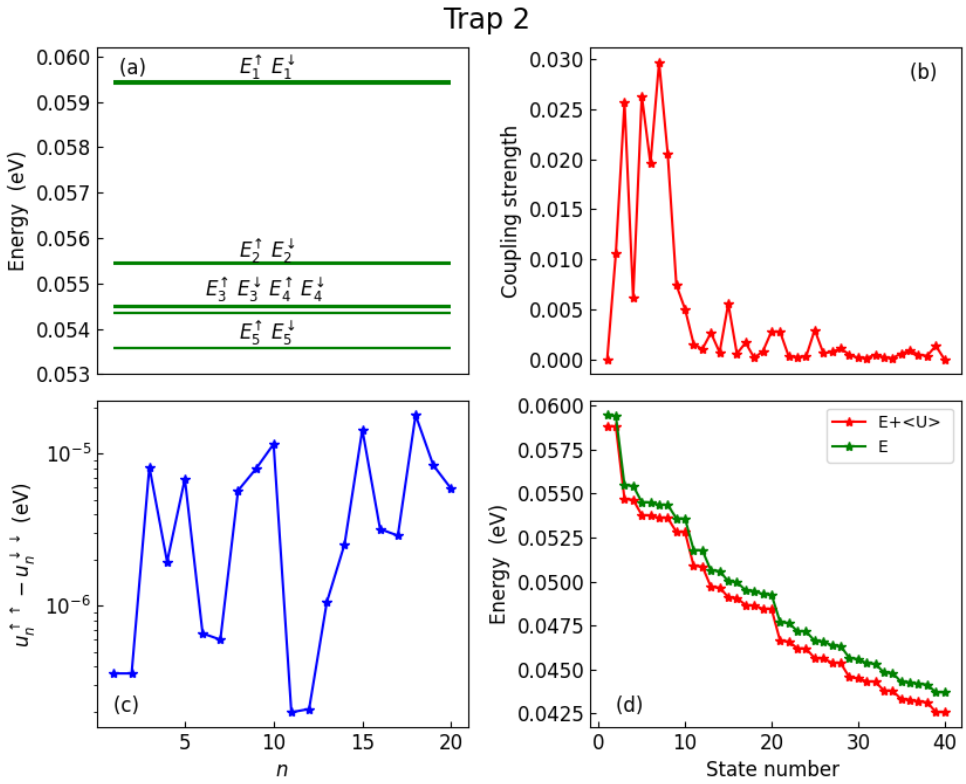

Figure 6.13: Same as figure 6.10 for Trap 2.

that the qubit loses its coherence as a function of time just when the fluctuator undergoes its first switch and remains coherent as long as there is no change of state.

6.9 Effect of non-instantaneous transitions

The telegraphic noise model assumes that the transitions between the two states of the fluctuator are instantaneous. In this section, we consider a situation where the transitions $0 \rightarrow 1$ and $1 \rightarrow 0$ are non-instantaneous.

Figure 6.15 shows the results obtained using a modified telegraphic signal $\chi'(t)$ in which the system is assumed to vary progressively (linearly) between states 0 and 1 over a time $\Delta t = 7$ ps. Figure 6.16 shows that the characteristic times calulated using $\chi'(t)$ behave as a function of frequency ν in the same way as for the original telegraph signal $\chi(t)$. At low frequencies, T_2 remains given by $2/\nu$, the

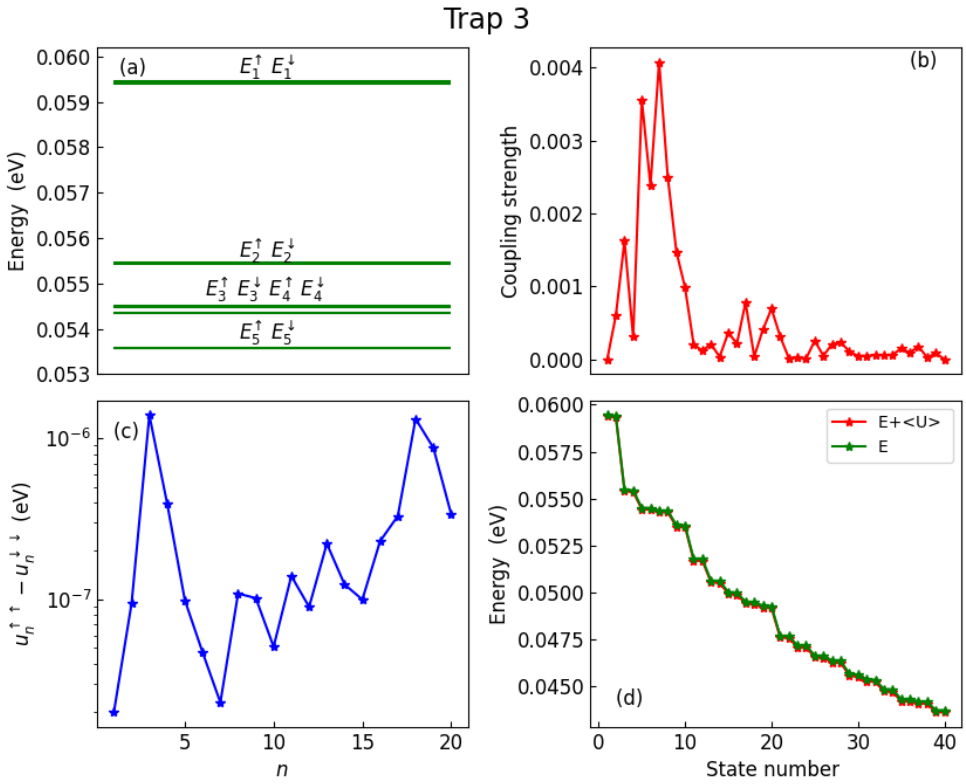

Figure 6.14: Same as figure 6.10 for Trap 3.

dephasing time remains limited by the average switching time of the fluctuator. On the other hand, T_1 and T_1' reach higher values due to the fact that transitions to higher energy hole states are less likely. However, the overall behavior remains the same.

The question is therefore whether a value Δt of 7 ps is realistic. This does not appear to be the case, as tunneling times are typically in the femtosecond range [121, 122], as can be estimated with the expression $\tau_T = d\sqrt{m/(2U_b)}$, in which d is the length of the tunneling barrier ($\approx$ 1 nm), U_b is its height ($\approx$ 2 eV) and m is the carrier effective mass ($\approx$ free electron mass). The characteristic times calculated for Δt in the femtosecond range are those presented in figures. 6.11 and 6.12. Therefore, the instantaneous transitions model employed in this work seems justified.

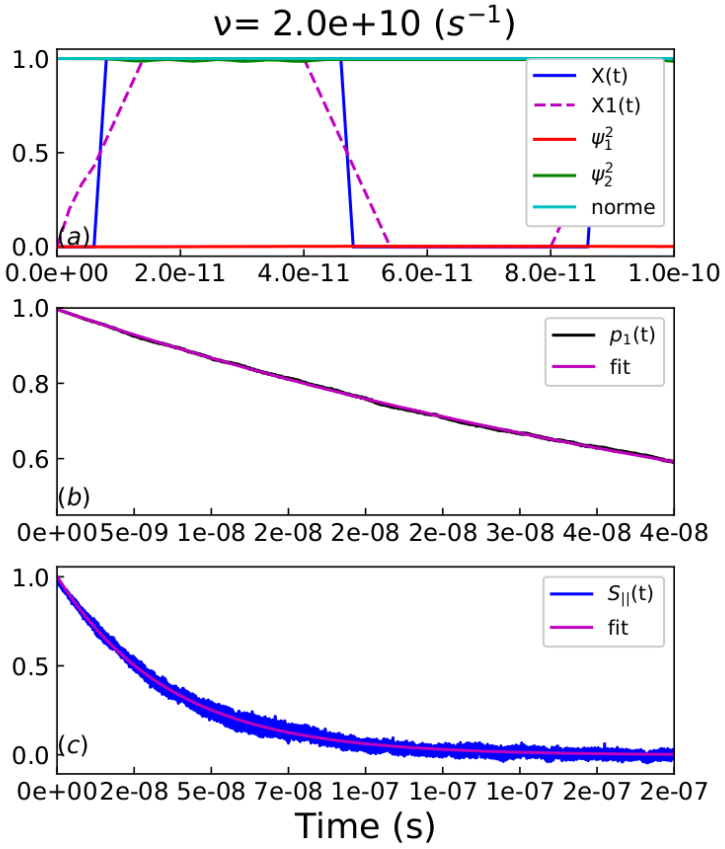

Figure 6.15: (a) Modified telegraphic signal $\chi'(t)$ in which the transition between states 0 and 1 is linear over a time $\Delta t = 7$ ps (magenta dashed line), compared to the original telegraph signal $\chi(t)$ (blue solid line). (b) $p_1(t)$ for Trap 1. (c) $s_{\|}(t)$ which correspond to $\sigma_{\|}(t)$ for Trap 1.

6.10 Dependence on the magnetic field orientation and gate bias

In this part, we will study the influence of the magnetic field orientation and the back gate potential on the coherence time. This study allows us to optimize the effect of the charge fluctuator on the qubit decoherence.

A recent theoretical work on the same kind of hole qubit [110] has discussed the electrical manipulation of the qubit spin by radio frequency. It was found that the Rabi frequency depends on the orientation of the magnetic field and back gate voltage in a complex way, where the symmetry of the wave function in the nanowire plays an important role in understanding this dependence and is controlled by the back gate voltage. In addition, the g-matrix formalism offers a mathematical tool

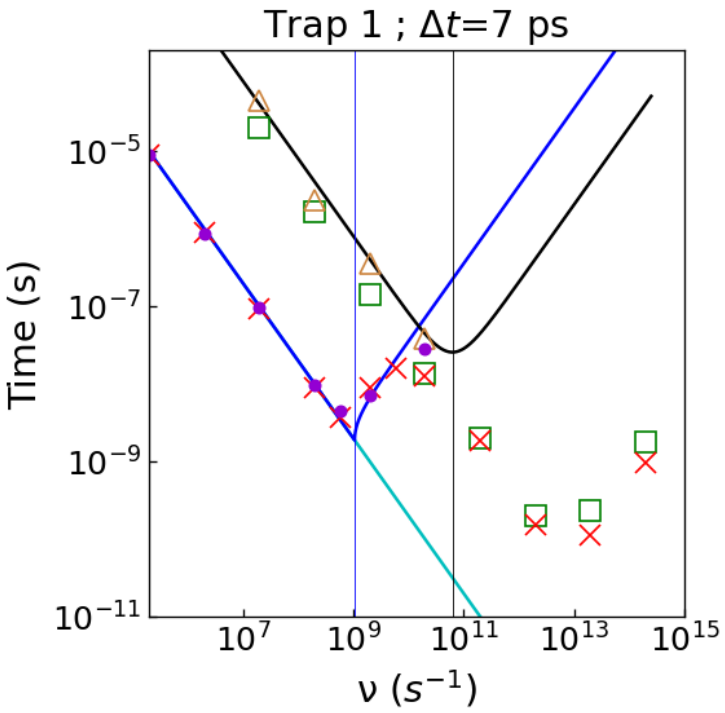

Figure 6.16: Characteristic lifetimes T_1 and T_2 versus switching frequency ν calculated in the multi-level model ($N = 10$) for Trap 1. Green squares: T_1 calculated using $\chi(t)$. Brown triangles: T_1 calculated using $\chi'(t)$. Red crosses: T_2 calculated using $\chi(t)$. Violet dots: T_2 calculated using $\chi'(t)$. Solid lines depict the analytical expressions for T_1 (black) and T_2 (light blue), as given by Eq. (2.5.28) and Eq. (2.5.23), respectively, using ω_{th} and $|u_{\uparrow\downarrow}|$ of Table 6.1. The straight turquoise line shows a time varying as $2/\nu$. Vertical blue line is for $\nu = \omega_{th}$ and vertical black line is for $\nu = \Omega$

to describe the qubit spin response to the magnetic field orientation.

The goal is to increase the coherence time, especially T_2 which is the shortest time among the characteristic times. T_2 depends on the difference $|u_{\uparrow\uparrow} - u_{\downarrow\downarrow}|$ as shown in equations (2.5.23, 2.5.29). T_2 is also defined by the frequency ω_{th} which separates the Gaussian regime from the non-Gaussian regime. ω_{th} is equal to $|u_{\uparrow\uparrow} - u_{\downarrow\downarrow}|/\hbar$ as already discussed in the previous sections. $T_2(\nu = \omega_{th})$ represents the general minimum of $T_2(\nu)$ in the case of a 2-level model and it is a local minimum in the case of a multi-level model. Then it is interesting to study this minimum as a function of the back gate voltage and as a function of the magnetic field orientation.

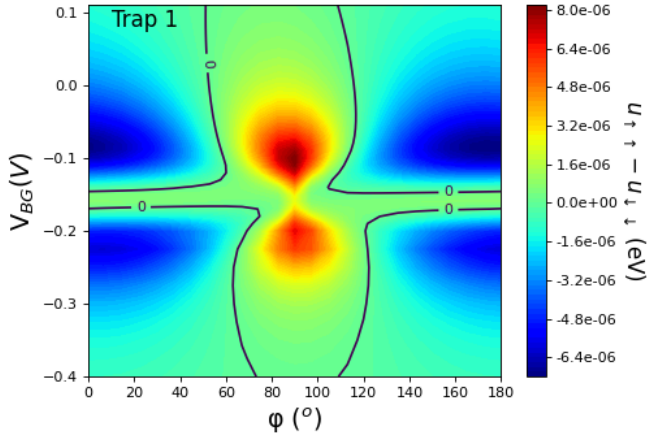

Figure 6.17: 2D plots of $u_{\uparrow\uparrow} - u_{\downarrow\downarrow}$ versus back gate bias V_{BG} and angle φ of B in the xy plane ($\theta = 90°$), for Trap 1. The 2D plots are made on a discrete grid of 25×40 points. The contours indicated by black lines correspond to $u_{\uparrow\uparrow} - u_{\downarrow\downarrow} = 0$.

6.10.1 Discussion of the results

Since $T_2(\nu = \omega_{th}) = 2/\omega_{th}$, it is interesting to study the cases where $|u_{\uparrow\uparrow} - u_{\downarrow\downarrow}| = 0$, where we could expect a divergence of $T_2(\nu = \omega_{th})$. Figure 6.17 shows $|u_{\uparrow\uparrow} - u_{\downarrow\downarrow}| = f(V_{BG}, \varphi)$ as a function of back gate potential and φ for $\theta = \pi/2$, i.e. the magnetic field is always in the xoy plane (figure 4.1). The modulus of the magnetic field is always fixed at $0.29T$. In Figure 6.17, we see positive and negative regions, which define at their boundaries lines where $u_{\uparrow\uparrow} - u_{\downarrow\downarrow} = 0$, that we call sweet lines. Sweet lines are also visible in figure 6.18 which represents a 2D map of $u_{\uparrow\uparrow} - u_{\downarrow\downarrow}$ as a function of θ and φ which define the orientation of the magnetic field, for $V_{BG} = 0$, for the three trap.

Figure 6.19 shows the evolution of T_2 for Trap 1 as a function of ν for a system placed on a sweet line. From this figure, $\omega_{th} = 1.6 \times 10^8$ is found 10 times smaller than ω_{th} of Trap 1 in Table (6.1) but not zero. It was expected that T_2 in this case would tend to infinity due to the fact that $|u_{\uparrow\uparrow} - u_{\downarrow\downarrow}| = 0$ but it is not the case because ω_{th} also depends on the non diagonal elements of the potential matrix U.

In the two-level system, the Hamiltonian in state 1 is

$$H = H_0 + U = \begin{pmatrix} \hbar\Omega/2 + u_{\uparrow\uparrow} & u_{\uparrow\downarrow} \\ u^*_{\uparrow\downarrow} & -\hbar\Omega/2 + u_{\downarrow\downarrow} \end{pmatrix}. \tag{6.10.1}$$

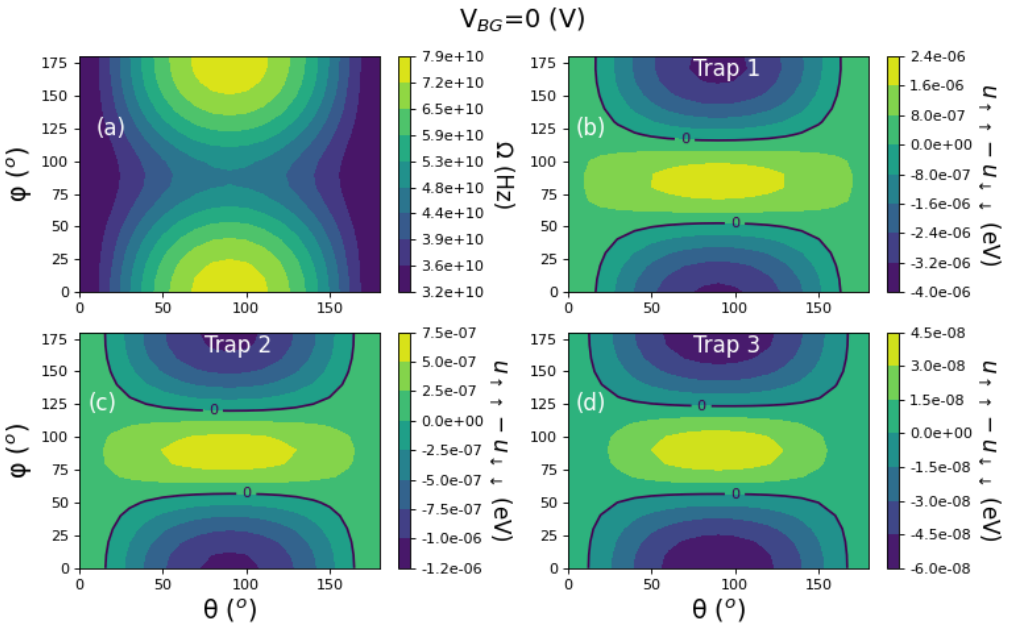

Figure 6.18: 2D plots of the Larmor frequency Ω (a) and $u_{\uparrow\uparrow} - u_{\downarrow\downarrow}$ (b-d) versus θ and φ, for Trap 1 (b), Trap 2 (c) and Trap 3 (d), for $V_{BG} = 0$ V. The contours corresponding to $u_{\uparrow\uparrow} - u_{\downarrow\downarrow} = 0$ are indicated by black lines.

After diagonalization, the Larmor angular frequency Ω' in the state 1 is defined by

$$\hbar\Omega' = 2\sqrt{\left(\frac{\hbar\Omega + u_{\uparrow\uparrow} - u_{\downarrow\downarrow}}{2}\right)^2 + |u_{\uparrow\downarrow}|^2}. \tag{6.10.2}$$

We define the threshold angular frequency

$$\omega_{th} = |\Omega' - \Omega| = \left|\frac{2}{\hbar}\sqrt{\left(\frac{\hbar\Omega + u_{\uparrow\uparrow} - u_{\downarrow\downarrow}}{2}\right)^2 + |u_{\uparrow\downarrow}|^2} - \Omega\right| \tag{6.10.3}$$

which, in the pure dephasing model $|u_{\uparrow\uparrow} - u_{\downarrow\downarrow}| \gg |u_{\uparrow\downarrow}|$, gives equation 2.5.23, i.e. $\omega_{th} \approx |u_{\uparrow\uparrow} - u_{\downarrow\downarrow}|/\hbar$ (because $|u_{\uparrow\uparrow} - u_{\downarrow\downarrow}| \ll \hbar\Omega$).

In the opposite case where $|u_{\uparrow\uparrow} - u_{\downarrow\downarrow}| \ll |u_{\uparrow\downarrow}|$, the threshold angular frequency becomes

$$\omega_{th} \approx \frac{2|u_{\uparrow\downarrow}|^2}{\hbar^2\Omega} \tag{6.10.4}$$

which is valid in particular when one seeks to reach a "sweet" point where $u_{\uparrow\uparrow} -$

$u_{\downarrow\downarrow} \to 0$. Remarquably, ω_{th} in this case can be rewritten as $4/T_1^{min}$ where T_1^{min} is the minimum value of T_1 in the two-level model.

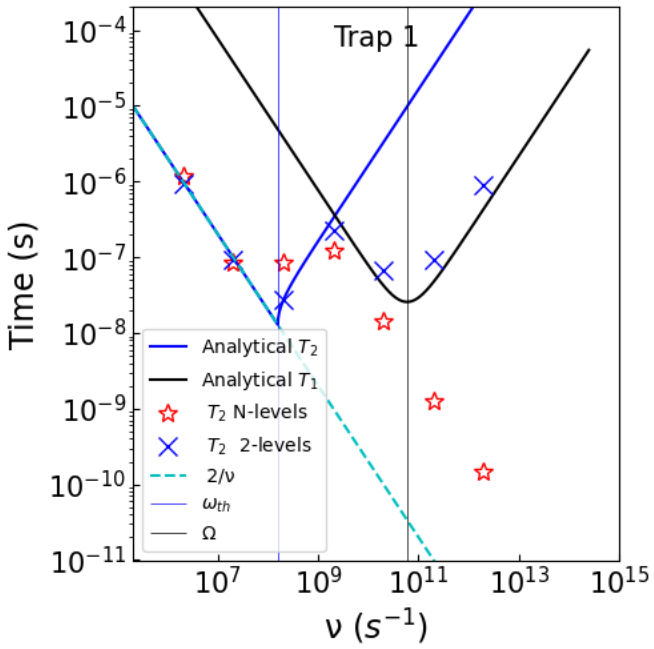

Figure 6.19: Characteristic time T_2 versus tunneling frequency ν calculated in the 2-level model (blue crosses) and multi-level ($N = 10$) model (red stars) for Trap 1, for $V_{BG} = 0$ V, $\varphi = 52.6°$, $\theta = 90°$ and $\hbar\Omega = 3.88 \times 10^{-5}$ eV, in a situation where $u_{\uparrow\uparrow} - u_{\downarrow\downarrow} \approx 0$ eV and $|u_{\uparrow\downarrow}| = 1.41 \times 10^{-6}$ eV. The black solid line show the analytical expression for T_1 of the 2-level model, as given by Eq. (2.5.28). T_2^* (light blue) of the two-level model, as given by Eq. (2.5.23). The straight dashed turquoise line shows a time varying as $2/\nu$.

It is also clear that at low frequency $\nu < \omega_{th}$, T_2 is given by $2/\nu$ and that is independent of the fluctuator potential conditions. This kind of behavior has already been discussed in the previous sections and proved mathematically in the appendix (C.1).

For ν such that T_1 becomes smaller then T_2^* in the 2-level model, T_2 tends to $2T_1$, and in the multi-level model, T_2 is driven by the coupling to high energy levels.

In conclusion, the behavior of T_2 in the case where $u_{\uparrow\uparrow} - u_{\downarrow\downarrow} \approx 0$ (sweet line) is similar to the general case ($u_{\uparrow\uparrow} - u_{\downarrow\downarrow} \neq 0$) but what differs is that ω_{th} is determined by the non-diagonal elements of the potential matrix which are in principle responsible for the relaxation phenomenon. Moreover, it is clear that $T_2(\nu = \omega_{th})$ has become longer on sweet lines, even though it is not infinite.

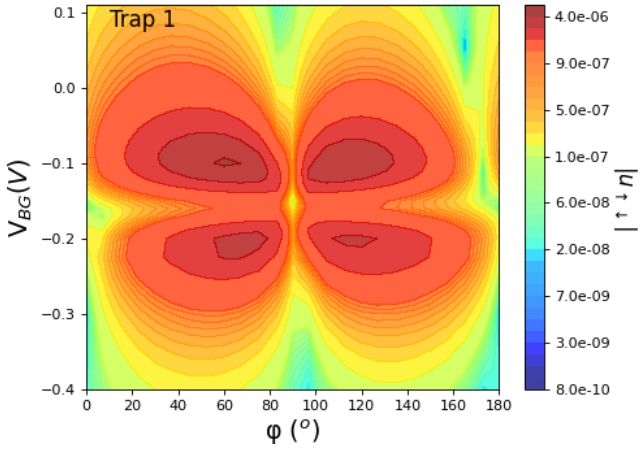

Figure 6.20: 2D plots of $|u_{\uparrow\downarrow}|$ for Trap 1 versus back gate bias V_{BG} and angle φ of B in the xy plane ($\theta = 90°$).

Figure 6.20 shows $u_{\uparrow\downarrow}$ as a function of V_{BG} and φ and then one can find points on the sweet lines where T_2 is larger by reducing $u_{\uparrow\downarrow}$.

Moreover in Figure 6.17 the sweet lines appear almost as horizontal lines at $V_{BG} = -0.15V$, in a situation discussed in the reference [110] where the spin becomes insensitive to the electrical noise applied to the central gate. Moreover in this configuration, the wave function is located in the middle of the nanowire as shown in Figure 6.21.

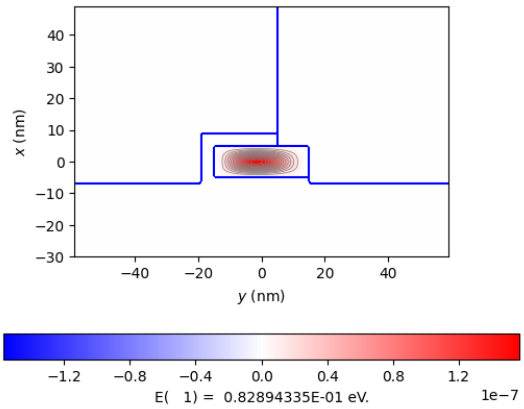

Figure 6.21: Iso-density surface of the ground-state qubit hole wavefunction in the middle of nanowire, obtained when $V_{BG} = -0.15$ V, shown in a transverse section [xy plane at $z = 0$].

We also notice in Figure 6.17 two other quasi vertical lines located at $\varphi = 55°$ and $\varphi = 125°$ where $u_{\uparrow\uparrow} - u_{\downarrow\downarrow} = 0$. These lines appear in a region where the Zeeman splitting is approximately constant as a function of V_{BG} as seen in Figure 6.23. In order to explain that, we take the first-order expansion of the Hamiltonian in $\mathbf{B}$ described in the appendix (B) where it can be rewritten in a general way in the g-matrix formalism as

$$H_0(\mathbf{B}, V_{BG}) = \frac{1}{2}\mu_B \boldsymbol{\sigma} \cdot \hat{g}(V_{BG}) \cdot \mathbf{B} \tag{6.10.5}$$

where $\boldsymbol{\sigma}$ is the vector of Pauli matrices, $\hat{g}(V_{BG})$ is a real 3×3 matrix. Here we highlight the dependence of the Hamiltonian and the g-matrix on the back-gate bias V_{BG}. The dependence on another potential could be considered in the same way. We have assumed that the Hamiltonian is written in the basis $\{|\uparrow\rangle, |\downarrow\rangle\}$ in which the vectors are orthogonal linear combinations of $|\varphi_1^{\uparrow}(0)\rangle$ and $|\varphi_1^{\downarrow}(0)\rangle$. The value of the g factors is not unique, it depends on the choice of the axes and the hole state basis.

As xy is an exact mirror symmetry plane of the device whatever V_{BG}, as yz is an approximate mirror symmetry plane, x, y and z can be considered as the main magnetic axes of the system [110]. For a magnetic field in the xy plane, $\mathbf{B} = B\,(\cos(\varphi), \sin(\varphi), 0)$, the Zeeman Hamiltonian can be written as

$$H_0(\vec{B}, V_{BG}) = \frac{1}{2}\mu_B B \begin{bmatrix} g_x \cos(\varphi) & -i g_y \sin(\varphi) \\ +i g_y \sin(\varphi) & -g_x \cos(\varphi) \end{bmatrix} \tag{6.10.6}$$

in which g_x and g_y depend implicitely on V_{BG}. The Zeeman splitting is equal to

$$\hbar\Omega = \mu_B B \sqrt{g_x^2 \cos^2(\varphi) + g_y^2 \sin^2(\varphi)}. \tag{6.10.7}$$

The g_x and g_y factors calculated for the device studied in this work are shown in Figure 6.22. Very similar g factors were obtained for a nearly identical device and were discussed in Ref. [110]. The evolution of these factors with V_{BG} reflects the respective weight of the wave function on the heavy and light hole states. For

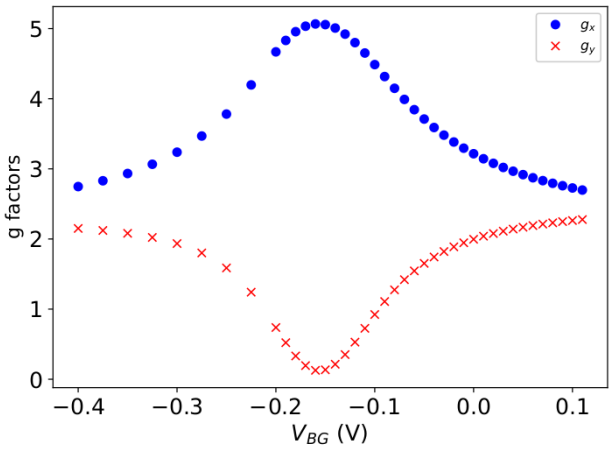

Figure 6.22: g_x and g_y factors for the device considered in the present work.

$V_{BG} \approx -0.15$ V, the wave function is located at the center of the nanowire along y, the heavy hole component is maximal as it is the case in a (100) silicon film. In this case, the in-plane g factors are almost zero, the vertical g factor (g_x) is maximum. For higher or smaller values of V_{BG}, the wave function is pushed to one side of the nanowire. The strong lateral confinement induces a significant increase in the respective weight of the wave function on the light hole states. As shown in Ref. [110], this transfer of the respective weight between heavy and light hole states makes that (Figure 6.22)

$$\frac{\partial g_x}{\partial V_{BG}} \approx -\frac{\partial g_y}{\partial V_{BG}}. \tag{6.10.8}$$

It is interesting to find the conditions for which the Zeeman splitting [Eq. (6.10.7)] is stationary with respect to V_{BG}. Using Eq. (6.10.8), we deduce that $(\partial\,\hbar\Omega)/(\partial\,V_{BG}) = 0$ for

$$g_x \cos^2\varphi = g_y \sin^2\varphi \tag{6.10.9}$$

It is also important to remind that the dependence in V_{BG} of the Zeeman Hamiltonian is essentially through the electric field along the y axis which is the main modulating factor of the g factors. Similar results can be obtained by playing on the potential of the other gates, only the lever arm will be different [18].

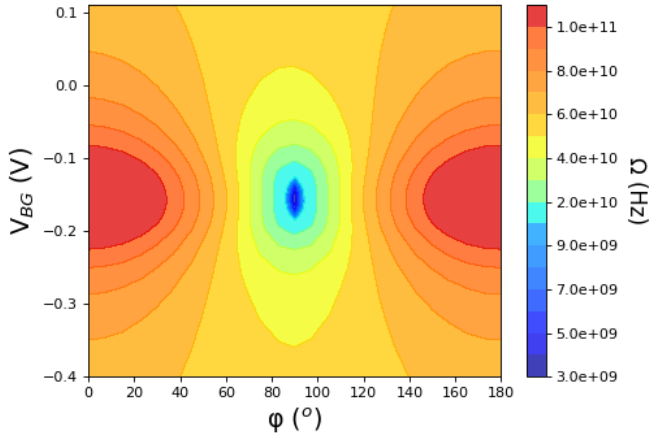

Figure 6.23: 2D plots of (a) the Larmor frequency Ω for Trap 1 versus back gate bias V_{BG} and angle φ of B in the xy plane ($\theta = 90°$).

Figure 6.23 shows the Larmor frequency Ω as a function of V_{BG} and φ. There are vertical regions where Ω varies weakly as a function of V_{BG}. In order to explain this, we look for conditions where the Zeeman splitting given by equation (6.10.7) becomes independent of V_{BG}, when $\delta\Omega/dV_{BG} = 0$. Then we can deduce

$$\varphi \approx \frac{\pi}{2} \pm \arctan\sqrt{\frac{g_x}{g_y}}. \tag{6.10.10}$$

which explains the vertical contours of the figure 6.23 at $\varphi = 90° \pm 34°$ for a ratio $\frac{g_x}{g_y}$ close to 2/3.

One can also derive the elements of the $u_{\uparrow\uparrow} - u_{\downarrow\downarrow}$ of the potential matrix from the g-matrix formalism. The eigenstates of the Hamiltonian given by Eq. (6.10.6) are

$$|\varphi_1^{\uparrow}\rangle = \alpha|\Uparrow\rangle + \beta|\Downarrow\rangle \tag{6.10.11}$$

$$|\varphi_1^{\downarrow}\rangle = -\beta|\Uparrow\rangle + \alpha^*|\Downarrow\rangle \tag{6.10.12}$$

with

$$\alpha = \frac{ib_y g_y}{\sqrt{b_y^2 g_y^2 + \left(b_x g_x + \sqrt{b_x^2 g_x^2 + b_y^2 g_y^2}\right)^2}} \tag{6.10.13}$$

$$\beta = \frac{b_x g_x + \sqrt{b_x^2 g_x^2 + b_y^2 g_y^2}}{\sqrt{b_y^2 g_y^2 + \left(b_x g_x + \sqrt{b_x^2 g_x^2 + b_y^2 g_y^2}\right)^2}} \tag{6.10.14}$$

in which we write $b_x = \cos(\varphi)$ and $b_y = \sin(\varphi)$, for simplicity.

The effect of a fluctuating electric charge results in a perturbation Hamiltonian

$$U = \delta H_0(0, V_{BG}) + \delta H_Z(\mathbf{B}, V_{BG}) \tag{6.10.15}$$

with

$$\delta H_Z = \frac{1}{2}\mu_B B \begin{bmatrix} \delta g_x b_x & -i\delta g_y b_y \\ +i\delta g_y b_y & -\delta g_x b_x \end{bmatrix} + \delta H'_Z \tag{6.10.16}$$

in which, we have $\delta g_x \approx -\delta g_y$. $\delta H'_Z$ contains additional terms like $\delta g_{xy} by$, $\delta g_{yx} bx$ arising from the fact that the variation (differential) of the g matrix may not be diagonal in the same basis and magnetic axes frame as $\hat{g}$ [110]. However, in the present case, these terms are small and the dephasing process is determined by the diagonal matrix elements $u_{\uparrow\uparrow} = \langle\varphi_1^{\uparrow}|\delta H_0 + \delta H_Z|\varphi_1^{\uparrow}\rangle$ and $u_{\downarrow\downarrow} = \langle\varphi_1^{\downarrow}|\delta H_0 + \delta H_Z|\varphi_1^{\downarrow}\rangle$. After some algebra, we obtain:

$$u_{\uparrow\uparrow} = u_0 + \delta u \tag{6.10.17}$$

$$u_{\downarrow\downarrow} = u_0 - \delta u \tag{6.10.18}$$

with $u_0 = \langle\varphi_1^{\uparrow}|\delta H_0|\varphi_1^{\uparrow}\rangle = \langle\varphi_1^{\downarrow}|\delta H_0|\varphi_1^{\downarrow}\rangle$

$$\delta u = -\frac{\delta g_x b_x^3 g_x^2 + \delta g_x b_x^2 g_x \sqrt{b_x^2 g_x^2 + b_y^2 g_y^2} + \delta g_y b_x b_y^2 g_x g_y + \delta g_y b_y^2 g_y \sqrt{b_x^2 g_x^2 + b_y^2 g_y^2}}{b_x^2 g_x^2 + b_x g_x \sqrt{b_x^2 g_x^2 + b_y^2 g_y^2} + b_y^2 g_y^2}. \tag{6.10.19}$$

We can verify that δu and therefore $u_{\uparrow\uparrow} - u_{\downarrow\downarrow}$ cancels for $\delta g_x = -\delta g_y$ and $g_x b_x^2 = g_y b_y^2$ [Eq. (6.10.9)], i.e. when $(\partial\hbar\Omega)/(\partial V_{BG}) = 0$ as shown in figure 6.17 where, we can find the quasi sweet line contours around $\varphi = 90° \pm 34°$ which appear also in figure 6.18.

In Figures 6.23, we do not have straight lines, the analytical calculations provide an approximation and an explanation of the results of the figures which show $u_{\uparrow\uparrow} - u_{\downarrow\downarrow}$ as a function of θ and φ presenting sweet lines aproximately equal to those given in the equation (6.10.10). A large increase in the coherence durations was seen, where the Larmor frequency is least dependent on the gate voltages, demonstrating the presence of these sweet lines, in agreement with the combined experimental and theoretical study of Ref.[18].

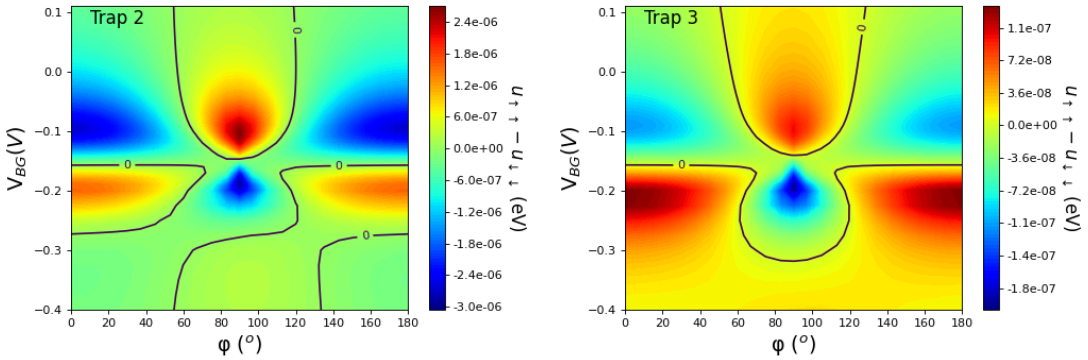

Figure 6.24: Same as the figure 6.17 but for Trap 2and Trap 3

Figure 6.24 shows $u_{\uparrow\uparrow} - u_{\downarrow\downarrow}$ as a function of back gate potential V_{BG} and φ for $\theta = 90°$, for Trap 2 and 3. We clearly see horizontal sweet lines for $V_{BG} \approx -0.15\ V$ which do not vary with the position of the trap. We also found vertical sweet lines around $\varphi = 90° \pm 34°$. In addition the case of Trap 2 exhibits a sweet line for $V_{BG} \approx -0.28\ V$. At this back gate potential the wavefunction is not in the middle of nanowire as for $V_{BG} \approx -0.15\ V$, it is compressed on the right corner of nanowire where it is closer to Trap 2.

Comparing figures 6.17 and 6.24, we can see that for $0.1\ V < V_{BG} < -0.15\ V$ we have almost the same color profile and sweet lines. On the other hand for $-0.15\ V < V_{BG} < -0.4\ V$ the color profile changes when changing the position of trap where we assume that the distance separating the trap's wave function and its position have more influence in this region on the difference $u_{\uparrow\uparrow} - u_{\downarrow\downarrow}$. This is shown by the small distance separating the 2 sweet lines around $V_{BG} = -0.15\ V$ in the case of Trap 1, which widens in the case of Trap 2. This shows the influence of the position of the trap in the device and its distance from the hole wave function. The analytical description of this situation is a more difficult since it is necessary to calculate g_x and g_y taking into account the Trap 2 which has a symmetry breaking effect and makes the g-matrix formalism more complicated to calculate analytically, which has not been done in this thesis.

6.11 Comparison with experimental results

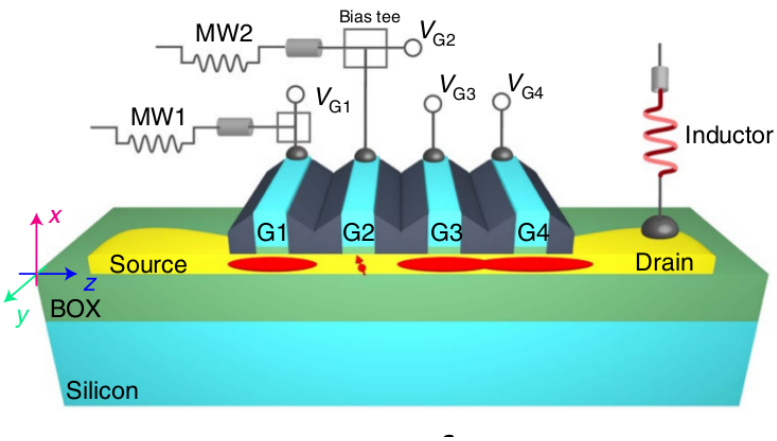

Figure 6.25: Simplified three-dimensional representation of a silicon (yellow)-on-insulator (green) nanowire device with four gates (light blue) labelled G1, G2, G3 and G4. Gate G2 defines a quantum dot (QD2) hosting a single hole; G3 and G4 define a hole island used as reservoir and sensor for hole spin readout; G1 defines a hole island screening QD2 from dopant disorder and fluctuations in the source. Using bias tees, both static voltages (V_{G1}, V_{G2}) and time-dependent, high-frequency voltages (MW1, MW2) can be applied to G1 and G2, respectively. The drain contact is connected to an off-chip, surface-mount inductor to enable radiofrequency reflectometry readout. The coordinate system used for the magnetic field is shown on the left side (in the crystal frame, $x = [001], y = [1\bar{1}0]$ and $z = [110]$). Taken from ref [18].

It is now important to try to compare our simulation results with experimental data. In this section, we focus on reference [18] which concerned a situation very close to the one considered in this thesis. Indeed, the Grenoble researchers studied a four-grid (G1-G4) device (figure above). Grids G3 and G4 define a reservoir of holes that serves as a sensor for reading the hole spin. Grid G2 is used to form the quantum dot, and G1 defines another island of holes to screen the fluctuations coming from the source. Remarkably, the authors of this work are able to confine a single hole under G2, which allows a more direct comparison to theoretical simulations.

This study shows that the effective g factor is strongly anisotropic for the reasons discussed in [109] and in the previous sections. This anisotropy is very well described by the theory presented by the authors of ref [18]. It should be noted that it was necessary for them to introduce small shear deformations within the Si nanowire to improve the agreement with the experiment.

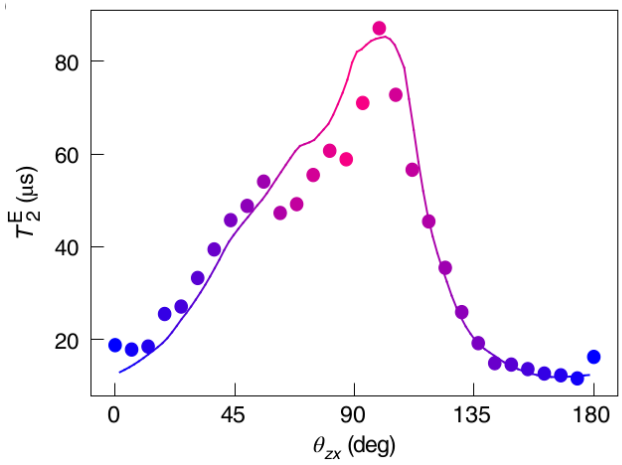

Figure 6.26: Measured T_2^E versus magnetic field angle θ_{zx} (symbols). The solid line is a fit. Taken from ref [18].

The time T_2 was measured by following a Hahn echo protocol [123] which gets rid of low frequency noise sources. The echo amplitude follows a decay law in the form of a stretched exponential as a function of the waiting time τ_{wait} (free evolution), which is interpreted by a high frequency noise ($10^4 - 10^6$ Hz) of characteristic spectrum $S(f) \propto 1/\sqrt{f}$ where f is the frequency. The characteristic time which is deduced, noted T_2^E, depends on the orientation of the magnetic field (measured as function of the angle θ_{zx} in the xz plane) and reaches the remarkable value of 88 μs at its maximum. This dependence is well described from the θ_{zx} dependence of the measured $\partial f_L/\partial V_{G1}$ and $\partial f_L/\partial V_{G2}$ susceptibilities, where f_L is the Larmor frequency and V_{Gi} is the electric voltage on the Gi grid (figure above). This shows that T_2^E is limited by electrical noise generating horizontal and vertical electric fields as those induced by the different gates.

The authors of [18] present other spin coherence measurements following the Carr-Purcell-Meiboom-Gill (CPMG) protocol which consists in applying an increasing number of π pulses which progressively cancels the fastest phase shift effects. Other measures consist in applying Ramsey sequences formed by two $\pi/2$ pulses separated by a variable delay. In contrast to the Hahn echo, the phase shift induced by low frequency noise sources is not cancelled due to the absence of a π refocusing pulse. The phase shift decreases with increasing measurement time t_{meas} due to the

contribution of lower and lower frequency noise components. These experiments highlight the likely influence of noise induced by hyperfine interactions because the device is fabricated in natural silicon including the ^{29}Si isotope with non-zero nuclear spin. The power spectrum of this noise at low frequency ($10^{-4} - 10^{-2}$ Hz) behaves like $1/f$.

Although experiments show that the high frequency noise has an electrical origin, its precise physical origin remains unknown. We can assume that it comes from a number of fluctuators like those studied in this thesis. Let us first assume that a very small number of fluctuators contribute to most of the noise. Each fluctuator n can be characterized by its threshold angular frequency ω_{th}^n and by its oscillation frequency ν_n. If $\nu_n < \omega_{th}^n$, each fluctuator is in the non-Gaussian regime. It is then easy to show that T_2^* is given by $2/\sum_n \nu_n$ (Appendix C). In the probable case where one of the fluctuators is much faster than the others (of frequency ν_{max}), T_2^* is given by $2/\nu_{max}$, i.e. the coherence is bounded by the fastest of the fluctuators, by the moment when it first changes state. In this regime, T_2^* does not depend on the magnetic field orientation and is not related to the noise spectrum $S(\omega)$ for $\omega \to 0$. We can therefore deduce that the experimental system of [18] does not work in a configuration dominated by a small number of fluctuators in the non-Gaussian regime.

The most likely situation is that the fluctuators involved in the measured noise are characterized by $\nu_n > \omega_{th}^n$, i.e. they operate in the Gaussian regime. As the measured time T_2^E is relatively long, this means that the threshold angular frequencies ω_{th}^n are low, smaller than $\approx 10^4$ Hz. Since $\omega_{th} = |u^{\uparrow\uparrow} - u^{\downarrow\downarrow}|/\hbar$, we conclude that the fluctuators involved are characterized by weak coupling terms (U matrix), which corresponds to defects very far from the qubit, or characterized by a weak charge displacement ($U \propto d$ where d is the dipole), or whose dipole potential is strongly screened, for example by a gas of holes. T_2^* is then determined by the noise spectrum induced by the totality of the "far" fluctuators. This situation seems reasonable (but not guaranteed), since the component studied experimentally in [18] has been chosen among the best of the manufactured batch. The devices are sorted by an automatic prober which measures their $I(V)$ characteris-

tics at room temperature. Those selected for low temperature measurements are those with the best performances, e.g., uniformity of threshold voltages between the different gates, value and uniformity of sub-threshold slopes, absence of gate leakage currents...

It could be interesting in the future to characterize noisier devices in order to see if non-Gaussian behaviors induced by a small number of "closer" telegraphic fluctuators can be highlighted. One could also imagine very low noise situations where the influence of the distant environment is reduced but remains governed by a few extremely slow fluctuators for which $\nu_n < \omega_{th}^n$. In these cases, the coherence time would become independent of the magnetic field orientation.

6.12 Conclusion; outlook

The results obtained in this chapter show the impact of the distance separating the fluctuator from the hole wave functions on the coherence time. Furthermore the comparison of the 2-level model with the multi-level model shows that the 2-level model is not sufficient to describe all the existing effects that cause the decoherence and that the coupling of the fundamental doublet with the other energy states has a non negligible effect on the hole qubit relaxation. It was also found that, in the low frequency range, the dephasing time is described by $2/\nu$ which is a physical limit attached only to the fluctuator frequency. It was also possible to find so-called sweet lines on which the effect of the fluctuator on the dephasing is reduced but not cancelled due to the influence of non-diagonal coupling matrix elements.

Chapter 7

Bloch-Redfield

7.1 Intoduction

In this chapter, we discuss the Bloch Redfield theory as an approach to calculate the characteristic relaxation and dephasing times T_1 and T_2 respectively for a two-state system. We describe the theory and the general equations. We introduce two models with which we deduce the coherence characteristic times. Then we discuss the results obtained with the two approaches compared to the results obtained in chapter 6.

7.2 Description of the theory

A method for obtaining a master equation describing the dynamics of a microscopic system in interaction with its environment is the Bloch-Redfield formalism. Under the notion of weak system-environment coupling, it begins from a combined system-environment perspective and develops a perturbative master equation for the system alone. On the positive side, this method has the benefit of immediately obtaining the dissipation processes and rates from environmental characteristics such as correlation functions. On the negative side, it does not automatically ensure that the resultant master equation unconditionally maintains the density matrix's physical characteristics (because it is a perturbative method). Therefore,

caution should be paid while using the Bloch-Redfield master equation, and the derivation's underlying assumptions must be respected. See, for instance, [124] or [125], for a complete derivation of the Bloch Redfield master equation. Below we provide a simplified description of the derivation.

We recall the Liouville-von Neumann equation which describes the evolution of the density matrix ρ as a function of time.

$$i\hbar\frac{\partial}{\partial t}\rho(t) = [H, \rho(t)] \tag{7.2.1}$$

We consider that a system Hamiltonian H_S is weakly coupled to an environment of bath Hamiltonian H_B. The coupling Hamiltonian V is considered separable as shown in equation (7.2.2) where S_n plays on the Hilbert space of the system and B_n plays on the Hilbert space of the bath.

$$H(t) = H_0 + V(t), \qquad H_0 = H_S + H_B, \qquad V = \sum_n S_n \otimes B_n \tag{7.2.2}$$

$$\rho_I(t) = e^{iH_0t/\hbar}\rho(t)e^{-iH_0t/\hbar} \qquad V_I(t) = e^{iH_0t/\hbar}V(t)e^{-iH_0t/\hbar} \tag{7.2.3}$$

The density matrix $\rho_I(t)$ and the coupling Hamiltonian $V_I(t)$ in the interaction picture are introduced by the transformations that appear in equation (7.2.3). The development of the equation (7.2.1) in the interaction picture reads as

$$i\hbar\frac{\partial}{\partial t}\rho_I(t) = [V_I(t), \rho_I(t)] \tag{7.2.4}$$

where H_0 disappears in this representation. Formal integration gives

$$\rho_I(t) = \rho_I(0) - \frac{i}{\hbar}\int_0^t [V_I(\tau), \rho_I(\tau)]d\tau \tag{7.2.5}$$

wich leads to

$$\frac{\partial}{\partial t}\rho_I(t) = -\frac{i}{\hbar}[V_I(t), \rho_I(0)] - \frac{1}{\hbar^2}\int_0^t d\tau[V_I(t), [V_I(\tau), \rho_I(\tau)]] \tag{7.2.6}$$

As discussed by Breuer and Petruccine [125], all observations of interest refer to the system S and are therefore of the form $A \otimes I_B$ where A acts on Hilbert space of the system and I_B is the identity operator in the Hilbert space of the bath. Expectation values given by

$$\langle A\rangle(t) = Tr\{\rho(t)A\} \tag{7.2.7}$$

can be written as

$$\langle A\rangle(t) = Tr_s\{\rho_S(t)A\} \tag{7.2.8}$$

with $\rho_S(t) = Tr_B\{\rho(t)\}$ is the reduced density operator obtained by taking the trace over the degrees of freedom of the environment. Here we use the Born approximation which assumes that the influence of the system on the reservoir is small (weak coupling) and therefore

$$\rho(t) \approx \rho_s(t) \otimes \rho_B \tag{7.2.9}$$

where ρ_B is equilibrium density operator in the bath. This assumes that the bath returns instantaneously to equilibrium, i.e on a time scale much shorter than the evaluation of $\rho_s(t)$. Taking the trace over the bath of equation 7.2.6 gives

$$\frac{\partial}{\partial t}(\rho_{SI}(t)) = -\frac{1}{\hbar^2}\int_0^t d\tau Tr_B[V_I(t),[V_I(\tau),\rho_{SI}(\tau)\otimes\rho_B]] \tag{7.2.10}$$

because it can be shown that $Tr_B[V_I(t),\rho_I(0)] = 0$ (ρ_{SI} is ρ_S in the interaction picture) [125]. Equation (7.2.10) is non-Markovian since the density at time t depends on the history through $\rho_{SI}(\tau)$. Once again, if the time scales of the correlations in the environment are small compared to the time scales of the system dynamics, the neglect of memory effects is justified. This is done by replacing $\rho_{SI}(\tau)$ by $\rho_{SI}(t)$ is equation (7.2.10):

$$\frac{\partial}{\partial t}(\rho_{SI}(t)) = -\frac{1}{\hbar^2}\int_0^t d\tau Tr_B[V_I(t),[V_I(\tau),\rho_{SI}(t)\otimes\rho_B]] \tag{7.2.11}$$

which depends on the initial state $\rho_{SI}(0)$ and therefore remains non-Markovian. A Markovian quantum master equation is obtained by substituting τ by $t-\tau$ and by extending the integration to ∞ [125] :

$$\frac{\partial}{\partial t}(\rho_{SI}(t)) = -\frac{1}{\hbar^2}\int_0^\infty d\tau Tr_B[V_I(t),[V_I(t-\tau),\rho_{SI}(t)\otimes\rho_B]] \tag{7.2.12}$$

which is of second order in V_I (weak coupling to the bath).

The next step is to write the system-bath coupling in the form

$$V_I = \sum_n S_n \otimes B_n \tag{7.2.13}$$

where S_n and B_n are system and bath operators, respectively. This allows to rewrite the equation in terms of correlation functions $\langle B_n(\tau)B_m(0)\rangle = Tr_B\{B_n(\tau)B_m(0)\rho_B\}$ using the fact that the bath is considered in a stationary state on the coarse-grain time scale on which we describe the system evolution.

7.3 General equations for classical noise

7.3.1 General case of a N-level system

A usual situation is to work is the basis of the eigenstates (of energies E_α) of the time-independent H_S. In a semi-classical approach, the interaction with the bath is just described by the matrix of $V(t)$ in this basis. Following Redfield [94], equation (7.2.12) becomes in the Schrödinger picture

$$\frac{\partial}{\partial t}\rho_s^{\alpha\beta}(t) = -i\omega_{\alpha\beta}\rho_s^{\alpha\beta}(t) + \sum_{\delta\gamma} R_{\alpha\beta\delta\gamma}\rho_s^{\delta\gamma}(t) \tag{7.3.1}$$

with $\rho_s^{\alpha\beta}$ is a matrix element of ρ_s and

$$\begin{aligned}\hbar^2 R_{\alpha\beta\delta\gamma} &= g_{\alpha\delta\gamma\beta}(\omega_{\delta\alpha}) + g_{\alpha\delta\gamma\beta}(\omega_{\beta\gamma}) \\ &\quad - \sum_v g_{\alpha vv\delta}(\omega_{\delta v})\delta_{\gamma\beta} - \sum_v g_{\gamma vv\beta}(\omega_{v\gamma})\delta_{\delta\alpha}\end{aligned} \tag{7.3.2}$$

with $\omega_{\alpha\beta} = (E_\alpha - E_\beta)/\hbar$ and

$$g_{\alpha\beta\delta\gamma}(\omega) = \frac{1}{2}\int_{-\infty}^{\infty} d\tau e^{i\omega\tau}\langle V_{\alpha\beta}(\tau)V_{\delta\gamma}(0)\rangle \tag{7.3.3}$$

In equation 7.3.1, R is the Redfield tensor derived in reference [94]. g represents the noise-power spectra of the environment. R describes the relaxation of the system due to the perturbation of the environment. The element $R_{\alpha\alpha\delta\delta}$ is the transition rate from state δ to α.

We recall that the Bloch-Redfield equation is justified when the dynamics and relaxation of the system take place over a long time compared to the correlation times of the environment. This means that the following conditions must be verified : $|R^{-1}_{\alpha\beta\delta\gamma}| >> \tau_c$ with $\langle V_{\alpha\beta}(t)V_{\delta\gamma}(0)\rangle \approx e^{-\tau/\tau_c}$ at long time.

7.3.2 General case of a 2-level system

We return to the particular case of the two-level system subjected to telegraph noise. H_S and V are represented in the basis $\{\uparrow,\downarrow\}$ that we denote $\{0,1\}$ for convenience. ρ_S is the density matrix of the system with $\rho_S^{00}+\rho_S^{11}=1$, $\rho_S^{01}=\rho_S^{10*}$ and

$$H_S=\hbar\begin{pmatrix}\Omega/2 & 0\\ 0 & -\Omega/2\end{pmatrix},\quad V(t)=B(t)U,\quad U=\begin{pmatrix}u_{00} & u_{01}\\ u_{10} & u_{11}\end{pmatrix},\quad \rho_S=\begin{pmatrix}\rho_S^{00} & \rho_S^{01}\\ \rho_S^{10} & \rho_S^{11}\end{pmatrix} \tag{7.3.4}$$

where $B(t)$ was defined in eq (2.5.4) as $\chi(t)-\langle\chi(t)\rangle$. The correlation functions are given by

$$g_{\alpha\beta\delta\gamma}(\omega)=\frac{\Delta U_{\alpha\beta}U_{\delta\gamma}}{\nu^2+\omega^2} \tag{7.3.5}$$

where $\Delta=q_0q_1$, equal to $1/4$ when $q_0=q_1=1/2$.

The element of R and g are given in the appendix (E). This allows to write the R matrix as

$$R=\begin{pmatrix}R_{0000} & R_{0001} & R_{0001}^* & -R_{0000}\\ R_{0100} & R_{0101} & R_{0110} & -R_{0100}\\ R_{0100}^* & R_{0110}^* & R_{0101}^* & -R_{0100}^*\\ -R_{0000} & -R_{0001} & -R_{0001}^* & R_{0000}\end{pmatrix} \tag{7.3.6}$$

The differential equation system

The Bloch-Redfield equations give us a system of coupled differential equations for the density matrix elements which reads as

$$\frac{\partial}{\partial t}\begin{pmatrix}\rho_S^{00}(t)\\ \rho_S^{01}(t)\\ \rho_S^{10}(t)\\ \rho_S^{11}(t)\end{pmatrix}=\left[\begin{pmatrix}0 & 0 & 0 & 0\\ 0 & -i\Omega & 0 & 0\\ 0 & 0 & i\Omega & 0\\ 0 & 0 & 0 & 0\end{pmatrix}+R\right]\begin{pmatrix}\rho_S^{00}(t)\\ \rho_S^{01}(t)\\ \rho_S^{10}(t)\\ \rho_S^{11}(t)\end{pmatrix} \tag{7.3.7}$$

We can reduce these four equations into three in which $\langle\sigma_z\rangle(t)=tr[\rho_S(t)\sigma_z]=$

$\rho_S^{00}(t) - \rho_S^{11}(t)$:

$$\frac{\partial}{\partial t}\begin{pmatrix} \langle\sigma_z\rangle(t) \\ \langle Re(\rho_S^{01})\rangle(t) \\ \langle Im(\rho_S^{01})\rangle(t) \end{pmatrix} = Y \begin{pmatrix} \langle\sigma_z\rangle(t) \\ \langle Re(\rho_S^{01})\rangle(t) \\ \langle Im(\rho_S^{01})\rangle(t) \end{pmatrix} \tag{7.3.8}$$

with the tensor Y given by

$$Y = \begin{pmatrix} 2R_{0000} & 4Re(R_{0001}) & -4Im(R_{0001}) \\ Re(R_{0100}) & Re(R_{0101}) + Re(R_{0110}) & -Im(R_{0101}) + \Omega + Im(R_{0110}) \\ Im(R_{0100}) & Im(R_{0101}) - \Omega + Im(R_{0110}) & Re(R_{0101}) - Re(R_{0110}) \end{pmatrix} \tag{7.3.9}$$

This system of differential equations can be solved numerically, the solutions have this form

$$\begin{pmatrix} \langle\sigma_z\rangle(t) \\ \langle Re(\rho_S^{01})\rangle(t) \\ \langle Im(\rho_S^{01})\rangle(t) \end{pmatrix} = K_1 e^{\lambda_1 t}\begin{pmatrix} a_1 \\ b_1 \\ c_1 \end{pmatrix} + K_2 e^{\lambda_2 t}\begin{pmatrix} a_2 \\ b_2 \\ c_2 \end{pmatrix} + K_3 e^{\lambda_3 t}\begin{pmatrix} a_3 \\ b_3 \\ c_3 \end{pmatrix} \tag{7.3.10}$$

we obtain 3 characteristic times $T_1 = \frac{-1}{Re(\lambda_1)}$, $T_2 = \frac{-1}{Re(\lambda_2)}$ and $T_3 = \frac{-1}{Re(\lambda_3)}$. Numerical calculations show that $\lambda_2 = \lambda_3^*$ and therefore $T_2 = T_3$.

7.3.3 Particular case of Rotating Wave Approximation

We describe the Rotating Wave Approximation (RWA) allowing to decouple the differential equations. The density matrix can be expressed in the rotating frame as

$$\rho_{SI}(t) = e^{iH_0 t/\hbar}\rho_S e^{-iH_0 t/\hbar} \tag{7.3.11}$$

which gives

$$\rho_{SI}^{00}(t) = \rho_S^{00}(t) \qquad \rho_{SI}^{11}(t) = \rho_S^{11}(t) \tag{7.3.12}$$

$$\rho_{SI}^{01}(t) = \rho_S^{01}(t)e^{i\Omega t} \qquad \rho_{SI}^{10}(t) = \rho_S^{10}(t)e^{-i\Omega t} \tag{7.3.13}$$

Then we can write the differential equation of $\rho_{SI}^{00}(t)$ and $\rho_{SI}^{01}(t)$ in the rotating frame as

$$\frac{d}{dt}\rho_{SI}^{00}(t) = R_{0000}(\rho_{SI}^{00} - \rho_{SI}^{11}) + R_{0001}\rho_{SI}^{01}e^{-i\Omega t} + R_{0001}^*\rho_{SI}^{10}e^{i\Omega t} \tag{7.3.14}$$

$$\frac{d}{dt}\rho_{SI}^{01}(t) = R_{0100}(\rho_{SI}^{00} - \rho_{SI}^{11})e^{i\Omega t} + R_{0101}\rho_{SI}^{01} + R_{0110}^{*}\rho_{SI}^{10}e^{2i\Omega t} \tag{7.3.15}$$

If we neglect the fast counter rotating terms, we have equations where $\rho_{SI}^{00}(t)$ and $\rho_{SI}^{01}(t)$ are decoupled. Then we return to the main frame and the differential equations read as

$$\frac{d}{dt}\rho_{S}^{00}(t) = R_{0000}(\rho_{S}^{00} - \rho_{S}^{11}) \tag{7.3.16}$$

$$\frac{d}{dt}\rho_{S}^{11}(t) = -\frac{d}{dt}\rho_{S}^{00}(t) \tag{7.3.17}$$

$\sigma_z(t)$ is calculated as in the general case

$$\langle\sigma_z\rangle(t) = Tr[\rho_S(t)\sigma_z] = \rho_S^{00}(t) - \rho_S^{11}(t) \tag{7.3.18}$$

The solution of this differential equation gives us the relaxation time T_1

$$\frac{d}{dt}\langle\sigma_z\rangle(t) = 2R_{0000}\langle\sigma_z\rangle(t) \qquad \langle\sigma_z\rangle(t) = \sigma_z(0)e^{-t/T_1} \tag{7.3.19}$$

Using elements R_{0000} given in Appendix E, we obtain

$$T_1^{-1} = \frac{2}{\hbar^2}[-g_{0110}(\Omega) - g_{0110}(-\Omega)] = \frac{2}{\hbar^2}\frac{2\nu\Delta U_{01}U_{10}}{\nu^2 + \Omega^2} \tag{7.3.20}$$

which agrees with equation (2.5.28) sinse $U_{01} = u^{\uparrow\downarrow}$ (chapter 2).

Neglecting the counter rotating terms in equation (7.3.15) leads to :

$$\frac{d}{dt}\rho_{SI}^{01}(t) = R_{0101}\rho_{SI}^{01} \tag{7.3.21}$$

$$\rho_{SI}^{01}(t) = \rho_{SI}(0)e^{R_{0101}t} \tag{7.3.22}$$

$$\rho_{S}^{01}(t) = \rho_{S}(0)e^{-i\Omega t}e^{R_{0101}t} \tag{7.3.23}$$

which gives

$$\rho_{S}^{01}(t) = \rho_{S}(0)e^{-i\Omega' t}e^{-t/T_2} \tag{7.3.24}$$

in which T_2 is the dephasing time with

$$T_2^{-1} = Re(-R_{0101}) = -\frac{\Delta(2U_{00}U_{11} - U_{00}^2 - U_{11}^2)}{\hbar^2\nu} + \frac{2\nu\Delta U_{01}U_{10}}{\hbar^2(\nu^2 + \Omega^2)} \tag{7.3.25}$$

We deduce :

$$T_2^{-1} = T_2^{*-1} + (2T_1)^{-1} \tag{7.3.26}$$

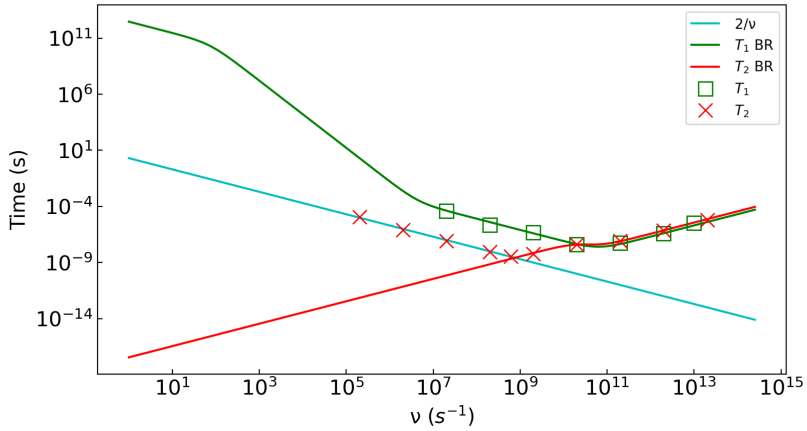

Figure 7.1: Characteristic times T_1 (green) and T_2 (red) obtained with the Bloch-Redfield equations (solid lines) and with the time-dependent simulations (squares and crosses, respectively). The blue line represents a time varying as $2/\nu$.

$$T_2^{*-1} = -\frac{\Delta(2U_{00}U_{11} - U_{00}^2 - U_{11}^2)}{\hbar^2\nu} = \frac{\Delta(U_{00} - U_{11})^2}{\hbar^2\nu} \tag{7.3.27}$$

in which T_2^* is the pure dephasing lifetime. Interestingly, the RWA implies that the terms R_{0100} and R_{0001} have a negligible effect, as when the diagonal and non-diagonal terms are uncorrelated, such as $\langle V_{00}(\tau)V_{01}(0)\rangle = 0$.

7.4 Comparison between Bloch-Redfield and time-dependent simulations

In this section, we present the results obtained from the numerical solution of equation (7.3.8) deduced from the Bloch-Redfield equation for Trap 1, in the two-level model. We compare to the results obtained by solving the time-dependent Schrödinger equation presented and discussed in the previous chapters. This comparison highlights the limitations of the Bloch-Redfield approach.

We recall that the angular frequency ω_{th} delimits two regimes of behavior ($\omega_{th} = 1.96 \times 10^9$ s^{-1} for Trap 1). For $\nu > \omega_{th}$, the agreement between Bloch-Redfield and time-dependent simulations is excellent. On the other hand, for $\nu < \omega_{th}$, Bloch-Redfield gives a time T_2 proportional to ν whereas it should vary as $2/\nu$

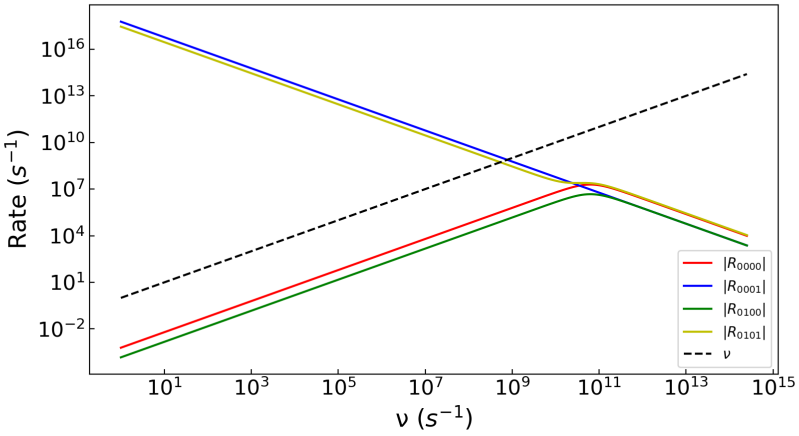

Figure 7.2: Absolute value of the elements of the R tensor versus frequency ν. The black dashed line represents the limit of a transition rate equal to ν. Matrix elements of R larger in absolute value than ν mean that the Bloch-Redfield theory is no longer in its domain of validity.

as predicted by the exact analytical calculation [Eq. (2.5.23)]. In this frequency range, the Gaussian model is no longer valid, the dephasing time is fixed by the average time when the fluctuator changes state for the first time. This non-Gaussian behavior can obviously not be described by the Bloch-Redfield theory in which the environment is described by the correlation functions of its fluctuations whereas here a single change of state of the fluctuator determines the decoherence of the system.

The relaxation time T_1 seems to be very well described by the Bloch-Redfield theory but this conclusion must be immediately qualified. Indeed, we are not able to perform time-dependent simulations for frequencies lower than 10^7 s^{-1} which would require to consider simulation times longer than one millisecond. Moving to lower frequencies, Figure 7.1 shows that Bloch-Redfield predicts a change in the behavior of T_1 which starts to grow faster than $1/\nu$. We are not able to perform time-dependent simulations in this frequency range. We will return to this point later in the chapter.

To better understand the limitations of the Bloch-Redfield model, we plot the matrix elements of the R tensor as a function of ν in Figure 7.2. The black dashed line represents $1/\tau_c = \nu$ where τ_c is the correlation time of the fluctuator

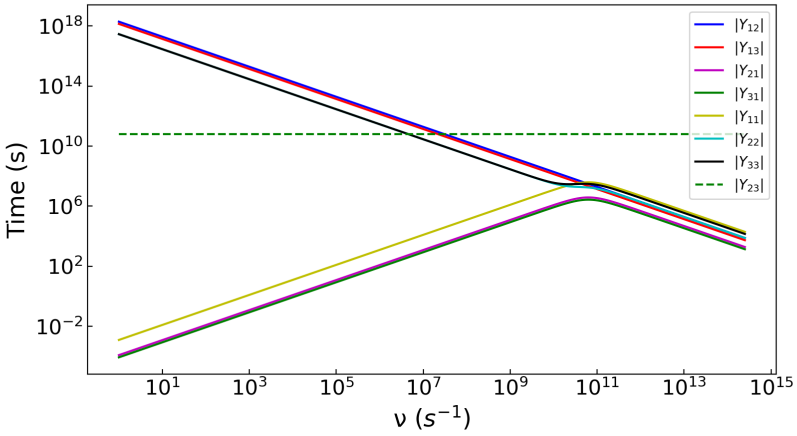

Figure 7.3: Absolute value of the elements of the matrix Y. Note that $|Y_{23}| = \Omega$.

as discussed in the previous section. We see that, for $\nu \lesssim 5 \times 10^8$ s^{-1}, $|R_{0001}|$ and $|R_{0101}|$ become larger than ν, meaning that $|R_{0001}| \gg 1/\tau_c$ and $|R_{0101}| \gg 1/\tau_c$. In this case, the Bloch-Redfield theory is no longer justified because some elements of the two-level system dynamics become faster than the correlation times of the environment, which is in opposition to the assumptions that established the Bloch-Redfield equation. For $\nu \gtrsim 5 \times 10^8$ s^{-1}, all conditions are verified and the Bloch-Redfield theory explains well the behavior of T_1 and T_2 (Figure 7.1).

7.5 T_1 using perturbation method

The behavior of T_1 predicted by the numerical solution of the Bloch-Redfield equation (Figure 7.1), through the diagonalization of the Y matrix of the Equation (7.3.8), shows a surprising behavior, with a considerable increase at low frequencies, which corresponds to an eigenvalue λ_1 of equation (7.3.10) rapidly tending towards 0. It is therefore important to check that this is not an artifact of the numerical calculation. We show here that this is not the case by demonstrating that the same value of T_1 can be obtained analytically by a perturbation approach.

The 3×3 system of differential equations (7.3.8) involves the real matrix Y. The plot of the matrix elements versus ν shows that Y can be rewritten as $Y =$

$Y^{(0)} + \delta Y$ with

$$Y^{(0)} = \begin{bmatrix} Y_{11} & Y_{12} & Y_{13} \\ 0 & Y_{22} & \Omega \\ 0 & -\Omega & Y_{33} \end{bmatrix} \tag{7.5.1}$$

in which $Y_{22} \approx Y_{33}$ and

$$\delta Y = \begin{bmatrix} 0 & 0 & 0 \\ Y_{21} & 0 & 0 \\ Y_{31} & 0 & 0 \end{bmatrix} \tag{7.5.2}$$

Figure 7.3 shows that δY can be treated in perturbation. The problem is that Y is not symmetric.

The eigenvalues of $Y^{(0)}$ are Y_{11} and $Y_{22} \pm i\Omega$. The eigenvalue $\lambda_1^{(0)} = Y_{11}$ is the one obtained in the RWA (section 7.3.3) which gives $T_1^{(0)} = -1/Y_{11}$ (equation 7.3.20). The corresponding eigenvector is $|u\rangle = \begin{bmatrix} 1 \\ 0 \\ 0 \end{bmatrix}$, i.e. $Y^{(0)}|u\rangle = Y_{11}|u\rangle$.

Our goal is to compute the first order perturbation $\delta\lambda_1$ induced by δY. The difficulty is that Y and δY are not symmetric. Reference [126] shows that we have to calculate the left eigenvector for the same eigenvalue,

$$\langle v|Y^{(0)} = \lambda_1^{(0)}\langle v| \tag{7.5.3}$$

in which $\langle v|$ is the complex conjugate transpose of $|v\rangle$. In this case, the first order perturbation correction is given by

$$\delta\lambda_1 = \langle v|\delta Y|u\rangle \tag{7.5.4}$$

In the case of the matrix Y of equation 7.5.1, the left eigenvector for the eigenvalue $\lambda_1^{(0)} = Y_{11}$ is

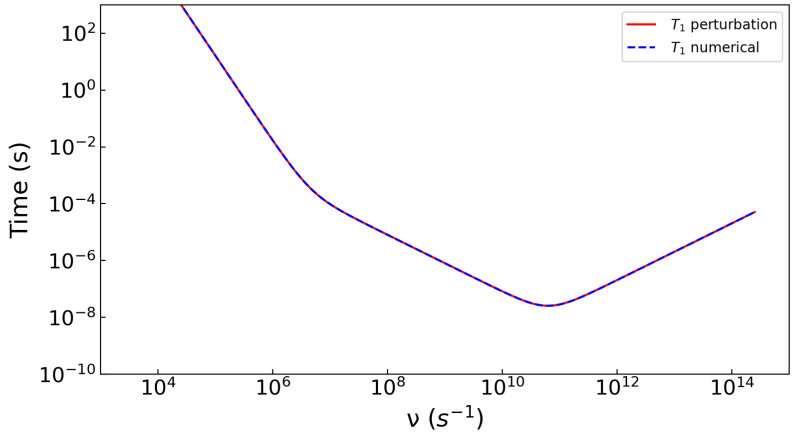

Figure 7.4: T_1 versus ν obtained using numerical resolution of Equation (7.3.8) or using the perturbative approach [Equation 7.5.6].

$$\langle v| = \begin{bmatrix} 1 & \frac{Y_{12}(Y_{11}-Y_{22})-Y_{13}\Omega}{\Omega^2+(Y_{11}-Y_{22})^2} & \frac{Y_{12}\Omega+Y_{13}(Y_{11}-Y_{22})}{\Omega^2+(Y_{11}-Y_{22})^2} \end{bmatrix} \tag{7.5.5}$$

Injecting this into the equation 7.5.4 gives

$$\lambda_1^{(0)} + \delta\lambda_1 = -\frac{1}{T_1} = Y_{11} + \frac{Y_{21}(Y_{12}(Y_{11}-Y_{22})-Y_{13}\Omega)+Y_{31}(Y_{12}\Omega+Y_{13}(Y_{11}-Y_{22}))}{\Omega^2+(Y_{11}-Y_{22})^2} \tag{7.5.6}$$

Figure 7.4 shows that this equation perfectly reproduces T_1 obtained by the numerical solution of the Bloch-Redfield equation, proving the validity of the perturbative approach. This shows that the change in behavior of $T_1(\nu)$ at low frequency is indeed a true result of the Bloch-Redfield model. It remains to be seen if it is physically relevant.

7.6 Low-frequency behavior of T_1 in the Bloch-Redfield theory

Deciding whether the low-frequency behavior of T_1 predicted by the Bloch-Redfield theory is correct or not requires the ability to perform time-dependent simulations over a longer period of time, which was not numerically possible. We have chosen

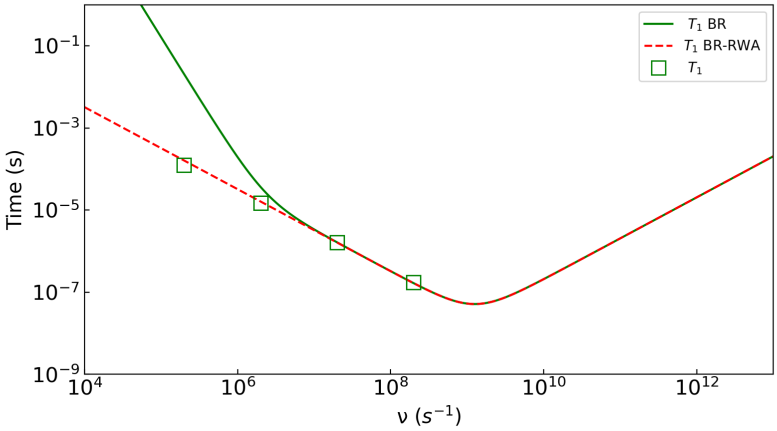

Figure 7.5: Values of T_1 calculated with Ω and U reduced by a factor 50 and 10, respectively. Green squares: time-dependent simulations. Green solid line: Bloch-Redfield theory. Red dashed line: Bloch-Redfield theory in the RWA.

another strategy. We considered a fictitious system in which the Larmor frequency is divided by 50 and the coupling matrix is divided by 10. In this case, it is possible to reduce the time step of the temporal simulations and consider situations allowing us to compare with the low-frequency regime of Bloch-Redfield.

Results are presented in Figure 7.5. They show that the low frequency behavior predicted by the Bloch-Redfield theory, i.e., a strong increase of T_1 when ν decreases, faster than $1/\nu$, is not reproduced by time-dependent simulations and therefore is not physical. This is consistent with the fact that the Bloch-Redfield theory is used here outside its domain of validity as shown in Figure 7.2.

7.7 Comparison with Bloch-Redfield in the RWA

We have seen in section 7.3.3 that the RWA allows us to arrive at analytical solutions of the Bloch-Redfield equation for T_1 and T_2. It is interesting to compare them with the results of time-dependent simulations (Figure 7.6). We find that for T_2 the Bloch-Redfield plus RWA predictions remains incorrect for $\nu < \omega_{th}$, which makes sense since the Gaussian description remains invalid in this case. On the contrary, the predictions for T_1 seem to be in excellent agreement with the time-

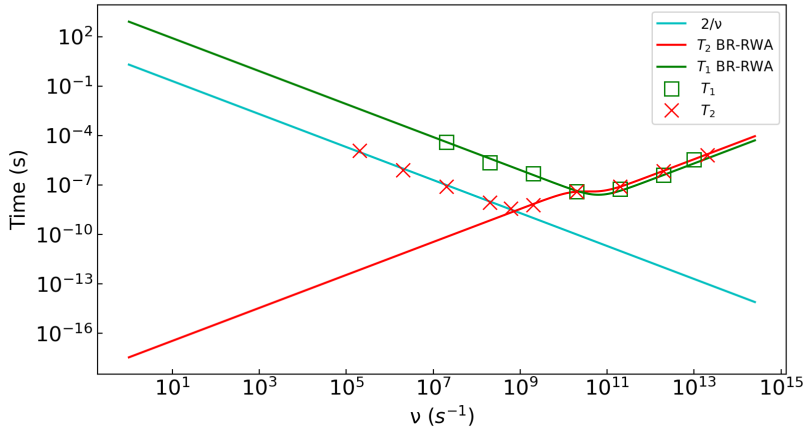

Figure 7.6: Characteristic times T_1 (green) and T_2 (red) obtained with the Bloch-Redfield theory in the RWA (solid lines) and with the time-dependent simulations (squares and crosses, respectively). The blue line represents a time varying as $2/\nu$.

dependent simulations whatever ν. This is confirmed in the case of the fictitious system with reduced Ω and U, Figure 7.5. This shows that the Bloch-Redfield theory in the RWA seems to describe correctly the values of T_1 of the two-level model, whatever the frequency of the fluctuator, which may seem surprising at first sight since it means that Bloch-Redfield theory works better with RWA than without approximation.

It is possible to give two first explanations for this result. First, the values of T_1 always remain much longer than the correlation time $1/\nu$, and thus the Gaussian approximation remains valid. Secondly, the RWA amounts to decoupling the equations for T_2 and T_1, and thus to annihilate the effect of the terms R_{0001} and R_{0101} which become problematic at low frequency.

In addition, we present in Appendix D an exact calculation of T_1 in the limit where $\nu \ll \Omega$. The obtained expression agrees with T_1 obtained by the Bloch-Redfield approach in the RWA (Equation 7.3.20).

7.8 Conclusion and outlook

In this section, we have applied the Bloch-Redfield theory to the two-level problem of a qubit perturbed by a random telegraphic noise. The results agree with exact time-dependent simulations at high frequency. This is no longer true at low frequency when the Gaussian approximation fails or when dynamical processes of the qubit spin determined by the transition rates of the Bloch-Redfield tensor become faster than the correlations of the fluctuator. However, the relaxation time T_1 is correctly given in the whole frequency range by the Bloch-Redfield theory in the RWA. These results clarify the domains of validity of the Bloch-Redfield theory for the problems of interest in this thesis.

Chapter 8

Conclusions

In this thesis, we focused on the theoretical study of the influence of quantum noise represented by a single charge fluctuator on a hole qubit in silicon technology. The background in this thesis was provided by the extensive theoretical and experimental work that was done at CEA on the development of a semiconductor quantum computer platform. Chapter 3 and 4 summarize some of this work. This helped us to understand better the physics of these qubits. Moreover, the bibliographical study presented in chapter 2 gave us a picture of the strategy that we have to follow to model a single charge fluctuator in a real device, which was realized in chapter 5 where we did not stop to consider the qubit system as a two-state system but to go further and ask the question: do the other states of the quantum dot play a role too?

8.1 General Conclusions

Thanks to the model developed in chapter 5, we have simulated the spin decoherence in a hole qubit due to the presence of a single charge fluctuator which undergoes telegraphic electrical noise. Thanks to the results obtained and discussed in chapter 6, we found that the dephasing time T_2 in the low frequency range ($\nu < \omega_{th}$) is not described by the Gaussian approximation due to the fact that the phase distribution in this regime is not Gaussian as expected by the

Bloch-Redfield theory. Simulations have shown that by playing on the orientation of the magnetic field, on the back gate potential and on the position of the fluctuator in the device, we can find points or lines called "sweet lines" on which the threshold frequency ω_{th} becomes smaller and consequently $T_2(\omega_{th})$ becomes longer and therefore the noise has a smaller influence. We also found that T_2 is dominated by the characteristic relaxation time T_1 in the high frequency range ($\nu \gg \omega_{th}$). Furthermore T_1 becomes shorter because of the additional coupling to the system in the case of multi-level model which results in the 2-level model not being sufficient in this case. Thanks to the theoretical physics, we could model and simulate the impact of a microscopic noise source which is almost impossible to filter and to isolate in experimental measurements, which shows the importance of simulation.

8.2 Perspectives

The perspectives of this thesis can be divided in two parts. The first one is to further develop the models used to better describe the decoherence of a hole qubit. In this work, we have studied the system from the semi-classical point of view where we have not taken into account the spontaneous emission and therefore it will be good to study the system from the purely quantum point of view and see the influence of the spontaneous emission on the decoherence, especially in the multi-level model whether it decreases or increases the effect of coupling to other states. An important study would be to simulate this effect by taking into account the electron-phonon coupling that will contribute to relax the system from high energy states to low energy ones.

There are several sources of microscopic noise that are not yet studied. So the second part of the prospects will be to study the influence of other existing noise sources such as the charge impurities in the source and drain of the transistor which may have a more dynamic aspect. In particular, it would be important to understand the origin of the $1/\sqrt{f}$ noise that has been observed experimentally and

that suggests the influence of very distant electric fluctuators that would operate in a Gaussian regime because ω_{th} is very small (weak coupling to the qubit) so the condition $\nu < \omega_{th}$ is likely.

The combination of experimental work and simulations as close as possible to the manufactured components remains more necessary than ever to advance in the development of quantum technologies in Si or SiGe.

References

[1] Andrew Steane. Quantum computing. *Reports on Progress in Physics*, 61 (2):117–173, feb 1998. doi: 10.1088/0034-4885/61/2/002. URL https://doi.org/10.1088/0034-4885/61/2/002.

[2] Thaddeus D Ladd, Fedor Jelezko, Raymond Laflamme, Yasunobu Nakamura, Christopher Monroe, and Jeremy Lloyd O'Brien. Quantum computers. *nature*, 464(7285):45–53, 2010.

[3] Andrea Corna, Léo Bourdet, Romain Maurand, Alessandro Crippa, Dharmraj Kotekar-Patil, Heorhii Bohuslavskyi, Romain Laviéville, Louis Hutin, Sylvain Barraud, Xavier Jehl, et al. Electrically driven electron spin resonance mediated by spin–valley–orbit coupling in a silicon quantum dot. *npj quantum information*, 4(1):1–7, 2018.

[4] John JL Morton, Dane R McCamey, Mark A Eriksson, and Stephen A Lyon. Embracing the quantum limit in silicon computing. *Nature*, 479(7373):345–353, 2011.

[5] Werner Weber. Adiabatic bond charge model for the phonons in diamond, Si, Ge, and α - Sn. *Physical Review B*, 15(10):4789–4803, May 1977. ISSN 0556-2805. doi: 10.1103/PhysRevB.15.4789. URL https://link.aps.org/doi/10.1103/PhysRevB.15.4789.

[6] M. Hofheinz, X. Jehl, M. Sanquer, G. Molas, M. Vinet, and S. Deleonibus. Simple and controlled single electron transistor based on doping modulation in silicon nanowires. *Applied Physics Letters*, 89(14):143504, October 2006.

ISSN 0003-6951, 1077-3118. doi: 10.1063/1.2358812. URL http://aip.scitation.org/doi/10.1063/1.2358812.

[7] R. Maurand, X. Jehl, D. Kotekar-Patil, A. Corna, H. Bohuslavskyi, R. LavIÃĬville, L. Hutin, S. Barraud, M. Vinet, M. Sanquer, and S. De Franceschi. A CMOS silicon spin qubit. *Nature Communications*, 7(1):13575, December 2016. ISSN 2041-1723. doi: 10.1038/ncomms13575. URL http://www.nature.com/articles/ncomms13575.

[8] Floris A. Zwanenburg, Andrew S. Dzurak, Andrea Morello, Michelle Y. Simmons, Lloyd C. L. Hollenberg, Gerhard Klimeck, Sven Rogge, Susan N. Coppersmith, and Mark A. Eriksson. Silicon quantum electronics. *Reviews of Modern Physics*, 85(3):961–1019, July 2013. ISSN 0034-6861, 1539-0756. doi: 10.1103/RevModPhys.85.961. URL https://link.aps.org/doi/10.1103/RevModPhys.85.961.

[9] Leo Bourdet. Modeling of electrical manipulation in silicon spin qubits. page 168.

[10] W. G. van der Wiel, S. De Franceschi, J. M. Elzerman, T. Fujisawa, S. Tarucha, and L. P. Kouwenhoven. Electron transport through double quantum dots. *Reviews of Modern Physics*, 75(1):1–22, December 2002. doi: 10.1103/RevModPhys.75.1. URL https://link.aps.org/doi/10.1103/RevModPhys.75.1. Publisher: American Physical Society.

[11] R. Hanson, L. P. Kouwenhoven, J. R. Petta, S. Tarucha, and L. M. K. Vandersypen. Spins in few-electron quantum dots. *Reviews of Modern Physics*, 79(4):1217–1265, October 2007. doi: 10.1103/RevModPhys.79.1217. URL https://link.aps.org/doi/10.1103/RevModPhys.79.1217. Publisher: American Physical Society.

[12] M Hofheinz, X Jehl, M Sanquer, G Molas, M Vinet, and S Deleonibus. Simple and controlled single electron transistor based on doping modulation in silicon nanowires. *Applied physics letters*, 89(14):143504, 2006.

[13] Alessandro Crippa, Romain Maurand, Léo Bourdet, Dharmraj Kotekar-Patil, Anthony Amisse, Xavier Jehl, Marc Sanquer, Romain Laviéville, Heorhii Bohuslavskyi, Louis Hutin, Sylvain Barraud, Maud Vinet, Yann-Michel Niquet, and Silvano De Franceschi. Electrical Spin Driving by g-Matrix Modulation in Spin-Orbit Qubits. *Physical Review Letters*, 120(13): 137702, March 2018. doi: 10.1103/PhysRevLett.120.137702. URL https://link.aps.org/doi/10.1103/PhysRevLett.120.137702. Publisher: American Physical Society.

[14] Y. M. Niquet, D. Rideau, C. Tavernier, H. Jaouen, and X. Blase. Onsite matrix elements of the tight-binding Hamiltonian of a strained crystal: Application to silicon, germanium, and their alloys. *Physical Review B*, 79 (24):245201, June 2009. doi: 10.1103/PhysRevB.79.245201. URL https://link.aps.org/doi/10.1103/PhysRevB.79.245201. Publisher: American Physical Society.

[15] Benjamin Venitucci. Modélisation de la manipulation électrique des qubits de trou dans le silicium. page 135.

[16] J Bergli, Y M Galperin, and B L Altshuler. Decoherence in qubits due to low-frequency noise. *New Journal of Physics*, 11(2):025002, feb 2009. doi: 10.1088/1367-2630/11/2/025002. URL https://doi.org/10.1088/1367-2630/11/2/025002.

[17] E. Paladino, Y. M. Galperin, G. Falci, and B. L. Altshuler. 1 / f noise: Implications for solid-state quantum information. *Reviews of Modern Physics*, 86(2):361–418, April 2014. ISSN 0034-6861, 1539-0756. doi: 10.1103/RevModPhys.86.361. URL https://link.aps.org/doi/10.1103/RevModPhys.86.361.

[18] N. Piot, B. Brun, V. Schmitt, S. Zihlmann, V. P. Michal, A. Apra, J. C. Abadillo-Uriel, X. Jehl, B. Bertrand, H. Niebojewski, L. Hutin, M. Vinet, M. Urdampilleta, T. Meunier, Y.-M. Niquet, R. Maurand, and S. De Franceschi. A single hole spin with enhanced coherence in natural silicon.

Nature Nanotechnology, 17(10):1072–1077, October 2022. ISSN 1748-3387, 1748-3395. doi: 10.1038/s41565-022-01196-z. URL https://www.nature.com/articles/s41565-022-01196-z.

[19] Elena Ferraro and Enrico Prati. Is all-electrical silicon quantum computing feasible in the long term? *Physics Letters A*, 384(17):126352, 2020.

[20] *Spin-orbit Coupling Effects in Two-Dimensional Electron and Hole Systems*. . URL https://link.springer.com/book/10.1007/b13586.

[21] Michael Riordan, Lillian Hoddeson, and Conyers Herring. *The Invention of the Transistor*, pages 563–578. Springer New York, New York, NY, 1999. ISBN 978-1-4612-1512-7. doi: 10.1007/978-1-4612-1512-7_37. URL https://doi.org/10.1007/978-1-4612-1512-7_37.

[22] Gordon E Moore et al. Progress in digital integrated electronics. In *Electron devices meeting*, volume 21, pages 11–13. Washington, DC, 1975.

[23] Richard P Feynman et al. Simulating physics with computers. *Int. j. Theor. phys*, 21(6/7), 1982.

[24] Peter W. Shor. Polynomial-time algorithms for prime factorization and discrete logarithms on a quantum computer. *SIAM Review*, 41(2):303–332, 1999. doi: 10.1137/S0036144598347011. URL https://doi.org/10.1137/S0036144598347011.

[25] Lov K Grover. A fast quantum mechanical algorithm for database search. In *Proceedings of the twenty-eighth annual ACM symposium on Theory of computing*, pages 212–219, 1996.

[26] Isaac L. Chuang, Neil Gershenfeld, and Mark Kubinec. Experimental implementation of fast quantum searching. *Phys. Rev. Lett.*, 80:3408–3411, Apr 1998. doi: 10.1103/PhysRevLett.80.3408. URL https://link.aps.org/doi/10.1103/PhysRevLett.80.3408.

[27] IBM Unveils 400 Qubit-Plus Quantum Processor and Next-Generation IBM Quantum System Two, . URL https://newsroom.ibm.com/2022-11-09-IBM-Unveils-400-Qubit-Plus-Quantum-Processor-and-Next-Generatio

[28] C. H. Bennett. Logical reversibility of computation. *IBM Journal of Research and Development*, 17(6):525–532, 1973. doi: 10.1147/rd.176.0525.

[29] Charles H Bennett. The thermodynamics of computation-a review. *International Journal of Theoretical Physics*, 21(12):905–940, 1982.

[30] Stephen Wiesner. Conjugate coding. *ACM Sigact News*, 15(1):78–88, 1983.

[31] Gilles Brassard and Claude Crépeau. 25 years of quantum cryptography. *ACM Sigact News*, 27(3):13–24, 1996.

[32] Richard P Feynman. Quantum mechanical computers. *Foundations of physics*, 16(6):507–531, 1986.

[33] Daniel R Simon. On the power of quantum computation. *SIAM journal on computing*, 26(5):1474–1483, 1997.

[34] Richard Jozsa and Benjamin Schumacher. A new proof of the quantum noiseless coding theorem. *Journal of Modern Optics*, 41(12):2343–2349, 1994.

[35] Benjamin Schumacher. Quantum coding. *Physical Review A*, 51(4):2738, 1995.

[36] Matthew Neeley, Radoslaw C Bialczak, M Lenander, Erik Lucero, Matteo Mariantoni, AD O'connell, D Sank, H Wang, M Weides, J Wenner, et al. Generation of three-qubit entangled states using superconducting phase qubits. *Nature*, 467(7315):570–573, 2010.

[37] Richard Harris, Mark W Johnson, T Lanting, AJ Berkley, J Johansson, P Bunyk, E Tolkacheva, E Ladizinsky, N Ladizinsky, T Oh, et al. Experimental investigation of an eight-qubit unit cell in a superconducting optimization processor. *Physical Review B*, 82(2):024511, 2010.

[38] Aaron D OâĂŹConnell, Max Hofheinz, Markus Ansmann, Radoslaw C Bialczak, Mike Lenander, Erik Lucero, Matthew Neeley, Daniel Sank, H Wang, Martin Weides, et al. Quantum ground state and single-phonon control of a mechanical resonator. *Nature*, 464(7289):697–703, 2010.

[39] John Clarke and Frank K Wilhelm. Superconducting quantum bits. *Nature*, 453(7198):1031–1042, 2008.

[40] JQ You and Franco Nori. Superconducting circuits and quantum information. *arXiv preprint quant-ph/0601121*, 2006.

[41] Yuriy Makhlin, Gerd Schön, and Alexander Shnirman. Quantum-state engineering with josephson-junction devices. *Reviews of modern physics*, 73(2): 357, 2001.

[42] Jian-Qiang You and Franco Nori. Atomic physics and quantum optics using superconducting circuits. *Nature*, 474(7353):589–597, 2011.

[43] M Büttiker. Zero-current persistent potential drop across small-capacitance josephson junctions. *Physical Review B*, 36(7):3548, 1987.

[44] Alexander Shnirman, Gerd Schön, and Ziv Hermon. Quantum manipulations of small josephson junctions. *Physical Review Letters*, 79(12):2371, 1997.

[45] Vincent Bouchiat, D Vion, Ph Joyez, D Esteve, and MH Devoret. Quantum coherence with a single cooper pair. *Physica Scripta*, 1998(T76):165, 1998.

[46] Yasunobu Nakamura, Yu A Pashkin, and JS Tsai. Coherent control of macroscopic quantum states in a single-cooper-pair box. *nature*, 398(6730):786–788, 1999.

[47] Denis Vion, A Aassime, Audrey Cottet, Pl Joyez, H Pothier, C Urbina, Daniel Esteve, and Michel H Devoret. Manipulating the quantum state of an electrical circuit. *Science*, 296(5569):886–889, 2002.

[48] AA Houck, JA Schreier, BR Johnson, JM Chow, Jens Koch, JM Gambetta, DI Schuster, L Frunzio, MH Devoret, SM Girvin, et al. Controlling the spontaneous emission of a superconducting transmon qubit. *Physical review letters*, 101(8):080502, 2008.

[49] Anthony J Leggett. Macroscopic quantum systems and the quantum theory of measurement. *Progress of Theoretical Physics Supplement*, 69:80–100, 1980.

[50] JE Mooij, TP Orlando, L Levitov, Lin Tian, Caspar H Van der Wal, and Seth Lloyd. Josephson persistent-current qubit. *Science*, 285(5430):1036–1039, 1999.

[51] Irinel Chiorescu, Y Nakamura, CJP Ma Harmans, and JE Mooij. Coherent quantum dynamics of a superconducting flux qubit. *Science*, 299(5614): 1869–1871, 2003.

[52] John M Martinis, Sae Nam, Joe Aumentado, and C Urbina. Rabi oscillations in a large josephson-junction qubit. *Physical review letters*, 89(11):117901, 2002.

[53] Jonas Bylander, Simon Gustavsson, Fei Yan, Fumiki Yoshihara, Khalil Harrabi, George Fitch, David G Cory, Yasunobu Nakamura, Jaw-Shen Tsai, and William D Oliver. Noise spectroscopy through dynamical decoupling with a superconducting flux qubit. *Nature Physics*, 7(7):565–570, 2011.

[54] Travis Hime, PA Reichardt, BLT Plourde, TL Robertson, C-E Wu, AV Ustinov, and John Clarke. Solid-state qubits with current-controlled coupling. *science*, 314(5804):1427–1429, 2006.

[55] AO Niskanen, K Harrabi, F Yoshihara, Y Nakamura, S Lloyd, and Jaw Shen Tsai. Quantum coherent tunable coupling of superconducting qubits. *Science*, 316(5825):723–726, 2007.

[56] R Blatt and P Zoller. Quantum jumps in atomic systems. *European Journal of Physics*, 9(4):250, 1988.

[57] M Acton, K-A Brickman, PC Haljan, PJ Lee, L Deslauriers, and C Monroe. Near-perfect simultaneous measurement of a qubit register. *arXiv preprint quant-ph/0511257*, 2005.

[58] David J Wineland, C Monroe, Wayne M Itano, Dietrich Leibfried, Brian E King, and Dawn M Meekhof. Experimental issues in coherent quantum-state manipulation of trapped atomic ions. *Journal of research of the National Institute of Standards and Technology*, 103(3):259, 1998.

[59] Rainer Blatt and David Wineland. Entangled states of trapped atomic ions. *Nature*, 453(7198):1008–1015, 2008.

[60] Juan I Cirac and Peter Zoller. Quantum computations with cold trapped ions. *Physical review letters*, 74(20):4091, 1995.

[61] Chris Monroe, David M Meekhof, Barry E King, Wayne M Itano, and David J Wineland. Demonstration of a fundamental quantum logic gate. *Physical review letters*, 75(25):4714, 1995.

[62] Dietrich Leibfried, Rainer Blatt, Christopher Monroe, and David Wineland. Quantum dynamics of single trapped ions. *Reviews of Modern Physics*, 75 (1):281, 2003.

[63] David Kielpinski, Chris Monroe, and David J Wineland. Architecture for a large-scale ion-trap quantum computer. *Nature*, 417(6890):709–711, 2002.

[64] Daniel Loss and David P DiVincenzo. Quantum computation with quantum dots. *Physical Review A*, 57(1):120, 1998.

[65] Hermann Grabert and Michel H. Devoret. *Single Charge Tunneling: Coulomb Blockade Phenomena in Nanostructures*. Springer, New York, NY, 2013. ISBN 978-1-4757-2166-9. OCLC: 1066178774.

[66] B. E. Kane. A silicon-based nuclear spin quantum computer. *Nature*, 393 (6681):133–137, May 1998. ISSN 0028-0836, 1476-4687. doi: 10.1038/30156. URL http://www.nature.com/articles/30156.

[67] Lars R Schreiber and Hendrik Bluhm. Silicon comes back. *Nature nanotechnology*, 9(12):966–968, 2014.

[68] Jarryd J Pla, Kuan Y Tan, Juan P Dehollain, Wee H Lim, John JL Morton, David N Jamieson, Andrew S Dzurak, and Andrea Morello. A single-atom electron spin qubit in silicon. *Nature*, 489(7417):541–545, 2012.

[69] R Maurand, X Jehl, D Kotekar-Patil, A Corna, H Bohuslavskyi, R Laviéville, L Hutin, S Barraud, M Vinet, M Sanquer, et al. A cmos silicon spin qubit. *Nature communications*, 7(1):1–6, 2016.

[70] L Hutin, R Maurand, D Kotekar-Patil, A Corna, H Bohuslavskyi, X Jehl, S Barraud, S De Franceschi, M Sanquer, and M Vinet. Si cmos platform for quantum information processing. In *2016 IEEE Symposium on VLSI Technology*, pages 1–2. IEEE, 2016.

[71] Alessandro Crippa, Romain Maurand, Léo Bourdet, Dharmraj Kotekar-Patil, Anthony Amisse, Xavier Jehl, Marc Sanquer, Romain Laviéville, Heorhii Bohuslavskyi, Louis Hutin, et al. Electrical spin driving by g-matrix modulation in spin-orbit qubits. *Physical review letters*, 120(13):137702, 2018.

[72] Erika Kawakami, Pasquale Scarlino, Daniel R Ward, FR Braakman, DE Savage, MG Lagally, Mark Friesen, Susan N Coppersmith, Mark A Eriksson, and LMK Vandersypen. Electrical control of a long-lived spin qubit in a si/sige quantum dot. *Nature nanotechnology*, 9(9):666–670, 2014.

[73] Menno Veldhorst, CH Yang, JCC Hwang, W Huang, JP Dehollain, JT Muhonen, S Simmons, A Laucht, FE Hudson, Kohei M Itoh, et al. A two-qubit logic gate in silicon. *Nature*, 526(7573):410–414, 2015.

[74] Juha T Muhonen, Juan P Dehollain, Arne Laucht, Fay E Hudson, Rachpon Kalra, Takeharu Sekiguchi, Kohei M Itoh, David N Jamieson, Jeffrey C McCallum, Andrew S Dzurak, et al. Storing quantum information for 30

seconds in a nanoelectronic device. *Nature nanotechnology*, 9(12):986–991, 2014.

[75] Kenta Takeda, Akito Noiri, Jun Yoneda, Takashi Nakajima, and Seigo Tarucha. Resonantly driven singlet-triplet spin qubit in silicon. *Physical Review Letters*, 124(11):117701, 2020.

[76] Dohun Kim, Zhan Shi, CB Simmons, DR Ward, JR Prance, Teck Seng Koh, John King Gamble, DE Savage, MG Lagally, Mark Friesen, et al. Quantum control and process tomography of a semiconductor quantum dot hybrid qubit. *Nature*, 511(7507):70–74, 2014.

[77] Alessandro Crippa, R Ezzouch, A Aprá, A Amisse, R Laviéville, L Hutin, B Bertrand, M Vinet, Matias Urdampilleta, Tristan Meunier, et al. Gate-reflectometry dispersive readout and coherent control of a spin qubit in silicon. *Nature communications*, 10(1):1–6, 2019.

[78] Jim Clarke. Spin qubits at intel. In *APS March Meeting Abstracts*, volume 2019, pages B35–001, 2019.

[79] Ruoyu Li, Luca Petit, David P Franke, Juan Pablo Dehollain, Jonas Helsen, Mark Steudtner, Nicole K Thomas, Zachary R Yoscovits, Kanwal J Singh, Stephanie Wehner, et al. A crossbar network for silicon quantum dot qubits. *Science advances*, 4(7):eaar3960, 2018.

[80] Davide Rotta, Fabio Sebastiano, Edoardo Charbon, and Enrico Prati. Quantum information density scaling and qubit operation time constraints of cmos silicon-based quantum computer architectures. *npj Quantum Information*, 3(1):1–14, 2017.

[81] Jay M Gambetta, Jerry M Chow, and Matthias Steffen. Building logical qubits in a superconducting quantum computing system. *npj Quantum Information*, 3(1):1–7, 2017.

[82] Abhinav Kandala, Antonio Mezzacapo, Kristan Temme, Maika Takita, Markus Brink, Jerry M Chow, and Jay M Gambetta. Hardware-efficient

variational quantum eigensolver for small molecules and quantum magnets. *Nature*, 549(7671):242–246, 2017.

[83] Bjoern Lekitsch, Sebastian Weidt, Austin G Fowler, Klaus Mølmer, Simon J Devitt, Christof Wunderlich, and Winfried K Hensinger. Blueprint for a microwave trapped ion quantum computer. *Science Advances*, 3(2):e1601540, 2017.

[84] W. M. Witzel and S. Das Sarma. Quantum theory for electron spin decoherence induced by nuclear spin dynamics in semiconductor quantum computer architectures: Spectral diffusion of localized electron spins in the nuclear solid-state environment. *Physical Review B*, 74(3):035322, July 2006. ISSN 1098-0121, 1550-235X. doi: 10.1103/PhysRevB.74.035322. URL https://link.aps.org/doi/10.1103/PhysRevB.74.035322.

[85] J. W. Ager, J. W. Beeman, W. L. Hansen, E. E. Haller, I. D. Sharp, C. Liao, A. Yang, M. L. W. Thewalt, and H. Riemann. High-Purity, Isotopically Enriched Bulk Silicon. *Journal of The Electrochemical Society*, 152(6):G448, 2005. ISSN 00134651. doi: 10.1149/1.1901674. URL https://iopscience.iop.org/article/10.1149/1.1901674.

[86] B Andreas, Y Azuma, G Bartl, P Becker, H Bettin, M Borys, I Busch, P Fuchs, K Fujii, H Fujimoto, E Kessler, M Krumrey, U Kuetgens, N Kuramoto, G Mana, E Massa, S Mizushima, A Nicolaus, A Picard, A Pramann, O Rienitz, D Schiel, S Valkiers, A Waseda, and S Zakel. Counting the atoms in a si crystal for a new kilogram definition. *Metrologia*, 48(2):S1–S13, April 2011. ISSN 0026-1394, 1681-7575. doi: 10.1088/0026-1394/48/2/S01. URL https://iopscience.iop.org/article/10.1088/0026-1394/48/2/S01.

[87] P. Dutta and P. M. Horn. Low-frequency fluctuations in solids: 1 f noise. *Reviews of Modern Physics*, 53(3):497–516, July 1981. ISSN 0034-6861. doi: 10.1103/RevModPhys.53.497. URL https://link.aps.org/doi/10.1103/RevModPhys.53.497.

[88] M. B. Weissman. 1 f noise and other slow, nonexponential kinetics in condensed matter. *Reviews of Modern Physics*, 60(2):537–571, April 1988. ISSN 0034-6861. doi: 10.1103/RevModPhys.60.537. URL https://link.aps.org/doi/10.1103/RevModPhys.60.537.

[89] Sh. Kogan. *Electronic Noise and Fluctuations in Solids*. Cambridge University Press, 1 edition, August 1996. ISBN 978-0-521-46034-7 978-0-521-07019-5 978-0-511-55166-6. doi: 10.1017/CBO9780511551666. URL https://www.cambridge.org/core/product/identifier/9780511551666/type/book.

[90] Richard Fitzhugh. Statistical properties of the asymmetric random telegraph signal, with applications to single-channel analysis. *Mathematical Biosciences*, 64(1):75–89, May 1983. ISSN 00255564. doi: 10.1016/0025-5564(83)90028-7. URL https://linkinghub.elsevier.com/retrieve/pii/0025556483900287.

[91] Benjamin Simon Abel. *Macroscopic superposition states and decoherence by quantum telegraph noise*. PhD thesis, Ludwig-Maximilians-Universität MÃijnchen, 2009. URL https://edoc.ub.uni-muenchen.de/id/eprint/9828. Medium: application/pdf.

[92] Claude Cohen-Tannoudji, Jacques Dupont-Roc, and Gilbert Grynberg. *Atom-Photon Interactions: Basic Process and Appilcations*. Wiley, 1 edition, April 1998. ISBN 978-0-471-29336-1 978-3-527-61719-7. doi: 10.1002/9783527617197. URL https://onlinelibrary.wiley.com/doi/book/10.1002/9783527617197.

[93] F. Bloch. Generalized Theory of Relaxation. *Physical Review*, 105(4):1206–1222, February 1957. ISSN 0031-899X. doi: 10.1103/PhysRev.105.1206. URL https://link.aps.org/doi/10.1103/PhysRev.105.1206.

[94] A. G. Redfield. On the Theory of Relaxation Processes. *IBM Journal of Research and Development*, 1(1):19–31, January 1957. ISSN 0018-8646, 0018-8646. doi: 10.1147/rd.11.0019. URL http://ieeexplore.ieee.org/lpdocs/epic03/wrapper.htm?arnumber=5392713.

[95] Ulrich Weiss. *Quantum Dissipative Systems*, volume 13 of *Series in Modern Condensed Matter Physics*. WORLD SCIENTIFIC, 3 edition, March 2008. ISBN 978-981-279-162-7 978-981-279-179-5. doi: 10.1142/6738. URL https://www.worldscientific.com/worldscibooks/10.1142/6738.

[96] Andrea Corna, Léo Bourdet, Romain Maurand, Alessandro Crippa, Dharmraj Kotekar-Patil, Heorhii Bohuslavskyi, Romain Laviéville, Louis Hutin, Sylvain Barraud, Xavier Jehl, Maud Vinet, Silvano De Franceschi, Yann-Michel Niquet, and Marc Sanquer. Electrically driven electron spin resonance mediated by spin-valley-orbit coupling in a silicon quantum dot. *npj Quantum Information*, 4(1):6, December 2018. ISSN 2056-6387. doi: 10.1038/s41534-018-0059-1. URL http://www.nature.com/articles/s41534-018-0059-1.

[97] D. Kotekar-Patil, A. Corna, R. Maurand, A. Crippa, A. Orlov, S. Barraud, L. Hutin, M. Vinet, X. Jehl, S. De Franceschi, and M. Sanquer. Pauli spin blockade in CMOS double quantum dot devices: Pauli spin blockade in CMOS double quantum dot devices. *physica status solidi (b)*, 254(3): 1600581, March 2017. ISSN 03701972. doi: 10.1002/pssb.201600581. URL https://onlinelibrary.wiley.com/doi/10.1002/pssb.201600581.

[98] H. Bohuslavskyi, D. Kotekar-Patil, R. Maurand, A. Corna, S. Barraud, L. Bourdet, L. Hutin, Y.-M. Niquet, X. Jehl, S. De Franceschi, M. Vinet, and M. Sanquer. Pauli blockade in a few-hole PMOS double quantum dot limited by spin-orbit interaction. *Applied Physics Letters*, 109(19):193101, November 2016. ISSN 0003-6951. doi: 10.1063/1.4966946. URL https://aip.scitation.org/doi/abs/10.1063/1.4966946. Publisher: American Institute of Physics.

[99] Dispersively Detected Pauli Spin-Blockade in a Silicon Nanowire Field-Effect Transistor | Nano Letters, . URL https://pubs.acs.org/doi/abs/10.1021/acs.nanolett.5b01306.

[100] M. F. Gonzalez-Zalba, A. J. Ferguson, S. Barraud, and A. C. Betz. A high-

sensitivity gate-based charge sensor in silicon. *Nature Communications*, 6 (1):6084, May 2015. ISSN 2041-1723. doi: 10.1038/ncomms7084. URL http://arxiv.org/abs/1405.2755. arXiv:1405.2755 [cond-mat].

[101] Alessandro Crippa, Romain Maurand, Dharmraj Kotekar-Patil, Andrea Corna, Heorhii Bohuslavskyi, Alexei O. Orlov, Patrick Fay, Romain Laviéville, Sylvain Barraud, Maud Vinet, Marc Sanquer, Silvano De Franceschi, and Xavier Jehl. Level Spectrum and Charge Relaxation in a Silicon Double Quantum Dot Probed by Dual-Gate Reflectometry. *Nano Letters*, 17 (2):1001–1006, February 2017. ISSN 1530-6984. doi: 10.1021/acs.nanolett.6b04354. URL https://doi.org/10.1021/acs.nanolett.6b04354. Publisher: American Chemical Society.

[102] G. Dresselhaus. Spin-Orbit Coupling Effects in Zinc Blende Structures. *Physical Review*, 100(2):580–586, October 1955. doi: 10.1103/PhysRev.100.580. URL https://link.aps.org/doi/10.1103/PhysRev.100.580. Publisher: American Physical Society.

[103] M. O. Nestoklon, L. E. Golub, and E. L. Ivchenko. Spin and valley-orbit splittings in SiGe/Si heterostructures. *Physical Review B*, 73(23): 235334, June 2006. doi: 10.1103/PhysRevB.73.235334. URL https://link.aps.org/doi/10.1103/PhysRevB.73.235334. Publisher: American Physical Society.

[104] L. E. Golub and E. L. Ivchenko. Spin splitting in symmetrical SiGe quantum wells. *Physical Review B*, 69(11):115333, March 2004. doi: 10.1103/PhysRevB.69.115333. URL https://link.aps.org/doi/10.1103/PhysRevB.69.115333. Publisher: American Physical Society.

[105] John J. L. Morton, Dane R. McCamey, Mark A. Eriksson, and Stephen A. Lyon. Embracing the quantum limit in silicon computing. *Nature*, 479(7373): 345–353, November 2011. ISSN 1476-4687. doi: 10.1038/nature10681. URL https://www.nature.com/articles/nature10681. Number: 7373 Publisher: Nature Publishing Group.

[106] A. M. Tyryshkin, J. J. L. Morton, S. C. Benjamin, A. Ardavan, G. A. D. Briggs, J. W. Ager, and S. A. Lyon. Coherence of spin qubits in silicon. *Journal of Physics: Condensed Matter*, 18(21):S783–S794, May 2006. ISSN 0953-8984. doi: 10.1088/0953-8984/18/21/S06. URL https://doi.org/10.1088/0953-8984/18/21/s06. Publisher: IOP Publishing.

[107] Alexei M. Tyryshkin, Shinichi Tojo, John J. L. Morton, Helge Riemann, Nikolai V. Abrosimov, Peter Becker, Hans-Joachim Pohl, Thomas Schenkel, Michael L. W. Thewalt, Kohei M. Itoh, and S. A. Lyon. Electron spin coherence exceeding seconds in high-purity silicon. *Nature Materials*, 11 (2):143–147, February 2012. ISSN 1476-4660. doi: 10.1038/nmat3182. URL https://www.nature.com/articles/nmat3182. Number: 2 Publisher: Nature Publishing Group.

[108] J. M. Elzerman, R. Hanson, J. S. Greidanus, L. H. Willems van Beveren, S. De Franceschi, L. M. K. Vandersypen, S. Tarucha, and L. P. Kouwenhoven. Few-electron quantum dot circuit with integrated charge read out. *Physical Review B*, 67(16):161308, April 2003. doi: 10.1103/PhysRevB.67.161308. URL https://link.aps.org/doi/10.1103/PhysRevB.67.161308. Publisher: American Physical Society.

[109] CEA. Modeling of the electrical manipulation of hole spin qubits in silicon, November 2020. URL https://www.mem-lab.fr/en/Pages/L_SIM/Theses/Benjamin-Venitucci.aspx. Publisher: CEA.

[110] Benjamin Venitucci, Léo Bourdet, Daniel Pouzada, and Yann-Michel Niquet. Electrical manipulation of semiconductor spin qubits within the g -matrix formalism. *Physical Review B*, 98(15):155319, October 2018. ISSN 2469-9950, 2469-9969. doi: 10.1103/PhysRevB.98.155319. URL https://link.aps.org/doi/10.1103/PhysRevB.98.155319.

[111] Guy Fishman. *Semi-conducteurs: les bases de la théorie k.p*. Physique. Les Éditions de l'École polytechnique, Palaiseau, 2010. ISBN 978-2-7302-1497-1.

[112] Per-Olov Löwdin. A Note on the Quantum-Mechanical Perturbation Theory. *The Journal of Chemical Physics*, 19(11):1396–1401, November 1951. ISSN 0021-9606. doi: 10.1063/1.1748067. URL https://aip-scitation-org.ressources-electroniques.univ-lille.fr/doi/abs/10.1063/1.1748067. Publisher: American Institute of Physics.

[113] G. Dresselhaus, A. F. Kip, and C. Kittel. Cyclotron Resonance of Electrons and Holes in Silicon and Germanium Crystals. *Physical Review*, 98(2):368–384, April 1955. doi: 10.1103/PhysRev.98.368. URL https://link.aps.org/doi/10.1103/PhysRev.98.368. Publisher: American Physical Society.

[114] E.O. Kane. Energy band structure in p-type germanium and silicon. *Journal of Physics and Chemistry of Solids*, 1(1-2):82–99, September 1956. ISSN 00223697. doi: 10.1016/0022-3697(56)90014-2. URL https://linkinghub.elsevier.com/retrieve/pii/0022369756900142.

[115] Lok C. Lew Yan Voon and Morten Willatzen. *The k p Method: Electronic Properties of Semiconductors*. Springer Science & Business Media, June 2009. ISBN 978-3-540-92872-0. Google-Books-ID: t46OZQrEd8QC.

[116] J. M. Luttinger and W. Kohn. Motion of Electrons and Holes in Perturbed Periodic Fields. *Physical Review*, 97(4):869–883, February 1955. doi: 10.1103/PhysRev.97.869. URL https://link.aps.org/doi/10.1103/PhysRev.97.869. Publisher: American Physical Society.

[117] Richard Barrett, Michael Berry, Tony F Chan, James Demmel, June M Donato, Jack Dongarra, Victor Eijkhout, Roldan Pozo, and Charles Romine. Templates for the Solution of Linear Systems: Building Blocks for Iterative Methods. page 117.

[118] David J. Griffiths. *Introduction to electrodynamics*. Pearson, Boston, fourth edition edition, 2013. ISBN 978-0-321-85656-2.

[119] C Leforestier, R.H Bisseling, C Cerjan, M.D Feit, R Friesner, A Guldberg, A Hammerich, G Jolicard, W Karrlein, H.-D Meyer, N Lipkin, O Roncero, and R Kosloff. A comparison of different propagation schemes for the time dependent schrÃűdinger equation. *Journal of Computational Physics*, 94(1): 59–80, 1991. ISSN 0021-9991. doi: https://doi.org/10.1016/0021-9991(91)90137-A. URL https://www.sciencedirect.com/science/article/pii/002199919190137A.

[120] Mamadou Ndong, Hillel Tal-Ezer, Ronnie Kosloff, and Christiane P. Koch. A Chebychev propagator with iterative time ordering for explicitly time-dependent Hamiltonians. *The Journal of Chemical Physics*, 132(6):064105, February 2010. ISSN 0021-9606, 1089-7690. doi: 10.1063/1.3312531. URL http://aip.scitation.org/doi/10.1063/1.3312531.

[121] R. Landauer and Th. Martin. Barrier interaction time in tunneling. *Reviews of Modern Physics*, 66(1):217–228, January 1994. ISSN 0034-6861, 1539-0756. doi: 10.1103/RevModPhys.66.217. URL https://link.aps.org/doi/10.1103/RevModPhys.66.217.

[122] Pierre FÃŀvrier and Julien Gabelli. Tunneling time probed by quantum shot noise. *Nature Communications*, 9(1):4940, November 2018. ISSN 2041-1723. doi: 10.1038/s41467-018-07369-6. URL https://www.nature.com/articles/s41467-018-07369-6.

[123] E. L. Hahn. Spin Echoes. *Physical Review*, 80(4):580–594, November 1950. ISSN 0031-899X. doi: 10.1103/PhysRev.80.580. URL https://link.aps.org/doi/10.1103/PhysRev.80.580.

[124] Claude Cohen-Tannoudji, Jacques Dupont-Roc, and Gilbert Grynberg. *Atom-photon interactions: basic processes and applications*. Wiley, New York, 1992. ISBN 978-0-471-62556-8 978-0-471-29336-1.

[125] Heinz-Peter Breuer and Francesco Petruccione. *The Theory of Open Quantum Systems*. Oxford University PressOxford, 1 edition, January

2007. ISBN 978-0-19-921390-0 978-0-19-170634-9. doi: 10.1093/acprof:oso/9780199213900.001.0001. URL https://academic.oup.com/book/27757.

[126] Anne Greenbaum, Ren-cang Li, and Michael L. Overton. First-order Perturbation Theory for Eigenvalues and Eigenvectors. 2019. doi: 10.48550/ARXIV.1903.00785. URL https://arxiv.org/abs/1903.00785. Publisher: arXiv Version Number: 2.

[127] J. M. Luttinger. Quantum Theory of Cyclotron Resonance in Semiconductors: General Theory. *Physical Review*, 102(4):1030–1041, May 1956. doi: 10.1103/PhysRev.102.1030. URL https://link.aps.org/doi/10.1103/PhysRev.102.1030. Publisher: American Physical Society.

[128] Gerard L. G. Sleijpen and Henk A. Van der Vorst. A jacobi-davidson iteration method for linear eigenvalue problems. *SIAM Review*, 42(2):267–293, 2000. ISSN 00361445. URL http://www.jstor.org/stable/2653109.

[129] Zhaojun Bai, James Demmel, Jack Dongarra, Axel Ruhe, and Henk van der Vorst. *Templates for the Solution of Algebraic Eigenvalue Problems*. Society for Industrial and Applied Mathematics, 2000. doi: 10.1137/1.9780898719581. URL https://epubs.siam.org/doi/abs/10.1137/1.9780898719581.

Appendix A

The K matrices

The effect of the magnetic field on the Bloch functions and spin is described by the following Hamiltonian [127]:

$$H_{\text{Bloch}} = -(3\kappa + 1)\mu_B \mathbf{B} \cdot \mathbf{L} + g_0 \mu_B \mathbf{B} \cdot \mathbf{S} = \mu_B \mathbf{B} \cdot \vec{K}\,, \tag{A.0.1}$$

where $\mathbf{L}$ is the (orbital) angular momentum of the Bloch function, $\mathbf{S}$ its spin, and $\kappa = -0.42$ in silicon. We neglect the effects of the much smaller $\propto q$ term of Ref. [127]. We give below the expression of the matrices K_x, K_y, K_z consistent with our choice of phases for the Bloch functions [taking $g_0 = 2$ in Eq. (A.0.1)]:

$$K_x = -\begin{pmatrix} 0 & \sqrt{3}\kappa & 0 & 0 & -\sqrt{\frac{3}{2}}\kappa' & 0 \\ \sqrt{3}\kappa & 0 & 2\kappa & 0 & 0 & -\frac{\kappa'}{\sqrt{2}} \\ 0 & 2\kappa & 0 & \sqrt{3}\kappa & \frac{\kappa'}{\sqrt{2}} & 0 \\ 0 & 0 & \sqrt{3}\kappa & 0 & 0 & \sqrt{\frac{3}{2}}\kappa' \\ -\sqrt{\frac{3}{2}}\kappa' & 0 & \frac{\kappa'}{\sqrt{2}} & 0 & 0 & \kappa'' \\ 0 & -\frac{\kappa'}{\sqrt{2}} & 0 & \sqrt{\frac{3}{2}}\kappa' & \kappa'' & 0 \end{pmatrix} \tag{A.0.2}$$

$$K_y = i \begin{pmatrix} 0 & \sqrt{3}\kappa & 0 & 0 & -\sqrt{\frac{3}{2}}\kappa' & 0 \\ -\sqrt{3}\kappa & 0 & 2\kappa & 0 & 0 & -\frac{\kappa'}{\sqrt{2}} \\ 0 & -2\kappa & 0 & \sqrt{3}\kappa & -\frac{\kappa'}{\sqrt{2}} & 0 \\ 0 & 0 & -\sqrt{3}\kappa & 0 & 0 & -\sqrt{\frac{3}{2}}\kappa' \\ \sqrt{\frac{3}{2}}\kappa' & 0 & \frac{\kappa'}{\sqrt{2}} & 0 & 0 & \kappa'' \\ 0 & \frac{\kappa'}{\sqrt{2}} & 0 & \sqrt{\frac{3}{2}}\kappa' & -\kappa'' & 0 \end{pmatrix} \tag{A.0.3}$$

$$K_z = - \begin{pmatrix} 3\kappa & 0 & 0 & 0 & 0 & 0 \\ 0 & \kappa & 0 & 0 & \sqrt{2}\kappa' & 0 \\ 0 & 0 & -\kappa & 0 & 0 & \sqrt{2}\kappa' \\ 0 & 0 & 0 & -3\kappa & 0 & 0 \\ 0 & \sqrt{2}\kappa' & 0 & 0 & \kappa'' & 0 \\ 0 & 0 & \sqrt{2}\kappa' & 0 & 0 & -\kappa'' \end{pmatrix}, \tag{A.0.4}$$

with $\kappa' = 1 + \kappa$ and $\kappa'' = 1 + 2\kappa$. Note that in the $J = 3/2$ subspace (the top left 4×4 sub-blocks of K_x, K_y and K_z), H_{Bloch} is formally equivalent to $-2\kappa\mu_B \mathbf{B} \cdot \mathbf{J}$, where $\mathbf{J} = \mathbf{L} + \mathbf{S}$ is the total angular momentum of the Bloch function [127]. The eigenstates are computed with an iterative Jacobi-Davidson eigensolver [128, 129].

Appendix B

Dependance of the perturbation matrix elements with magnetic field

The time-dependent Hamiltonian equation (5.3.1) of the system described in chapter 5 could be is rewritten as

$$H(\mathbf{B},t) = H_0(\mathbf{B}) + \chi(t)U \tag{B.0.1}$$

H_0 can be written explicitely as function of the static magnetic field $\mathbf{B}$. $|\varphi_n^{\uparrow}(\mathbf{B})\rangle$ and $|\varphi_n^{\downarrow}(\mathbf{B})\rangle$ are the eigenstates of $H_0(\mathbf{B})$ of energy levels $E_n^{\uparrow}(\mathbf{B})$ and $E_n^{\downarrow}(\mathbf{B})$ respectively. $\uparrow$ and $\downarrow$ represent a pseudo-spin since the physical spin is not a good quantum number in presence of spin-orbit coupling. There are no dependece neither on $\mathbf{B}$ or on the electron (hole) spin of the electrostatic perturbation $U(\vec{r})$.

The matrix of U is written in the basis of the states $|\varphi_1^{\uparrow}(\mathbf{B})\rangle$ and $|\varphi_1^{\downarrow}(\mathbf{B})\rangle$ which is the origin of the decoherence processes. We follow the derivation of Ref [110] to study the evolution of the matrix U with respect to $\mathbf{B}$

$H_0(\mathbf{B})$ can be developed in powers of $\mathbf{B}$:

$$H_0(\mathbf{B}) \approx H_0(0) - \mathbf{B}\cdot\vec{M} + \mathcal{O}(B^2) \tag{B.0.2}$$

where $M_\alpha = -\partial H/\partial B_\alpha|_{B=0}$. Second and higher order terms can be safely neglected [110].

B.1 Case of zero magnetic field

The levels of the doublet are Kramers degenerate for $B = |\mathbf{B}| = 0$, i.e., $E_1^{\uparrow}(0) = E_1^{\downarrow}(0) = E_1$. In addition, we can choose the phase of the wavefunctions so that

$$|\varphi_1^{\uparrow}(0)\rangle = T|\varphi_1^{\downarrow}(0)\rangle \tag{B.1.1}$$

where T is the time-reversal symmetry operator.

Writing $|\varphi_1^{\downarrow}(0)\rangle = \alpha(\vec{r})|+\rangle + \beta(\vec{r})|-\rangle$ where $|+\rangle$ and $|-\rangle$ are the physical spin components, we obtain

$$|\varphi_1^{\uparrow}(0)\rangle = T|\varphi_1^{\downarrow}(0)\rangle = \beta^*(\vec{r})|+\rangle - \alpha^*(\vec{r})|-\rangle \tag{B.1.2}$$

from which we deduce

$$\begin{aligned} u_0 &= \langle\varphi_1^{\uparrow}(0)|U|\varphi_1^{\uparrow}(0)\rangle = \langle\varphi_1^{\downarrow}(0)|U|\varphi_1^{\downarrow}(0)\rangle = \\ &= \int \left[|\alpha(\vec{r})|^2 + |\beta(\vec{r})|^2\right] U(\vec{r}) d^3\vec{r} \end{aligned} \tag{B.1.3}$$

We used the fact that $U(\vec{r})$ does not involve the spin. Similarly, we obtain:

$$\langle\varphi_1^{\uparrow}(0)|U|\varphi_1^{\downarrow}(0)\rangle = \int \left[\beta(\vec{r})\alpha(\vec{r}) - \alpha(\vec{r})\beta(\vec{r})\right] U(\vec{r}) d^3\vec{r} = 0. \tag{B.1.4}$$

In absence of magnetic field, the effect of U is just a rigid shift of the energy levels, the states remain uncoupled. Time-reversal symmetry breaking is needed for a non-zero coupling [110].

B.2 Case of non-zero magnetic field

The energy splitting between the levels $n = 1$ and $n = 2$ being large compared to the magnetic field Hamiltonian, first-order perturbation theory can be used to derive the states for $\mathbf{B} \neq 0$

$$|\varphi_1^{\uparrow}(\mathbf{B})\rangle = |\varphi_1^{\uparrow}(0)\rangle - B \sum_{n>1,\sigma} \frac{\langle \varphi_n^{\sigma}(0)|\mathbf{B}\cdot\vec{M}|\varphi_1^{\uparrow}(0)\rangle}{E_1 - E_n}|\varphi_n^{\sigma}(0)\rangle \tag{B.2.1}$$

$$|\varphi_1^{\downarrow}(\mathbf{B})\rangle = |\varphi_1^{\downarrow}(0)\rangle - B \sum_{n>1,\sigma} \frac{\langle \varphi_n^{\sigma}(0)|\mathbf{b}\cdot\vec{M}|\varphi_1^{\downarrow}(0)\rangle}{E_1 - E_n}|\varphi_n^{\sigma}(0)\rangle \tag{B.2.2}$$

where $\mathbf{b} = \mathbf{B}/B$. Here we have chosen $|\varphi_1^{\uparrow}(0)\rangle$ and $|\varphi_1^{\downarrow}(0)\rangle$ so that $\langle\varphi_1^{\uparrow}(0)|\mathbf{b}\cdot\vec{M}|\varphi_1^{\downarrow}(0)\rangle = 0$ (by diagonalizing $\mathbf{b}\cdot\vec{M}$ in the Kramers doublet subspace). The non-diagonal term of the matrix U can be written as

$$u_{\uparrow\downarrow} = \langle\varphi_1^{\uparrow}(\mathbf{B})|U|\varphi_1^{\downarrow}(\mathbf{B})\rangle = \eta_{\uparrow\downarrow}(\mathbf{b})B \tag{B.2.3}$$

with

$$\begin{aligned}\eta_{\uparrow\downarrow}(\mathbf{b}) = \quad & -\sum_{n>1,\sigma} \frac{\langle \varphi_n^{\sigma}(0)|\mathbf{b}\cdot\vec{M}|\varphi_1^{\downarrow}(0)\rangle}{E_1 - E_n}\langle\varphi_1^{\uparrow}(0)|U|\varphi_n^{\sigma}(0)\rangle \\ & -\sum_{n>1,\sigma} \frac{\langle \varphi_1^{\uparrow}(0)|\mathbf{b}\cdot\vec{M}|\varphi_n^{\sigma}(0)\rangle}{E_1 - E_n}\langle\varphi_n^{\sigma}(0)|U|\varphi_1^{\downarrow}(0)\rangle.\end{aligned} \tag{B.2.4}$$

Similar expressions can be derived for diagonal terms:

$$\begin{aligned}u_{\uparrow\uparrow} &= \langle\varphi_1^{\uparrow}(\mathbf{B})|U|\varphi_1^{\uparrow}(\mathbf{B})\rangle = u_0 + \eta_{\uparrow\uparrow}(\mathbf{b})B \\ u_{\downarrow\downarrow} &= \langle\varphi_1^{\downarrow}(\mathbf{B})|U|\varphi_1^{\downarrow}(\mathbf{B})\rangle = u_0 + \eta_{\downarrow\downarrow}(\mathbf{b})B.\end{aligned} \tag{B.2.5}$$

Formally similar expressions can as well be obtained for the terms $u_n^{\uparrow\uparrow}$ and $u_n^{\downarrow\downarrow}$ of the other states ($n > 1$). We deduce that the angular frequency ω_{th} that characterizes the analytic expression for T_2 is proportional to B,

$$\omega_{th} = \frac{|u_{\uparrow\uparrow} - u_{\downarrow\downarrow}|}{\hbar} = \frac{|\eta_{\uparrow\uparrow}(\mathbf{b}) - \eta_{\downarrow\downarrow}(\mathbf{b})|}{\hbar}B, \tag{B.2.6}$$

and therefore the dephasing time for $\nu = \omega_{th}$ varies as $1/B$,

$$T_2(\nu = \omega_{th}) = \frac{2\hbar}{|\eta_{\uparrow\uparrow}(\mathbf{b}) - \eta_{\downarrow\downarrow}(\mathbf{b})|B}. \tag{B.2.7}$$

Appendix C

Origin of the law in $2/\nu = 1/\nu_{cl}$ of the dephasing time T_2

C.1 General arguments

In this section, we are interested in the dephasing time T_2 due to a telegraphic signal of "classical" frequency $\nu_{cl} = \nu/2$. In a time interval $[0, t]$, the average number of flips is equal to $\nu_{cl}t$. In this case, the Poisson distribution gives the probability that the fluctuator switches exactly n times during the elapsed time t:

$$P_n(t) = \frac{(\nu_{cl}t)^n}{n!} \exp(-\nu_{cl}t). \tag{C.1.1}$$

The probability $P_0(t)$ of not switching is therefore equal to $\exp(-\nu_{cl}t)$.

Consider a system characterized by the Larmor angular frequencies Ω and Ω' in states 0 and 1, respectively. The phase shift $\delta\phi(t)$ of the qubit precession thus varies as $(\Omega' - \Omega)(t - t_0)$ after the first switch from state 0 to state 1 at time t_0 ($\delta\phi(t) = 0$ for $t < t_0$).

T_2 characterizes the decay of the quantity $\langle \exp(i\delta\phi(t)) \rangle_{\{E\}}$. We can write:

$$\langle \exp(i\delta\phi(t)) \rangle_{\{E\}} = \sum_n P_n(t) \langle \exp(i\delta\phi_n(t)) \rangle_{\{E_n\}} \tag{C.1.2}$$

where $\delta\phi_n(t)$ represents the phase shifts in all situations $\in \{E_n\}$ where the fluctuator has switched exactly n times during the elapsed time t.

We now consider the configuration where $|\Omega' - \Omega| \gg \nu$, i.e. where the dephasing angular frequency is large compared to the frequency of the telegraph noise. In this case, for a large number of realizations of the experiment, the phase coherence will be lost from the moment the fluctuator has changed state. Since $\delta\phi_0(t) = 0$, we obtain

$$\langle \exp(i\delta\phi(t)) \rangle_{\{E\}} \approx P_0(t) \langle \exp(i\delta\phi_0(t)) \rangle_{\{E_0\}} = \exp(-\nu_{cl} t) \tag{C.1.3}$$

from which we deduce $T_2 = 1/\nu_{cl} = 2/\nu$.

This calculation can be easily generalized to the situation where the qubit is influenced by M fluctuators in the case where the change of angular frequency $\Omega'^{(j)} - \Omega$ induced by each fluctuator j is large compared to its switching frequency $\nu^{(j)}$. The probability that the fluctuator j does not switch is therefore $P_0^{(j)}(t) = \exp(-\nu_{cl}^{(j)} t)$ with $\nu_{cl}^{(j)} = \nu^{(j)}/2$. We obtain

$$\langle \exp(i\delta\phi(t)) \rangle_{\{E\}} \approx \prod_j P_0^{(j)}(t) = \exp\left(-t \sum_j \nu_{cl}^{(j)} \right) \tag{C.1.4}$$

from which we deduce $T_2 = 2/\sum_j \nu^{(j)}$.

In the (probable) case where one of the fluctuators is much faster than the others, T_2 is well given by $2/\max(\nu^{(j)})$, i.e. the coherence of the qubit is limited by the fastest of the fluctuators that perturb it.

Appendix D

Long-time limit of a N-level system perturbed by a low-frequency telegraphic noise

We consider a system of N levels $\{E_1 \cdots E_N\}$ and wavefunctions $\{|\phi_1\rangle \cdots |\phi_N\rangle\}$, eigenvalues and eigenstates of H_0. Each energy E_i is written as $\hbar\omega_i$. The system is influenced by a telegraphic noise ($\chi(t) = 0, 1$), it fluctuates between two configurations 0 and 1 with probability q_0 q_1, respectively. The switch between 0 and 1 is a stochastic process characterized by a mean switching frequency ν. The Hamiltonian is $H(t) = H_0 + \chi(t)U$ in which U is the perturbation when the system switches from 0 to 1. The eigenvalues of $H_0 + U$ are called $E_i' = \hbar\omega_i'$. The system switches between the two configurations at the times $t_1, t_2 \cdots$.

We must solve the time-dependent Schrödinger equation:

$$i\hbar\frac{d\Psi(t)}{dt} = H(t)\Psi(t) \tag{D.0.1}$$

We assume that $H(t) = H_0$ for $t_0 \leq t < t_1$ with the initial condition $\Psi(t_0) = \Psi_0$. The propagation of the state can be easily written. For example, since the system is in the configuration 0 between t_0 and t_1 and the configuration 1 between t_1 and t_2, the wavefunction at t_2 is given by:

$$PT'(\Delta t_2)P^{+}T(\Delta t_1)\Psi_0 \tag{D.0.2}$$

in which $T(\Delta t_n)$ is the diagonal matrix

$$\begin{bmatrix} \exp\left(-i\omega_1\Delta t_n\right) & & 0 \\ & \ddots & \\ 0 & & \exp\left(-i\omega_N\Delta t_n\right) \end{bmatrix} \tag{D.0.3}$$

with $\Delta t_n = t_n - t_{n-1}$. $T'(\Delta t_n)$ is the same matrix in which the angular frequencies ω_i are replaced by ω_i'.

P is the basis change matrix, that is, the matrix of the eigenvectors of $H_0 + U$ in the basis of the eigenstates of H_0. In Eq. (D.0.2), we used $P^{-1} = P^{+}$.

We see that we can define a sequence of states given by recursion, i.e.,

$$\begin{aligned} |\Psi_n\rangle &= P^{+}T(\Delta t_n)|\Psi_{n-1}\rangle \text{ for } n \text{ odd} \\ |\Psi_n\rangle &= PT'(\Delta t_n)|\Psi_{n-1}\rangle \text{ for } n \text{ even.} \end{aligned} \tag{D.0.4}$$

We define the density operator $\rho_n = \overline{|\Psi_n\rangle\langle\Psi_n|}$ in which the overline means the statistical average on the different random realizations of the time interval Δt_n for the mean switching frequency ν.

Here we want to understand what happens in the long run, after a large number of switches of the fluctuator, in the case of a low-frequency telegraphic noise. We consider the situation where

$$\nu \ll \omega_i, \forall i. \tag{D.0.5}$$

In this case, the quantities $\exp(i\omega_i t)$ present in the propagators can be written as $\exp(i\theta)$ in which θ can be seen as a random variable between 0 and 2π.

Using Eq. (D.0.4), the diagonal term $(\rho_n)_{ii}$ which gives the electronic population on the level i after n switches is given, for odd n, by

$$\overline{\sum_{kl} P^{+}_{ik} \exp\left(-i\omega_k \Delta t_n\right) (\rho_{n-1})_{kl} \exp\left(+i\omega_l \Delta t_n\right) P_{li}}. \tag{D.0.6}$$

For $k \neq l$, assuming $\omega_k \neq \omega_l$ which is likely in presence of a magnetic field that splits the spin doublets, we have

$$\overline{\exp\left(i(\omega_l - \omega_k)\Delta t_n\right)} = 0. \tag{D.0.7}$$

We deduce that

$$(\rho_n)_{ii} = \sum_k |P_{ik}|^2 (\rho_{n-1})_{kk}, \tag{D.0.8}$$

which can be rewritten as

$$(\rho_n) = A(\rho_{n-1}) \tag{D.0.9}$$

in which (ρ_n) represents the column vector composed of the diagonal matrix elements of the operator and

$$A = \begin{bmatrix} |P_{11}|^2 & \cdots & |P_{1N}|^2 \\ \vdots & \ddots & \vdots \\ |P_{N1}|^2 & \cdots & |P_{NN}|^2 \end{bmatrix}. \tag{D.0.10}$$

A similar result is obtained for even values of n.

Let X be an eigenvector of the matrix A for the eigenvalue λ, and x_i its largest component (in modulus). We have:

$$\sum_j |P_{ij}|^2 x_j = \lambda x_i \tag{D.0.11}$$

$$\implies \lambda = \sum_j |P_{ij}|^2 (x_j/x_i) \tag{D.0.12}$$

$$\implies |\lambda| \leq \sum_j |P_{ij}|^2 |x_j/x_i| \leq \sum_j |P_{ij}|^2 = 1. \tag{D.0.13}$$

This shows that the eigenvalues λ_i of A have a modulus smaller or equal to 1. In addition, 1 is always a trivial eigenvalue for the eigenvector

$$\begin{pmatrix} 1/\sqrt{N} \\ \vdots \\ 1/\sqrt{N} \end{pmatrix}. \tag{D.0.14}$$

Using Eq. (D.0.13) and Eq. (D.0.12), we deduce that an eigenvector X of A for $\lambda = 1$ have components of the form $x_j = \exp(i\psi_j)/\sqrt{N}$. Injecting this into Eq. (D.0.12) and taking the conjugate complex, we obtain

$$|\lambda|^2 = \sum_{j,k} |P_{ij}|^2 |P_{ik}|^2 \exp\left[i(\psi_j - \psi_k)\right] \tag{D.0.15}$$

$$= \sum_{j,k} |P_{ij}|^2 |P_{ik}|^2 \cos(\psi_j - \psi_k) = 1. \tag{D.0.16}$$

We deduce that $\psi_j = \psi_k$ must be imposed for all j and k to verify the last equation (for P_{ij} and P_{ik} nonzero, see below). Equation (D.0.14) is therefore the only eigenvector for the eigenvalue $\lambda = 1$. In reality, there is an exception to this rule when the Hamiltonian matrix $H_0 + U$ can be written as independent blocks so that A is also written as a block matrix, i.e., with non diagonal blocks in which $P_{ij} = 0$. In this case, the eigenvalue $\lambda = 1$ exists for each of the blocks, and N must be replaced by the size of the block.

From Eq. (D.0.9), we deduce the long time limit of the density:

$$(\rho_\infty) = \lim_{n\to\infty} (\rho_n) = \left[\lim_{n\to\infty} A^n\right] (\rho_0) \tag{D.0.17}$$

In the basis of the eigenvectors of A, putting the vector given by Eq. (D.0.14) first, we have

$$A_\infty = \left[\lim_{n\to\infty} A^n\right] = \begin{bmatrix} 1 & 0 & \cdots & 0 \\ 0 & 0 & \cdots & 0 \\ \vdots & \vdots & \ddots & \vdots \\ 0 & 0 & \cdots & 0 \end{bmatrix} \tag{D.0.18}$$

from which we deduce using Eq. (D.0.17)

$$(\rho_\infty) = QA_\infty Q^{-1}(\rho_0) \tag{D.0.19}$$

where Q is the matrix of the eigenvectors of A in which $Q_{i1} = 1/\sqrt{N}$ for all i [Eq. (D.0.14)]. Similarly, we can show that the first row of the matrix Q^{-1} is such that $Q^{-1}_{1i} = 1/\sqrt{N}$ for all i because of the orthogonality of the first column vector of Q to all other column vectors. This can be deduced from Eq. (D.0.11) which gives

$$\sum_{i,j} |P_{ij}|^2 x_j = \sum_j x_j = \lambda \sum_i x_i \tag{D.0.20}$$

which implies that $\sum_i x_i = 0$ for $\lambda \neq 1$. We conclude that not only the eigenvalue $\lambda = 1$ is nondegenerate but also the vectors associated with the other eigenvalues form an orthogonal subspace.

Using these results and Eq. (D.0.18), we deduce finally:

$$(\rho_\infty)_i = \sum_j Q_{i1} Q^{-1}_{1j} (\rho_0)_j = \frac{1}{N} \sum_j (\rho_0)_j = \frac{1}{N}. \tag{D.0.21}$$

This shows that the system always ends up in a situation of equipartition between all states of the basis, whatever the starting point.

In this proof, we have made the assumption that the matrix A is diagonalizable if an eigenvalue is degenerate. If this is not the case, the result can be generalized to the case of Jordan normal forms.

D.1 Application to the calculation of the relaxation lifetime T_1 in the two-level model

As in the main document, the Hamiltonian is written as

Appendix D: Long-time limit of a N-level system perturbed by a low-frequency telegraphic noise

$$H(t) = \begin{pmatrix} -\Delta E & 0 \\ 0 & \Delta E \end{pmatrix} + \chi(t) \begin{pmatrix} 0 & u_{\uparrow\downarrow} \\ u^*_{\uparrow\downarrow} & 0 \end{pmatrix} \tag{D.1.1}$$

in which we define $\Delta E = \hbar\Omega/2$. Here we assume $u_{\uparrow\uparrow} = u_{\downarrow\downarrow} = 0$, and $|u_{\uparrow\downarrow}|/\Delta E \ll 1$.

The matrix A defined in Eq. (D.0.10) is given by

$$A = \begin{bmatrix} \frac{1}{2}\left(1 + \frac{\Delta E}{\sqrt{\Delta E^2 + |u_{\uparrow\downarrow}|^2}}\right) & \frac{1}{2}\left(1 - \frac{\Delta E}{\sqrt{\Delta E^2 + |u_{\uparrow\downarrow}|^2}}\right) \\ \frac{1}{2}\left(1 - \frac{\Delta E}{\sqrt{\Delta E^2 + |u_{\uparrow\downarrow}|^2}}\right) & \frac{1}{2}\left(1 + \frac{\Delta E}{\sqrt{\Delta E^2 + |u_{\uparrow\downarrow}|^2}}\right) \end{bmatrix}. \tag{D.1.2}$$

We have:

$$\begin{pmatrix} \rho^n_\uparrow \\ \rho^n_\downarrow \end{pmatrix} = A \begin{pmatrix} \rho^{n-1}_\uparrow \\ \rho^{n-1}_\downarrow \end{pmatrix} \tag{D.1.3}$$

in which $\rho^n_\uparrow$ is the population on the state $\uparrow$ after n switches.

Calling z the axis of the magnetic field $\mathbf{B}$, the relaxation of the spin is described by the decay of σ^n_z given by $\rho^n_\uparrow - \rho^n_\downarrow$.

Using Eq. (D.1.3), we deduce

$$\sigma^n_z = \frac{\Delta E}{\sqrt{\Delta E^2 + |u_{\uparrow\downarrow}|^2}} \sigma^{n-1}_z. \tag{D.1.4}$$

Using the initial condition $\sigma^0_z = 1$, we obtain

$$\sigma^n_z = \left(\frac{\Delta E}{\sqrt{\Delta E^2 + |u_{\uparrow\downarrow}|^2}}\right)^n. \tag{D.1.5}$$

The average elapsed time for n steps being $t_n = n/\nu_{cl} = 2n/\nu$, σ^n_z can be rewritten as $\exp(-t_n/T_1)$ with

$$T_1 = \frac{4\Delta E^2}{\nu |u_{\uparrow\downarrow}|^2} = \frac{\hbar^2\Omega^2}{\nu |u_{\uparrow\downarrow}|^2}. \tag{D.1.6}$$

This result, obtained using $|u_{\uparrow\downarrow}|/\Delta E \ll 1$, in the limit $\nu \ll \Omega$. In this case, T_1 was derived from the noise spectral density at frequency Ω [17].

Appendix E

Calculation of R tensor's components

E.1 R tensor's components

the R tensor's components are calculated accordint to Redfield paper [94]. The g component can be calculated as seen

$$\begin{aligned} g_{\alpha\beta\delta\gamma}(\omega) &= \int_{-\infty}^{\infty} d\tau e^{i\omega t} < V_{\alpha\beta}(t)V_{\delta\gamma}(0) > \\ &= \int_{-\infty}^{\infty} dt e^{i\omega t} < B(t)U_{\alpha\beta}B(t)U_{\delta\gamma} > \\ &= \int_{-\infty}^{\infty} dt e^{i\omega t} < B(t)B(0) > U_{\alpha\beta}U_{\delta\gamma} \\ &= \Delta U_{\alpha\beta}U_{\delta\gamma}\int_{-\infty}^{\infty} dt e^{i\omega t}e^{-\nu t} = \frac{\Delta\nu U_{\alpha\beta}U_{\delta\gamma}}{\nu^2+\omega^2} \end{aligned} \tag{E.1.1}$$

$$< V_{\alpha\beta}(t)V_{\delta\gamma}(0) > =< V_{\delta\gamma}(t)V_{\alpha\beta}(0) > \tag{E.1.2}$$

$$g_{\alpha\beta\delta\gamma}(\Omega) = g_{\delta\gamma\alpha\beta}(\Omega) \tag{E.1.3}$$

$$g_{\alpha\beta\delta\gamma}(\Omega) = g^{*}_{\beta\alpha\gamma\delta}(-\Omega) \tag{E.1.4}$$

$$\omega_{01} = \frac{\Omega}{2} \tag{E.1.5}$$

$$\omega_{10} = -\frac{\Omega}{2} \tag{E.1.6}$$

Calculation of (4×4) R tensor elements

$$\begin{aligned}
\hbar^2 R_{0000} &= -g_{0110}(\Omega) - g_{0110}(-\Omega) \\
\hbar^2 R_{0011} &= g_{0110}(-\Omega) + g_{0110}(\Omega) \\
\hbar^2 R_{0001} &= g_{0010}(0) + g_{0010}(\Omega) - g_{1000}(\Omega) - g_{1110}(0) \\
&= g_{0010}(0) - g_{1110}(0) \\
\hbar^2 R_{0010} &= g_{0100}(-\Omega) + g_{0100}(0) - g_{0001}(-\Omega) - g_{0111}(0) \\
&= g_{0100}(0) - g_{0111}(0)
\end{aligned}$$

$$\begin{aligned}
\hbar^2 R_{1100} &= g_{1001}(\Omega) + g_{1001}(-\Omega) \\
\hbar^2 R_{1111} &= -g_{1001}(-\Omega) - g_{1001}(\Omega) \\
\hbar^2 R_{1101} &= g_{1011}(\Omega) + g_{1011}(0) - g_{1000}(0) - g_{1110}(\Omega) \\
&= g_{1011}(0) - g_{1000}(0) \\
\hbar^2 R_{1110} &= g_{1101}(0) + g_{1101}(-\Omega) - g_{0001}(0) - g_{0111}(-\Omega) \\
&= g_{1101}(0) - g_{0001}(0)
\end{aligned}$$

$$\begin{aligned}
\hbar^2 R_{0100} &= g_{0001}(-\Omega) - g_{0111}(-\Omega) \\
\hbar^2 R_{0111} &= g_{0111}(-\Omega) - g_{0001}(-\Omega) \\
\hbar^2 R_{0101} &= 2g_{0011}(0) - g_{0000}(0) - g_{1111}(0) - g_{0110}(\Omega) - g_{1001}(\Omega) \\
&= 2g_{0011}(0) - g_{0000}(0) - g_{1111}(0) - 2g_{0110}(\Omega) \\
\hbar^2 R_{0110} &= 2g_{0101}(-\Omega)
\end{aligned}$$

$$\begin{aligned}
\hbar^2 R_{1000} &= g_{1000}(\Omega) - g_{1110}(\Omega) \\
\hbar^2 R_{1011} &= g_{1110}(\Omega) - g_{1000}(\Omega) \\
\hbar^2 R_{1001} &= 2g_{0011}(0) - g_{0000}(0) - g_{1111}(0) - g_{1001}(-\Omega) - g_{0110}(-\Omega) \\
&= 2g_{0011}(0) - g_{0000}(0) - g_{1111}(0) - 2g_{1001}(-\Omega) \\
\hbar^2 R_{1010} &= 2g_{1010}(\Omega)
\end{aligned}$$

therefore

$$R_{0011} = -R_{0000} \quad R_{1111} = -R_{1100} \quad R_{0000} = R_{1111}$$
$$R_{0010} = R^*_{0001} \quad R_{1110} = R^*_{1101} \quad R_{1101} = -R_{0001}$$
$$R_{0111} = -R_{0100} \quad R_{1011} = -R_{1000} \quad R_{1000} = R^*_{0100}$$
$$R_{1010} = R^*_{0101}$$
$$R_{1001} = R^*_{0110}$$

E.2 R tensor's elements calculation

$$R_{0000} = \frac{1}{\hbar^2}[-g_{0110}(\Omega) - g_{0110}(-\Omega)] = -\frac{1}{\hbar^2}\frac{2\nu\Delta U_{01}U_{10}}{\nu^2+\Omega^2}$$
$$R_{0100} = \frac{1}{\hbar^2}[g_{0001}(-\Omega) - g_{0111}(-\Omega)] = \frac{1}{\hbar^2}\frac{\Delta\nu(U_{00}U_{01} - U_{01}U_{11})}{\nu^2+\Omega^2}$$
$$R_{0110} = \frac{2}{\hbar^2}[g_{0101}(-\Omega)] = \frac{1}{\hbar^2}\frac{2\Delta\nu U_{01}U_{01}}{\nu^2+\Omega^2}$$
$$R_{0001} = \frac{1}{\hbar^2}[g_{0010}(0) - g_{1110}(0)] = \frac{1}{\hbar^2}\frac{\Delta(U_{00}U_{10} - U_{11}U_{10})}{\nu}$$
$$R_{0101} = \frac{1}{\hbar^2}[2g_{0011}(0) - g_{0000}(0) - g_{1111}(0) - 2g_{0110}(\Omega)]$$
$$= \frac{1}{\hbar^2}\frac{\Delta\nu(2U_{00}U_{11} - U_{00}U_{00} - U_{11}U_{11})}{\nu} - \frac{1}{\hbar^2}\frac{2\Delta U_{01}U_{10}}{\nu^2-\Omega^2}$$